

2D and 3D photonic crystals: synthesis, characterization and topological phenomenon

Thesis by
Siyang Peng

In Partial Fulfillment of the Requirements for the
degree of
Doctor of Philosophy

The logo for the California Institute of Technology (Caltech), featuring the word "Caltech" in a bold, orange, sans-serif font.

CALIFORNIA INSTITUTE OF TECHNOLOGY
Pasadena, California

2018
Defended June 13th 2017

© 2018

Siyng Peng

ORCID: [0000-0002-1541-0278]

All rights reserved except where otherwise noted

ACKNOWLEDGEMENTS

First, I would like to thank my thesis advisor, Professor Harry A. Atwater, for his guidance and support throughout the entire work. This thesis reflects efforts exploring immature ideas and learning experience from unproductive experiments. I am grateful to Harry for giving me enough freedom to explore, while always offering his endless enthusiasm, patience and support. Scientifically, I have a deep respect for Harry's intellectual abilities. He provides sometimes the most unexpected but extremely valuable insights, which inspired me to think more creatively. I am also thankful for all the opportunities Harry had provided, such as attending conferences and collaborations.

I would like to thank my thesis committee members Professor James Eisenstein, Professor Andrei Faraon and Professor Gil Refael. Gil have provided much valuable feedback regarding research and career opportunities. Both Andrei and Jim have been a pleasure to interact with, and I appreciate their invaluable advice.

This thesis would not have been possible without all the contributions from my collaborators. I would like to thank Professor Albert Polman of AMOLF, the FOM-institute, for his constant support and encouragement. I started collaborating with Albert in 2013 on characterizing plasmon dispersions of metallic nanoparticles (described in Chapter 4). We moved on to work with silicon nanostructures (described in Chapter 5 and Chapter 6), which hopefully will be productive towards realizing topologically protected edge states.

I am grateful to Professor Paul Braun of University of Illinois at Urbana-Champaign. Paul provided valuable insights on 3D photonic crystal fabrication and offered collaboration opportunities on making high refractive gyroid structures, without which Chapter 2 and Chapter 3 would not be possible.

I am thankful to Professor William Andrew Goddard III, who I had collaborated with from 2012 to 2013 for work described in Chapter 7. Bill continued to offer valuable career advice throughout my years at Caltech which I am extremely grateful for.

Many thanks to Runyu Zhang of University of Illinois at Urbana-Champaign, who performed static CVD depositions and contributed ideas for work done in Chapter 2 and Chapter 3. We have been through many ups and downs of the project, Runyu has always been extremely encouraging and supportive. I would like to thank Dr. Philip Hon, Dr. Juan C. Garcia, and Dr. Luke Sweatlock, who worked with me

on angle resolved mid-infrared characterization. Phil contributed enormously towards designing and optimizing the set up, and Juan offered his incredible expertise to debug whenever we encounter difficulties. Emil Khabiboulline, who is now a graduate student at Harvard University, was also an indispensable member of the angle resolved mid-infrared characterization team. Emil wrote the entire Python code that automated the measurement, as well as developed the initial mpb code for bandstructure projection. Valerian Chen, who is now a graduate student at Oxford University, contributed a lot to the initial design, fabrication, and characterization work. Vitoria Barim, a undergraduate student from university of Helsinki, worked with me last summer on optimizing the angle resolved set up.

I would like to thank Benjamin Brenny, Toon Coenen, Sondra Hellstrom, Sophie Meuret, and Nick Schilder. Sophie, Nick, and Toon from AMOLF have been incredibly helpful with the CL experiment and data analysis; Chapter 5 and Chapter 6 would not have been possible without their help. The CL work in Chapter 4 was done with Benjamin and Toon's help. Sondra, who was a postdoc in Harry's group, developed a recipe for fabricating metallic nano-pillars.

I would like to thank Professor Matthew Sheldon, with whom I coauthored the paper described in Chapter 7. In addition, Matt mentored me through my first two years at Caltech which I am extremely grateful for. I am also thankful to Wei-Guang Liu and Andres Jaramillo-Botero who performed electronic states simulations described in Chapter 7.

I have benefited greatly from interacting with past and current members of the A-team, I would like to thank everyone for their contributions. In particular, I would like to acknowledge Dr. James Fakonas for teaching me everything I know about clean room fabrication. Dr. Yulia Tolstova and Dr. Seokmin Jeon taught and helped me a lot with high vacuum equipments. I would like to thank Tiffany Kimoto, Jennifer Blankenship, Liz Jennings, and Lyann Lau, who keep the Atwater group running smoothly.

Special thanks to Fan Liu, who has helped, supported and believed in me in every aspect for the past five years. I am also grateful for the friendship with Tian Zhong and Mingwu Lu. There were lots of good memories from the weekly Friday dinner. I would like to thank my grandparents, Xiaojun Kan and Zhongmin Peng, for their unconditional love. Family members who passed away, including my father Yong Peng (2003), grandmother Yide Qin (1997), and grandfather Shiming Xiang (2012), were very influential on my early interests in science. Finally and most importantly, I thank my mother, Yang Xiang, who has always been my role model and has always

unconditionally supported my dreams. This thesis is dedicated to her.

Siyang Peng

May 2017

Pasadena, CA

Dedicated to my mother, Yang Xiang

ABSTRACT

Topological photonics has become an increasingly popular research topic in the field of nanophotonics in recent years. Topological phases of light provide opportunities to manipulate light propagation efficiently at the nanoscale volume. Performance of conventional optical elements are limited by back-reflection and bending losses, which hinder their prospect of large scale integration. Topological protection enables unidirectional excitation of edge states or surface states without leaking into the bulk, as well as suppression of scattering when encountering defects and corners. With such advantages, topological photonic elements may surpass conventional photonic design for future generations of ultra-compact efficient computing, imaging, and sensing applications. Due to limitations of fabrication and characterization techniques, previously experimental efforts on topological photonics have been carried out with 2D micron-scale optical design or at the microwave wavelength.

This thesis contributes to the experimental development of topological photonics in two aspects: first, how to fabricate and characterize 3D photonic crystals and therefore extend topological protection into the 3D (Chapters 2-3); and second, how to realize nanoscale topological protection in the visible frequencies (chapters 4-6). Specifically, Chapter 2 reports fabrication of 3D single gyroid structures composed of a-Si and FTIR characterization of a photonic bandgap at the mid-infrared wavelength. This is the foundation to investigate more complex morphologies to introduce topologically nontrivial photonic states. Chapter 3 describe properties of double gyroid photonic crystals, followed by angle resolved characterization method in the mid-infrared. Double gyroid photonic crystals can be designed to possess quadratic degeneracy points, Weyl points, and line nodes. Since Weyl points have non-zero Chern numbers, surface states are topologically protected in double gyroid photonic crystals with parity breaking symmetry. The angle resolved characterization method could be utilize to resolve both Weyl points and surface states. Chapter 4 depicts design, fabrication, and characterization of Dirac-like surface plasmon dispersions in metallic nano-pillars. Chapter 5 presents experimental investigation of coupled silicon Mie resonators, which is the first step towards topological design based on inter-lattice sites coupling in the next chapter. Chapter 6 details photonic bandstructure from angle-resolved cathodoluminescence measurements. We analyze bandstructures collected from the bulk of trivially and topologically gapped

lattices, as well as zigzag and arm-chaired edges of domain boundaries. Chapter 7 outlines a method to optically enhance dissociation of hydrazine molecules using ultraviolet plasmons, and attempts to use this method for low temperature GaN growth.

PUBLISHED CONTENT AND CONTRIBUTIONS

- [1] Siying Peng et al. “Three-Dimensional Single Gyroid Photonic Crystals with a Mid-Infrared Bandgap”. In: *ACS Photonics* 3.6 (June 2016), pp. 1131–1137. DOI: 10.1021/acsp Photonics.6b00293.
S.P. participated in the design of the project, performed simulations, prepared the sample, collected the data, and participated in the writing of the manuscript.
- [2] “Ultraviolet surface plasmon-mediated low temperature hydrazine decomposition”. In: *Applied Physics Letters* 106.2 (Jan. 2015), p. 023102. DOI: 10.1063/1.4905593.
S.P. participated in the design of the set up, performed simulations, prepared the sample, collected the data, and participated in the writing of the manuscript.

TABLE OF CONTENTS

Acknowledgements	iii
Abstract	vii
Published Content and Contributions	ix
Table of Contents	x
List of Illustrations	xii
List of Tables	xxi
Chapter I: Introduction	1
Chapter II: Single gyroid photonic crystals with a mid-infrared bandgap: synthesis and Fourier transform infrared spectroscopy characterization	3
2.1 Introduction	3
2.2 Design and fabrication of a-Si single gyroid photonic crystals	5
2.3 Fourier transform infrared spectroscopy characterization	6
2.4 Discussion and conclusion	7
Chapter III: Double gyroid photonic crystals: synthesis and angle resolved mid-infrared characterization	12
3.1 Introduction	13
3.2 Frequency domain simulation method of double gyroids	14
3.3 Three-dimensional band structure projection onto a two-dimensional plane	15
3.4 Synthesis of double gyroid photonic crystals	15
3.5 Angle resolved mid-infrared spectroscopy	19
3.6 Conclusions and outlook	21
Chapter IV: Dirac-like plasmons in silver nanopillar honeycomb lattices: design, fabrication and cathodoluminescence characterization	25
4.1 Introduction	26
4.2 Tight binding model	26
4.3 Full wave finite-different time-domain design of Dirac-like plasmons	27
4.4 Fabrication of silver nanopillar honeycomb lattices	29
4.5 Cathodoluminescence characterization of Dirac-like plasmons	30
Chapter V: Mie resonators: resonances and couplings	34
5.1 Introduction	34
5.2 Sample Fabrication	35
5.3 Resonances and coupling of Mie resonators with aspect ratio=1	35
5.4 Resonances and coupling of Mie resonators with aspect ratio=0.65	37
5.5 Asymmetric dimers	38
5.6 Coupling of hexamers and honeycomb lattices	39
5.7 Conclusions and outlook	41
Chapter VI: Mie resonators in honeycomb lattices: Dirac-like dispersions and topological edgestates	45

6.1	Introduction	45
6.2	Dirac-like bandstructures of honeycomb lattice and edge states	46
6.3	Angle-resolved cathodoluminescence characterization of photonic bandstructures	47
6.4	Photonic band structures in the bulk and on the edges	49
6.5	Conclusions	50
Chapter VII: Ultraviolet surface plasmon-mediated low temperature hydrazine decomposition and growth of GaN		54
7.1	Motivation	54
7.2	N-H bond energy of the N_2H_4 molecule	55
7.3	FDTD simulation of aluminum plasmonic grating	57
7.4	Fabrication of aluminum grating by nanoimprint lithography and UV characterization	57
7.5	Low temperature hydrazine decomposition: experimental set up and characterization	59
7.6	Experimental set up of ultraviolet plasmon assisted low temperature GaN growth	62
7.7	XRD, XPS, EDS, and Raman characterization of GaN film synthesized at low temperature condition	63
7.8	Conclusions	66
Bibliography		68
Appendix A: Chapter 2 methods and supplementary information		77
A.1	Full Wave Band Structure Simulation	77
A.2	Sample Fabrication	77
A.3	FTIR Characterization	77
A.4	Full Wave Simulation on deformed Crystals	78
A.5	Optical constants of deposited materials	78
A.6	Fill fraction and discontinuity	78

LIST OF ILLUSTRATIONS

<i>Number</i>	<i>Page</i>
2.1 Single gyroid structure and photonic bandstructure simulation. (a) Stacks of unit cells of single gyroid structure. (b) bcc Brillouin zone. (c) Photonic band structure of a-Si single gyroid from full wave simulations, with unit cell size of $5\ \mu\text{m}$ in x, y, and z directions. The color map is proportional to the logarithm of the density of states.	4
2.2 Fabrication procedures of gyroid photonic crystals. (a) Two-photon lithography to define a sacrificial polymer scaffold of the gyroid structure. (b) Atomic layer deposition of Al_2O_3 to coat the polymer structure. (c) Focused ion beam milling to remove the sides of the structure, followed by oxygen plasma to remove the polymer, leaving a hollow alumina structure. (d) Chemical vapor deposition of a-Si to coat and in-fill the hollow alumina structure.	6
2.3 FTIR characterization of bandgaps. (a) Fourier transform infrared spectroscopy experimental configuration. (b) SEM images of a hollow gyroid at (001) crystal orientation with a-Si (150 nm)/ Al_2O_3 (40 nm)/a-Si (150 nm) layers. (c) Reflectance spectrum from full wave simulations of a hollow gyroid at (001) crystal orientation with a-Si (100 nm)/ Al_2O_3 (40 nm)/a-Si (100 nm) layers (gray dashed line), reflectance spectrum from full wave simulations of a trapezoidal hollow gyroid at (001) crystal orientation with a-Si (100 nm)/ Al_2O_3 (40 nm)/a-Si (100 nm) layers (black dashed line), FTIR measurement of a hollow gyroid with a-Si (100 nm)/ Al_2O_3 (40 nm)/a-Si (100 nm) layers (red dashed line), and FTIR measurement of a hollow gyroid with a-Si (150 nm)/ Al_2O_3 (40 nm)/a-Si (150 nm) layers (red dashed line).	8
2.4 FTIR characterization of single gyroids. (a) Reflectance, transmittance, and scattering + absorbance from a single gyroid structure with unit cell size of $4.5\ \mu\text{m}$ and a total of $20 \times 20 \times 10$ cells. (b) Comparison of reflection spectra of samples with unit cell sizes of 4.5 , 5.1 , and $5.5\ \mu\text{m}$ ($20 \times 20 \times 10$ unit cells).	9

2.5	Photonic band structure simulation. Photonic band structure of a single gyroid consists of a-Si (100 nm)/ Al_2O_3 (40 nm)/a-Si (100 nm) layers from full wave simulations, with unit cell size of $4.5 \mu\text{m}$ in x, y, and z directions. Bands in between the orange lines are accessible through FTIR characterization shown in	10
3.1	(a) BCC Brillouin zone (b) Double gyroids (c) Double gyroids with an airsphere which breaking parity symmetry (d) Double gyroids with two airspheres	13
3.2	Band structures of double gyroids with unit cell size of $4.68 \mu\text{m}$. . .	15
3.3	Band structures of double gyroids with unit cell size of $4.68 \mu\text{m}$ (a) Double gyroids with quadratic point degeneracy (indicated by yellow circles) (b) Double gyroids with Parity breaking symmetry, which give rise to a pair of Weyl points. The Parity breaking airsphere is indicated by the yellow circle in the unit cell. Weyl points are indicated by the yellow circles along Γ -N11 and Γ -H3. (c) Double gyroids with two air spheres in one unit cell (indicated by yellow circles). Line nodes are indicated by yellow circles Γ -N11 and Γ -H3.	16
3.4	Band structures of double gyroids with unit cell size of $4.68 \mu\text{m}$ (a) Double gyroids with parity breaking symmetry by an airsphere, which give rise to a pair of Weyl points. The parity breaking airsphere is indicated by the yellow circle in the unit cell. Weyl points are indicated by the yellow circles along Γ -N11 and Γ -H3. (b) Double gyroids with Parity breaking symmetry by a thin cylinder, which also give rise to a pair of Weyl points along the same symmetry directions. The parity breaking cylinder is placed at the spatial position as the airsphere.	16
3.5	Illustration of 3D band structure projection onto a 2D plane, along the <i>Gamma</i> -H1 direction.	17
3.6	Projection of double gyroid band structures along the [001] direction.	17
3.7	Projection of Weyl points band structures along the [001] direction. .	18
3.8	Projection of line nodes band structures along the [001] direction. . .	18
3.9	Synthesis of three-dimensional photonic crystals with high-refractive index materials.	19

3.10	FTIR characterization of double gyroids: (a) Illustration of FTIR set up (b) Reflectance spectrum from single gyroid (red), double gyroids (blue) and double gyroids with parity breaking symmetry (green) (c) SEM images of single gyroid (red), double gyroids (blue), and double gyroids with parity breaking symmetry (green)	21
3.11	Photo of angle resolved characterization set up	22
3.12	Angle resolved characterization set up for normal incidence reflectance measurement	22
3.13	Angle resolved characterization set up for off normal incidence measurement	23
3.14	Fabry-Perot resonance from silicon substrate (a) reflectance (b) transmittance (c) simulated reflectance	23
3.15	Double gyroid photonic band structures (a) simulation (b) experimental characterization	24
4.1	Honeycomb lattices with lattice constant a and lattice vectors e_1, e_2 , and e_3 ; one unit cell of the lattice has two lattice sites: A and B.	27
4.2	Dirac-like surface plasmon bandstructures: (a) three-dimensional bandstructures with six Dirac points, (b) two-dimensional bandstructures along high symmetry directions of the hexagonal lattice	27
4.3	(a) Full wave simulations of bandstructures of silver nanopillars in honeycomb lattices ($r=80\text{nm}$, $h=160\text{nm}$ with a Drude model approximation for silver dielectric constants) (b) Degree of hybridization ($\Delta\lambda$) as a function of lattice sites separation and aspect ratio of individual lattice sites	29
4.4	Electric field distribution of silver nanopillars at the M point and the K point	29
4.5	Opening a bandgap at the Dirac point (a) Gap size as a function of lattice distortions (b) Band structures of distorted lattice with a band gap at the Dirac point ($r=80\text{nm}$, $h=160\text{nm}$ with a Drude model approximation for silver dielectric constants)	30
4.6	Fabrication method: 1. Spin bottom two layers of ebeam resist (bottom layer: PMMA 495, top layer: PMMA 950), 2. Electron beam lithography to define honeycomb patterns and development of exposed areas 3. Electron beam deposition of germanium as the adhesive layer and silver 4. Lift off in Remover PG	31

4.7	SEM images of fabricated silver nanopillars in honeycomb lattices (a) top view (b) side view	31
4.8	Angle resolved cathodoluminescence of a single silver pillar at 650nm	32
4.9	Angle resolved cathodoluminescence of a dimer pair of silver pillars at 650nm	33
4.10	Angle resolved cathodoluminescence of silver pillars in honeycomb lattices at (a) 800nm (b) 750nm	33
5.1	Fabrication of Mie resonators on 10nm free-standing Si_3N_4 mem- branes: (a) Epitaxial lift off of a single crystalline silicon film from an SOI wafer (b) Placement of the silicon film on a 10nm free- standing Si_3N_4 membrane (c) Spin a layer of ZEP520 on the silicon film (d) Electron beam lithography on the ZEP520 film (e) Electron beam curing of the ZEP520 film as an etching mask (f) Reactive ion beam etching of the silicon film (g) Oxygen plasma cleaning to remove ZEP520	36
5.2	Single Mie resonator: (a) Scattering cross section of a single silicon Mie resonator with radius of 65nm and height of 130nm (b) Electric field intensity distribution of the top XY plane at 494nm (c) Elec- tric field intensity distribution of the center XZ plane at 494nm (d) Electric field intensity distribution of the top XY plane at 596nm (e) Electric field intensity distribution of the center XZ plane at 596nm .	38
5.3	Coupled Mie resonators (a) Scattering cross section of dimer silicon Mie resonators with radius of 65nm and height of 130nm and distance of 40nm from edge to edge (b) Electric field intensity distribution of the top XY plane at 484nm (c) Electric field intensity distribution of the center XZ plane at 484nm (d) Scattering cross section of : a single silicon Mie resonator with radius of 65nm and height of 130nm (dashed blue); dimer silicon Mie resonators at distance of 10nm apart (lightest blue); dimer silicon Mie resonators at distance of 15nm apart (second lightest blue); dimer silicon Mie resonators at distance of 20nm apart (third lightest blue); dimer silicon Mie resonators at distance of 40nm apart (fourth lightest blue) (e) Electric field intensity distribution of the top XY plane at 616nm (f) Electric field intensity distribution of the center XZ plane at 616nm	39

- 5.4 Cathodoluminescence characterization of coupled Mie resonators (a) CL spectrum of a single particle of radius 65nm and height 130nm at the center (left), side (middle), CL map at 571nm (right) (b) Dimers of 40nm apart: Cl spectrum at the center (left), side (middle), CL map at 599nm (right) (c) Dimers of 20nm apart: Cl spectrum at the center (left), side (middle), CL map at 624nm (right) (d) Dimers of 15nm apart: Cl spectrum at the center (left), side (middle), CL map at 644nm (right) (e) Dimers of 10nm apart: Cl spectrum at the center (left), side (middle), CL map at 689nm 40
- 5.5 Connected Mie resonators: (a) CL spectrum of a single particle of radius 65nm and height 130nm at the center (left), side (middle), CL map at 571nm (right) (b) Dimers of 10nm apart: Cl spectrum at the center (left), side (middle), CL map at 689nm (b) Connected dimers: Cl spectrum at the center (left), side (middle), CL map at 609nm . . . 41
- 5.6 Single Mie resonator: (a) CL spectrum of a single particle of radius 100nm and height 130nm at the center (b) CL spectrum of a single particle of radius 100nm and height 130nm at the side (c) CL intensity map at 422nm (d) CL intensity map at 483nm (e) CL intensity map at 568nm (f) CL intensity map at 624nm (g) CL intensity map 688nm 42
- 5.7 Coupled Mie resonators: (a) CL spectrum of a single particle of radius 100nm and height 130nm at the side (b) CL spectrum of dimer particles on the side (c) CL intensity map at 423nm (d) CL intensity map at 483nm (e) CL intensity map at 558nm (f) CL intensity map at 581nm (g) CL intensity map 632nm (g) CL intensity map 703nm . 42

5.8	Asymmetric dimers: (a) CL spectrum of a single particle of radius 100nm and height 130nm on the side (b) CL spectrum of a asymmetric dimer 40nm apart ($r_1=100\text{nm}$, $r_2=65\text{nm}$), excitation point on the side of the $r_1=100\text{nm}$ particle (c) CL spectrum of a asymmetric dimer 200nm apart ($r_1=100\text{nm}$, $r_2=65\text{nm}$), excitation point on the side of the $r_1=100\text{nm}$ particle (d) CL spectrum of a single particle of radius 65nm and height 130nm on the side (e) CL spectrum of a asymmetric dimer 40nm apart ($r_1=100\text{nm}$, $r_2=65\text{nm}$), excitation point on the side of the $r_1=65\text{nm}$ particle (f) CL spectrum of a asymmetric dimer 200nm apart ($r_1=100\text{nm}$, $r_2=65\text{nm}$), excitation point on the side of the $r_1=65\text{nm}$ particle (g) CL intensity map at 558nm of the 40nm apart dimer (h) CL intensity map at 614nm of the 40nm apart dimer (i) CL intensity map at 694nm of the 40nm apart dimer (j) CL intensity map 558nm of the 200nm apart dimer (k) CL intensity map 694nm of the 200nm apart dimer (l) CL intensity map 693nm of the 200nm apart dimer	43
5.9	Hexamers and honeycomb lattice modes: (a) Lattice l at 426nm, modes in the center (b) Lattice L at 664 nm, anti-bonding mode (c) Lattice L at 750 nm, bonding mode (d) SEM image of lattice l (e) Hexamer l at 426 nm (f) Hexamer l at 664 nm (g) Hexamer l at 750 nm (h) SEM image of hexamer l (i) Lattice s at 452 nm (j) Lattice s at 518 nm (k) Lattice s at 750 nm (l) SEM image of lattice s (m) Hexamer s at 452 nm (n) Hexamer s at 518 nm (o) Hexamer s at 750nm (p) SEM image of hexamer s	44
6.1	(a) Honeycomb lattice with lattice constant R1 for the smallest unit cell (diamond shaped dashed line), and triangular lattice with lattice constant R2 with the hexagonal shaped unit cell (dashed cell) (b) First Brillouin zone of the honeycomb lattice (dashed line), reduced Brillouin zone of the supercell triangular lattice (solid line) (c) Band structures of a honeycomb lattice in the first Brillouin zone (d) Band structures of a supercell triangular lattice with a band gap ($R2=2.9R1$) (e) Edge states at the Zigzag edge within the bandgap	47
6.2	Electron beam induced bands asymmetry: (a) 630 – 670 nm (b) 580 – 620 nm (c) 530 – 570 nm (d) 480 – 520 nm (e) 430 -470 nm (d) Lattice orientation and electron beam excitation location	49

- 6.3 Mapping band structures in the Brillouin zone: (a) Honeycomb lattices s 630-670nm; (b) Topologically gapped lattices s 630-670nm; (c) Trivially gapped lattices s 630-670nm; (d) Zigzag edges lattice s 630-670nm; (e) Arm-chaired lattice s 630-670nm; (f) Honeycomb lattices l 580-620nm; (g) Topologically gapped lattices l 580-620nm; (h) Trivially gapped lattices l 580-620nm; (i) Zigzag edges lattices l 580-620nm; (j) Arm-chaired lattices l 580-620nm 50
- 6.4 Spectral resolved photonic bands lattice s ($r_1=65\text{nm}$, $h=150\text{nm}$, trivial gap: $R_1=246\text{nm}$, $R_2=444\text{nm}$, factor=3.12): (a) 0 degrees topological gap (b) 15 degrees topological gap (c) 30 degrees topological gap (d) 45 degrees topological gap (e) 60 degrees topological gap (f) 0 degrees trivial gap (g) 15 degrees trivial gap (h) 30 degrees trivial gap (i) 45 degrees trivial gap (j) 60 degrees trivial gap (k) 0 degrees Zigzag edge (l) 15 degrees Zigzag edge (m) 30 degrees Zigzag edge (n) 45 degrees Zigzag edge (o) 60 degrees Zigzag edge (p) 0 degrees arm-chaired edge (q) 15 degrees arm-chaired edge (r) 30 degrees arm-chaired edge (s) 45 degrees arm-chaired edge (t) 60 degrees arm-chaired edge 51
- 6.5 Spectral resolved photonic bands honeycomb lattice l : ($r_1=284\text{nm}$, $h=230\text{nm}$, $R_1=526\text{nm}$) (a) 0 degrees honeycomb lattice l (b) 15 degrees honeycomb lattice l (c) 30 degrees honeycomb lattice l (d) 45 degrees honeycomb lattice l (e) 60 degrees honeycomb lattice l 52
- 6.6 Spectral resolved photonic bands honeycomb lattice l : (need information from MP5 on the trivial and topologically gapped lattice) (a) 0 degrees topological gap (b) 15 degrees topological gap (c) 30 degrees topological gap (d) 37 degrees topological gap (e) 45 degrees topological gap (f) 60 degrees topological gap (g) 0 degrees trivial gap (h) 15 degrees trivial gap (i) 30 degrees trivial gap (j) 37 degrees trivial gap (k) 45 degrees trivial gap (l) 60 degrees trivial gap (m) 0 degrees Zigzag edge (n) 15 degrees Zigzag edge (o) 30 degrees Zigzag edge (p) 37 degrees Zigzag edge (q) 45 degrees Zigzag edge (r) 60 degrees Zigzag edge (s) 0 degrees arm-chaired edge (t) 15 degrees arm-chaired edge (u) 30 degrees arm-chaired edge (v) 37 degrees arm-chaired edge (w) 45 degrees arm-chaired edge (x) 60 degrees arm-chaired edge 53

- 7.1 N_2H_4 energy curve: Solid black curve (S_0) is the singlet ground state for the N-H bond. Inside the potential well of S_0 , the horizontal lines represent the roto-vibrational states. Optical excitation at 5eV (free space wavelength 248nm) excites the ground state to higher roto-vibrational states and dissociates the N-H bond. The calculated curves depict the triplet first excited state (T_1 , solid red), the singlet first excited state (S_1 , dash black), the triplet second excited state (T_2 , dashed red), the singlet second excited state (S_2 , dotted black), and the triplet third excited state (T_3 , dotted red). 56
- 7.2 (a) Full wave (finite-difference time-domain) simulation of the reflectance versus wavenumber, $k_g = 2\pi/\text{grating pitch}$, and energy of the aluminum grating with 4 nm aluminum oxide on top. The surface plasmon dispersion and the photon dispersion are manifested as the reflectance minimums (dashed white) in the density plot. Localized surface plasmon modes (circles) and photonic modes (stars) are also indicated. (b) The electric field magnitude for two grating periods of the optimized design, with 248 nm incident photons, shows strong field confinement near the surface. The aluminum grating and aluminum oxide layers are marked by white dotted lines. (c) Full wave simulation (FDTD) of the reflectance spectrum at normal incidence is shown (black). The red curve is the experimentally measured reflectance. The dip in reflectance in both the simulated and measured spectra indicates a surface plasmon resonance at 248 nm. Inset: AFM image of the fabricated grating. 58
- 7.3 Schematic illustration of ultraviolet surface plasmon mediated athermal resonant dissociation of N_2H_4 . A 248 nm laser at normal incidence excites ultraviolet surface plasmons on the surface of a nanostructured Al grating which has been cooled to 77 K inside a low pressure atmosphere of N_2H_4 (105 Torr). The localized optical field resonantly dissociates N_2H_4 molecules adsorbed to the grating surface, and the dissociated species are detected via mass spectrometry. . 60
- 7.4 GaN growth. (a) A Schematic illustration of a low temperature nitrogen source and epitaxial growth scheme of GaN. (b) View of the actual experimental chamber. 63
- 7.5 GaN film on gold substrate (a) Transmission electron micrograph of the film cross-section. (b) Scanning electron micrograph of the film. . 65

7.6	X-ray photoelectron spectroscopy of GaN film at nitrogen 1s of (a) GaN film grown on gold substrate. (b) Commercial GaN crystal on silicon wafer.	65
7.7	X-ray photoelectron spectroscopy of GaN film at gallium 2p _{3/2} of (a) GaN film grown on gold substrate. (b) Commercial GaN crystal on silicon wafer.	66
7.8	X-ray photoelectron spectroscopy of GaN film at oxygen 1s of (a) GaN film grown on gold substrate. (b) Commercial GaN crystal on silicon wafer.	66
A.1	Optical constants at Mid-infrared wavelength. (a) measured real part of refractive index of a-Si (black solid line) and Palik's real part of refractive index of a-Si (blue dotted line) (b) measured imaginary part of refractive index of a-Si (red solid line) Palik's imaginary part of refractive index of a-Si (blue dotted line) (c) measured real part of refractive index of Al ₂ O ₃ (black solid line) and Palik's real part of refractive index of Al ₂ O ₃ (blue dotted line) (d) measured imaginary part of refractive index of Al ₂ O ₃ and Palik's real part of refractive index of (blue dotted line)Al ₂ O ₃	79
A.2	Single gyroid with different u(x,y,z). (a) u(x,y,z) versus fill fraction for a solid single gyroid (b) single gyroid with u(x,y,z)=1.00, 1.35, 1.40, 1.41, and 1.42 respectively	80

LIST OF TABLES

<i>Number</i>		<i>Page</i>
7.1	The corrected partial pressure and quantum yield of the dissociated N_2H_4 species based on mass spectrometry.	62
7.2	Energy dispersive X-ray spectroscopy.	65
A.1	$u(x,y,z)$ versus fill fraction for a solid single gyroid.	79

Chapter 1

INTRODUCTION

Topological phases of matter have emerged as a new paradigm of classifying materials in recent years. Topology originates from mathematics that is concerned with properties preserved through deformations, twistings, and stretchings. Quantities that can be continuously changed into one another are topologically equivalent. Topologies for materials are established in the context of dispersion relations. For band structures, the topologically invariant quantity is the Chern number, named after the Chinese mathematician Shiing-Shen Chern. Materials can be classified based on Chern numbers of their bandstructures. For bandstructures with zero Chern numbers, the material is topologically trivial, while non-zero Chern numbers indicate topologically nontrivial band dispersions.

The first example of topologically interesting material is the integer quantum Hall effect, discovered in 1980[1, 2]. 2D electrons gas forms quantized cyclotron orbits under a strong magnetic field. With an energy gap in the bulk, electrons travel only along edges of the 2D plane. Influenced by the magnetic field, conducting electrons are spatially separated into two different lanes where electrons along the top edge only travels in the direction opposite to electrons along the bottom edge. The discovery is followed by the spin Hall state, which is also known as topological insulators. A topological insulator is an insulator in the bulk with conducting edge states as a result of spin-orbit coupling, without the applying a magnetic field. Backscattering of electrons is impeded when encountering impurities and corners. Unlike the quantum Hall state, there are two conducting states along each edge propagating in opposite directions, associated with spin up and spin down. Although not spatially separated, the spin up and spin down state does not scatter into each other protected by the Kramer's theorem. Early experimental observation of the spin Hall state were made in materials include CdTe/HgTe/CdTe quantum wells and Bi_2Te_3 bulk crystals.

Analogous to quantum Hall effect, photonic topological insulators were first proposed by Haldane and Raghu in 2005[3, 4]. Periodic variation of refractive index in photonic crystals modulate photons in the same way as solid state materials do to electrons. In photonic topological insulators, photons are allowed to propagate along the interface of two topologically inequivalent domains. The number of pho-

tonic edge states allowed at the interface is determined by the difference of Chern numbers between the two domains. Technologically, being able to transport photons with efficiently with immunity to fabrication disorders is the most most attractive aspect of photonic topological insulators[5].

Photonic topological insulators have been designed and experimentally realized in a number of systems. Time reversal symmetry of gyromagnetic photonic crystals could be broken by applying a uniform magnetic field. For example, Wang et. al. observed one way propagating edge states in gyromagnetic photonic crystals at microwave frequencies[6, 7]. Coupling between photonic resonators can be controlled to form topologically non-trivial frequency gaps, shown in the work by Hafezi et. al[8, 9]. In this work, the phase of photons propagating through the resonator is carefully designed to mimic the behavior of electron in a magnetic field. Unidirectional propagation in edge waveguides immune to disorder is observed at the telecommunication wavelength. Based on the Floquet band theory, Rechtsman et al. translate modulation from the time domain to the spatial domain, where periodic helical modulations in z direction break the z-symmetry, creating an effective magnetic field. They observed the photonic analogue of the quantum Hall effect at optical frequencies[10].

Chapter 2 and Chapter3 of this thesis focus on topological properties of 3D photonic crystals by breaking parity inversion symmetry[11]. Chapter 4, Chapter 5, and Chapter 6 of this thesis focus on topological edge state associated with Dirac cones. Specifically, in Chapter 6 topological bands are formed by distorting the honeycomb lattice, from which pseudo-time-reversal symmetry is constructed[12].

Chapter 2

SINGLE GYROID PHOTONIC CRYSTALS WITH A MID-INFRARED BANDGAP: SYNTHESIS AND FOURIER TRANSFORM INFRARED SPECTROSCOPY CHARACTERIZATION

A gyroid structure is a distinct morphology that is triply periodic and consists of minimal isosurfaces containing no straight lines. We have designed and synthesized amorphous silicon (a-Si) mid-infrared gyroid photonic crystals that exhibit a complete bandgap in infrared spectroscopy measurements. Photonic crystals were synthesized by deposition of a-Si/ Al_2O_3 coatings onto a sacrificial polymer scaffold defined by two-photon lithography. We observed a 100% reflectance at $7.5 \mu\text{m}$ for single gyroids with a unit cell size of $4.5 \mu\text{m}$, in agreement with the photonic bandgap position predicted from full-wave electromagnetic simulations, whereas the observed reflection peak shifted to $8 \mu\text{m}$ for a $5.5 \mu\text{m}$ unit cell size. This approach represents a simulation-fabrication-characterization platform to realize three-dimensional gyroid photonic crystals with well-defined dimensions in real space and tailored properties in momentum space.

2.1 Introduction

Three-dimensional photonic crystals offer opportunities to probe interesting photonic states such as bandgaps,[13, 14, 15, 16, 17, 18, 19, 20] Weyl points,[11, 21] well-controlled dislocations and defects.[22, 23, 24] Combinations of morphologies and dielectric constants of materials can be used to achieve desired photonic states. Gyroid crystals have interesting three-dimensional morphologies defined as triply periodic body centered cubic crystals with minimal surfaces containing no straight lines.[11, 21, 25, 26, 27, 28, 29, 30] A single gyroid structure, such as the one shown in Figure 2.1a, consists of isosurfaces described by

$$\sin(x)\cos(y) + \sin(y)\cos(z) + \sin(z)\cos(x) > u(x, y, z) \quad (2.1)$$

where the surface is constrained by $u(x,y,z)$. Gyroid structures exist in biological systems in nature. For example, self-organizing process of biological membranes forms gyroid photonic crystals that exhibit the iridescent colors of butterfly's wings.[31] Optical properties of gyroids could vary with tuning of $u(x,y,z)$,[32] unit

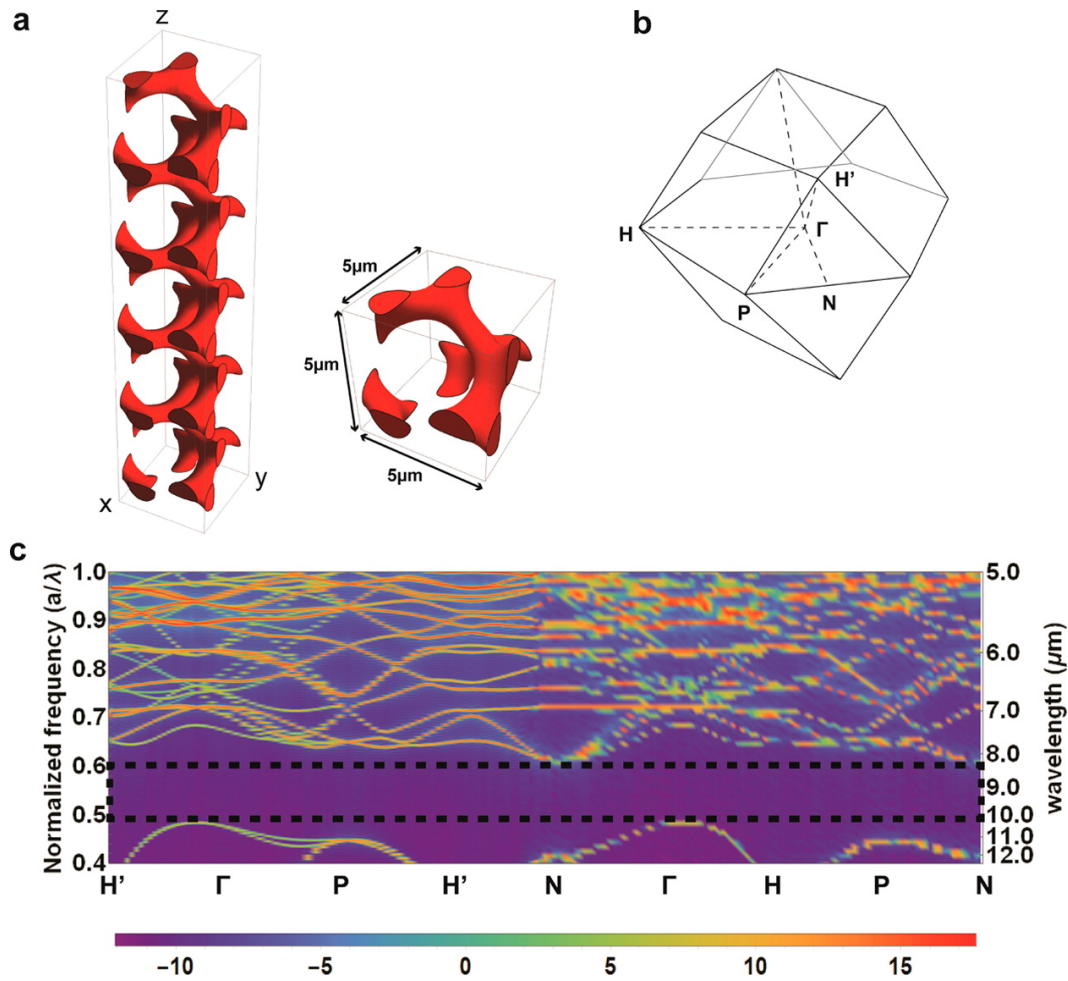


Figure 2.1: Single gyroid structure and photonic bandstructure simulation. (a) Stacks of unit cells of single gyroid structure. (b) bcc Brillouin zone. (c) Photonic band structure of a-Si single gyroid from full wave simulations, with unit cell size of $5 \mu\text{m}$ in x , y , and z directions. The color map is proportional to the logarithm of the density of states.

cell size, and spatial symmetry,[11] as well as refractive index contrast. Single gyroid photonic crystals, when designed with high refractive index and fill fraction, are predicted to possess among the widest complete three-dimensional bandgaps,[11, 33] making them interesting for potential device applications such as broadband filters and optical cavities. In this work, we demonstrate a synthesis approach for forming mid-infrared three-dimensional gyroid photonic crystals, and report experimental measurements of the bandgap for a single gyroid structure at mid-infrared wavelengths.

2.2 Design and fabrication of a-Si single gyroid photonic crystals

To realize gyroid photonic crystals at mid-infrared wavelengths, we utilize full-wave finite-difference time-domain (FDTD) simulations to determine the dimensions and materials required for crystal design (see Appendix A1). The simulation shown in Figure 2.1c reveals that a-Si single gyroid crystals with a unit cell size of $5 \mu\text{m}$ and $u(x,y,z) = 1.1$ (see Table A.1 for fill fraction) has a complete bandgap (indicated by the dashed box) from 8 to $10 \mu\text{m}$ in all symmetry directions of the bcc Brillouin zone in Figure 2.1b. In units of normalized frequency calculated by dividing unit cell size (a) by wavelength (Λ), the complete bandgap is between 0.5 and 0.6. For constant refractive index at mid-infrared wavelength, we can use the value of normalized frequency to deduce bandgap position for crystals with different unit cell size. For example, for $a = 5.5 \mu\text{m}$ single gyroid crystal investigated in Figure 2.4b, the center of the bandgap can be inferred by a normalized frequency, resulting in a shift of the bandgap center by $0.6 \mu\text{m}$. Therefore, we identified a-Si as a suitable material with its high refractive index and low loss at mid-infrared wavelength. Another suitable candidate material is germanium, which has even higher refractive index ($n > 4$) and sufficiently low loss in this wavelength regime.

To fabricate a-Si single gyroid structures, we developed a protocol which incorporates multiple steps [14, 23, 24, 34, 35] (see Appendix A2 for detailed description), as illustrated in Figure 2.2. Two-photon lithography was utilized to directly write a sacrificial polymer scaffold of gyroid photonic crystals with unit cell sizes of 4.5, 5.1, and $5.5 \mu\text{m}$ on mid-infrared transparent silicon substrates. Each sample is composed of $20 \times 20 \times 10$ unit cells. We conformally deposited 40 nm thick aluminum oxide coatings on the polymer gyroids via atomic layer deposition (ALD) at $150 \text{ }^\circ\text{C}$. We then used focused ion beam (FIB) milling to remove the crystal sides to facilitate polymer removal, yielding a hollow inorganic aluminum oxide crystal after oxygen plasma cleaning. Subsequently, the structure was conformally coated and in-filled with a 100 nm a-Si layer at $350 \text{ }^\circ\text{C}$ using chemical vapor deposition (CVD). The polymer structure is not structurally stable at temperatures above $250 \text{ }^\circ\text{C}$, which are typically necessary for conformal deposition of high refractive index materials such as a-Si. Therefore, the hollow aluminum oxide crystal is a critical intermediate structure to provide a scaffold that can withstand high temperature. The final structure consists of a 40 nm middle layer of aluminum oxide and two 100 nm/150 nm a-Si layers on both the inside and outside of the aluminum oxide scaffold, corresponding to $u(x,y,z)$ values of 1.1/1.05, 1.2, 1.25, and 1.35/1.37 for coated a-Si, Al_2O_3 , in-filled a-Si and inner hollow part, respectively (see Table A.1

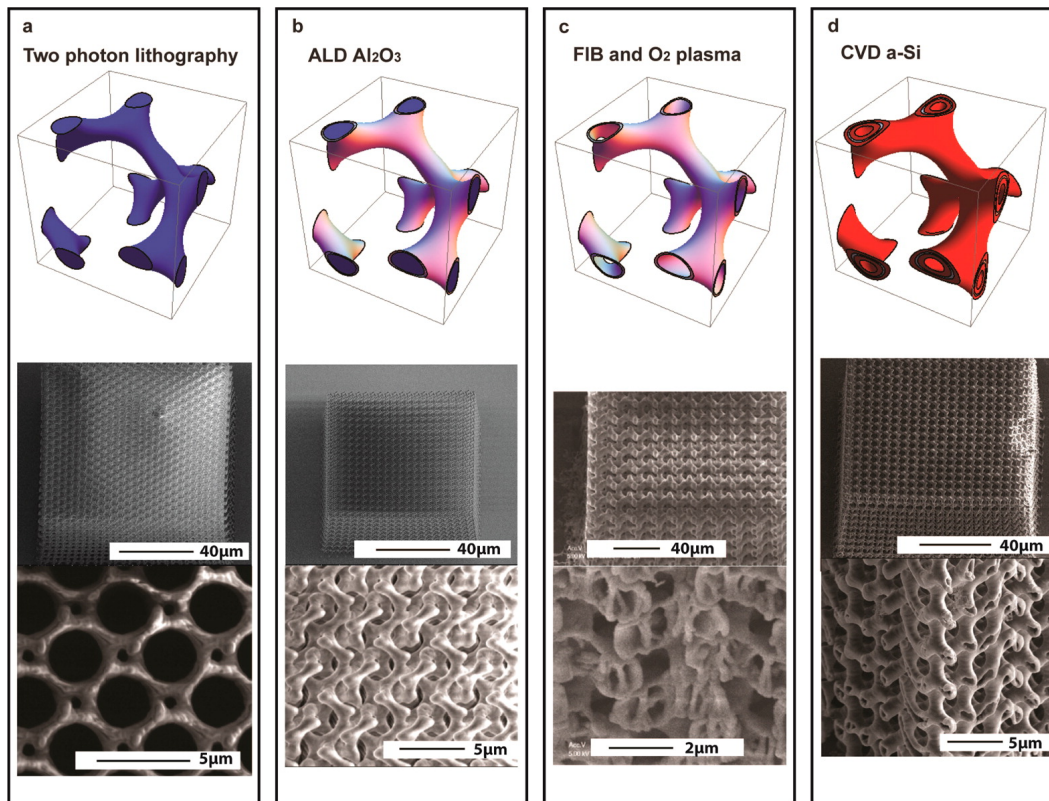


Figure 2.2: Fabrication procedures of gyroid photonic crystals. (a) Two-photon lithography to define a sacrificial polymer scaffold of the gyroid structure. (b) Atomic layer deposition of Al_2O_3 to coat the polymer structure. (c) Focused ion beam milling to remove the sides of the structure, followed by oxygen plasma to remove the polymer, leaving a hollow alumina structure. (d) Chemical vapor deposition of a-Si to coat and in-fill the hollow alumina structure.

for fill fraction values).

2.3 Fourier transform infrared spectroscopy characterization

We characterized the resulting a-Si single gyroid photonic crystals by Fourier transform infrared spectroscopy (FTIR), shown in Figure 2.3a (see Appendix A3 for a detailed description of the measurements). SEM images of the characterized sample are shown in Figure 2.3b. The reflectance spectrum of the $a = 4.5 \mu\text{m}$ sample reveals a peak of 98% at $7.0 \mu\text{m}$, as shown in Figure 2.3c (red dashed line), in agreement with the predicted reflectance peak center of the $4.5 \mu\text{m}$ trapezoidal structure in the figure above (black dashed line; see the Appendix A4 for Full Wave Simulation on Deformed Crystals), as well as the band gap center for a cubical single gyroid structure (gray dashed line). The reflectance of the sample is normalized to the

reflectance of an atomically smooth gold mirror of 97% reflectance. Additional 50 nm coating and in-filling of a-Si on the structure red-shifted the reflectance peak to 7.5 μm , giving rise to the 100% reflectance peak shown in Figure 2.3c (red solid line). The reflectance peak at 7.5 μm is a direct manifestation of a photonic bandgap. The transmittance spectrum shown in Figure 2.4a has a wide 0% transmittance band centered at 7.5 μm , confirming the bandgap. The extinction (scattering + absorption) is obtained by subtracting the transmittance and reflectance percentages from 100%. Since the FTIR collection angle is limited to 16°–34°, that part of the reflected light that lies outside of this angular range is considered as scattering here. These results reveal the photonic property of the single gyroid structure, namely, the optical bandgap in the mid-infrared regime.

We also characterized the reflectance spectrum of the $a = 5.1 \mu\text{m}$ period and $a = 5.5 \mu\text{m}$ period samples and compared them with that of the $a = 4.5 \mu\text{m}$ sample, as shown in Figure 2.4b. We observed a red shift of the reflection peaks by 0.6 μm in wavelength for the 5.5 μm period sample, and a shift of 0.4 μm in the 5.1 μm sample relative to the 4.5 μm sample, which is in agreement with the increase in the bandgap wavelength predicted (see Figures 2.1c and 2.5). This observation can be intuitively understood by considering the resonant coupling between the incoming beam and the cavity of a periodic unit cell. The agreement between our experimental results and simulations for three structures with different unit cell sizes confirms the mid-infrared bandgap feature of the single gyroid photonic crystals.

2.4 Discussion and conclusion

Several specific features arise in the reflectance spectra of these single gyroid samples due to practical aspects of the chosen material compositions and defects present in the crystal structures. The bandgap center of the 4.5 μm period structure is shifted from the predicted 8 μm wavelength inferred from Figures 2.1c and 2.3c (black dashed line) to the experimentally measured 7.0 μm wavelength in Figure 2.3c (red dashed line). This is due to lower effective refractive index of the a-Si/ Al_2O_3 /a-Si heterostructure present in fabricated samples as compared with an assumed homogeneous dense solid a-Si cross-section for the photonic crystal elements in the simulations given in Figure 2.1c. The center of the bandgap calculated from full wave simulation for the actual a-Si (100 nm)/ Al_2O_3 (40 nm)/a-Si (100 nm) composition is at 7 μm , shown in Figure 2.5. Another minor contribution comes from the lower refractive index in the experimental a-Si as compared to those of Palik(25) used in full wave simulations, shown in Figure A.1a, likely due to differences in the

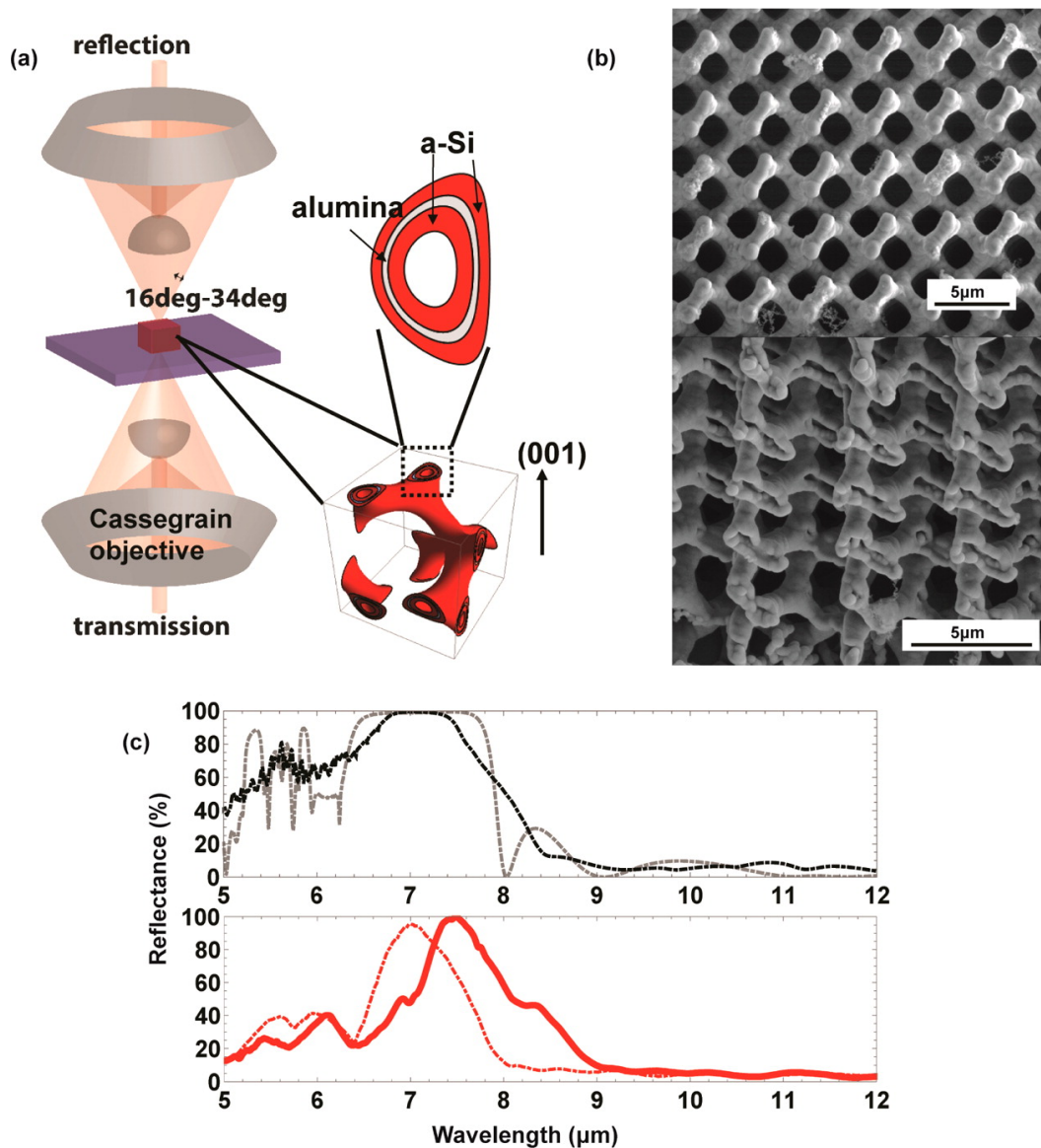


Figure 2.3: FTIR characterization of bandgaps. (a) Fourier transform infrared spectroscopy experimental configuration. (b) SEM images of a hollow gyroid at (001) crystal orientation with a-Si (150 nm)/ Al_2O_3 (40 nm)/a-Si (150 nm) layers. (c) Reflectance spectrum from full wave simulations of a hollow gyroid at (001) crystal orientation with a-Si (100 nm)/ Al_2O_3 (40 nm)/a-Si (100 nm) layers (gray dashed line), reflectance spectrum from full wave simulations of a trapezoidal hollow gyroid at (001) crystal orientation with a-Si (100 nm)/ Al_2O_3 (40 nm)/a-Si (100 nm) layers (black dashed line), FTIR measurement of a hollow gyroid with a-Si (100 nm)/ Al_2O_3 (40 nm)/a-Si (100 nm) layers (red dashed line), and FTIR measurement of a hollow gyroid with a-Si (150 nm)/ Al_2O_3 (40 nm)/a-Si (150 nm) layers (red solid line).

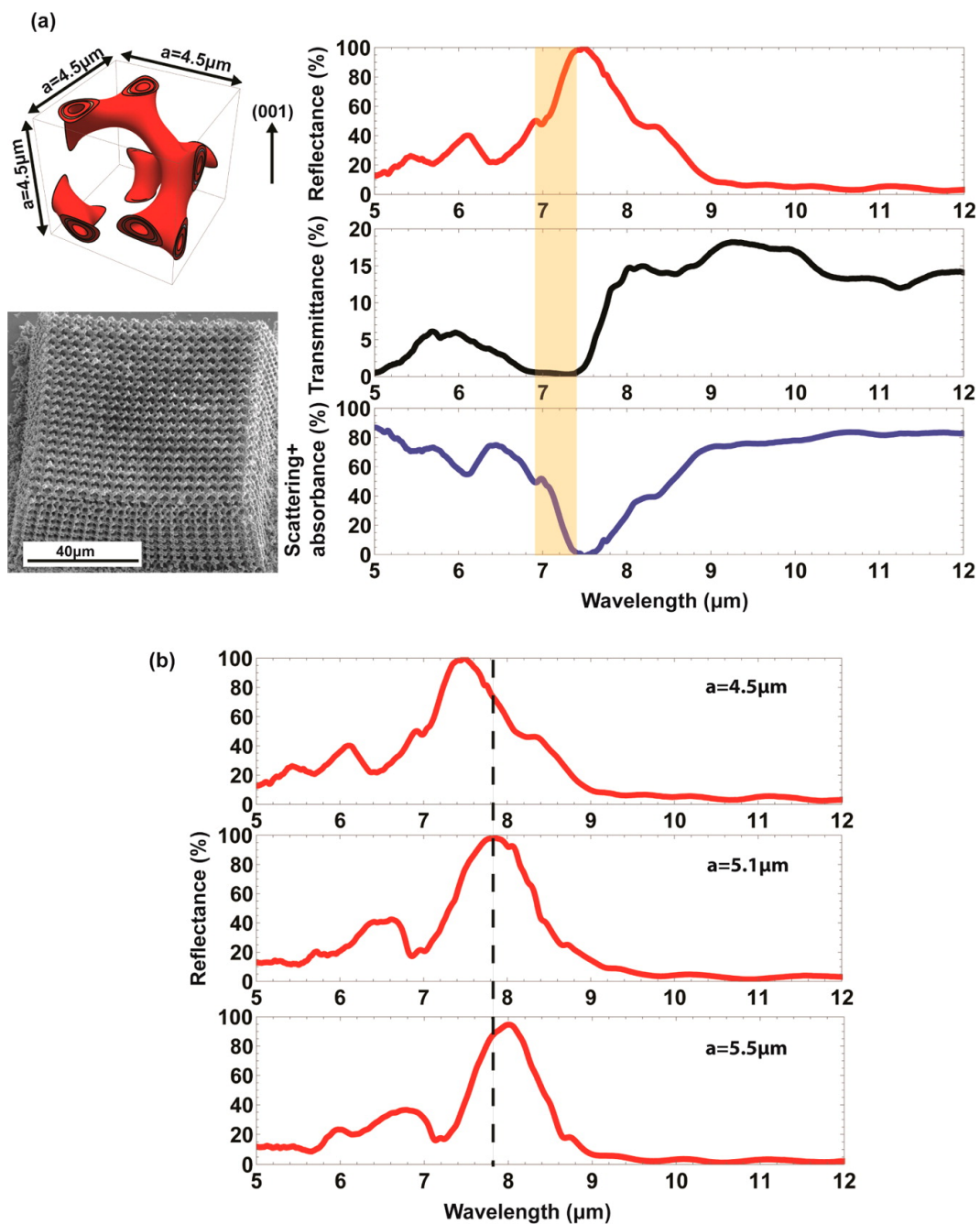


Figure 2.4: FTIR characterization of single gyroids. (a) Reflectance, transmittance, and scattering + absorbance from a single gyroid structure with unit cell size of $4.5\mu\text{m}$ and a total of $20 \times 20 \times 10$ cells. (b) Comparison of reflection spectra of samples with unit cell sizes of 4.5 , 5.1 , and $5.5\mu\text{m}$ ($20 \times 20 \times 10$ unit cells).

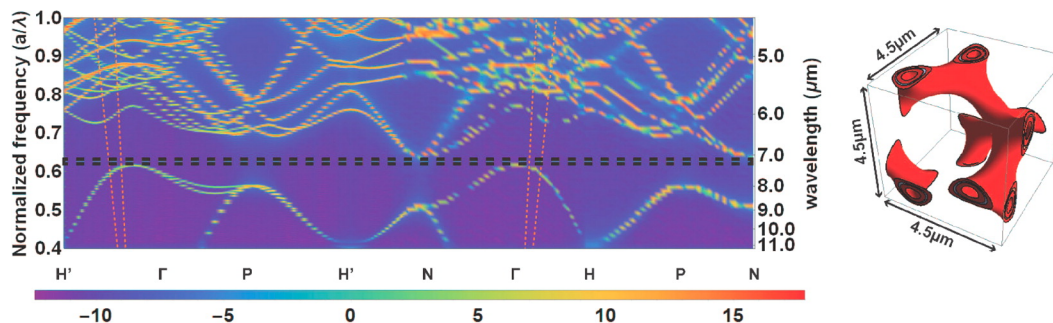


Figure 2.5: Photonic band structure simulation. Photonic band structure of a single gyroid consists of a-Si (100 nm)/ Al_2O_3 (40 nm)/a-Si (100 nm) layers from full wave simulations, with unit cell size of $4.5 \mu\text{m}$ in x, y, and z directions. Bands in between the orange lines are accessible through FTIR characterization shown in

deposition conditions.

The main crystal defect is a overall shape distortion of the lattice which is attributed to polymer shrinkage, as shown in SEM images in Figures 2.2 and 2.4, instead of the cubic shape expected in an ideal lattice. A trapezoidally shaped crystal is formed as the result of the polymer scaffold shrinkage. After direct laser writing, the written IP-Dip photoresist cross-links to form polymer scaffolds. The unwritten photoresist is then removed in the process of development, during which the top portion of the polymer scaffold shrinks. The adhesion force between the scaffold and the rigid Si substrate prevents the bottom lattice from shrinking. This distortion results in a decreasing unit cell size from the bottom to the top of the crystal, resulting in an overall trapezoidal shape for the crystal. In an ideal cubic crystal, we expect a 100% reflectance peak with bandwidth matching that of the predicted bandgap, shown in Figure 2.3c (black dashed line). A narrowing of the measured reflectance peak in Figure 2.3c (red dashed line) is expected when the trapezoidal shape is taken into account in the deformed crystal simulation (see Appendix A4, Full Wave Simulation on Deformed Crystals), together with the a-Si/ Al_2O_3 /a-Si material composition. Intuitively, the measured reflectance spectrum is a superposition of the scattering from each crystal layer over the range of momenta accessible by the 16° to 34° range of incident angles of the FTIR configuration shown in Figures 2.3a and 2.5 (orange lines). As the unit cell dimension increases from top to bottom of the trapezoidal shaped crystal, the reflectance peak center of each layer is increasingly red-shifted. The width of the measured reflectance narrows as a result of the effective inhomogeneity and the lowered effective refractive index. The second reflectance peak observed in Figure 2.4b, at $6.1 \mu\text{m}$ for the $a = 4.5$

μm sample, $6.5 \mu\text{m}$ for the $a = 5.1 \mu\text{m}$ sample, and $6.8 \mu\text{m}$ for the $a = 5.5 \mu\text{m}$ sample, respectively, can also be explained by this effective inhomogeneity. From reflectance simulations of an ideal a-Si gyroid crystal in Figure 2.3c (gray dashed line), distinct photonic bands exist above the band gap, manifested as sharp dips in the reflectance spectrum. The states observed in the reflectance spectra is equivalent of projected band structure on the (001) plane, spanned by Γ -H and Γ -H' symmetry directions. Band structure simulations in Figures 2.1c and 2.5 indicate photonic bands above the band gap. A trapezoidal shaped crystal gives rise to spectral inhomogeneity, and consequently the photonic band features broadens into one reflectance peak. Despite realistic material compositions and sample defects, the essential physics interpreted from these reflectance spectra is not affected by the above-mentioned nonidealities. In conclusion, we experimentally observed a 100% reflective bandgap at mid-infrared wavelengths in single gyroid photonic crystals with high refractive index materials, fabricated using two-photon lithography and conformal layer deposition, confirming photonic bandgap predictions obtained from simulations. This mid-infrared bandgap is also predictably tunable by changing the unit cell size in the simulation design and fabrication. The synthesis/characterization approach described here opens the door to design of more complex mid-infrared photonic crystals with topological states, such as Weyl points in double gyroid photonic crystal with parity-breaking symmetry, for which synthesis of single gyroid photonic crystals establishes feasibility. Further designs may also yield gyroid photonic structures whose surfaces exhibit topologically protected states, suggesting the possibility to synthesize these intriguing structures to create unusual states and phases of light.

Chapter 3

DOUBLE GYROID PHOTONIC CRYSTALS: SYNTHESIS AND ANGLE RESOLVED MID-INFRARED CHARACTERIZATION

Gyroid crystals are triply symmetric and have surfaces containing no straight lines. Single gyroid photonic crystals have a large band gap, while double gyroid photonic crystals bring quadratic point degeneracy into the band gap. Breaking the parity of double gyroids can be accomplished by introducing an air sphere, where the quadratic point lifts its degeneracy and forms a pair of Weyl points. Weyl points are the degenerate energy states resulting from band crossings of linear dispersion features in three dimensional momentum space. Unlike Dirac points in two-dimensional systems, Weyl points have been shown to be stable and the associated surface states are predicted to be topological with non-trivial Chern number. These topologically protected surface states give rise to various interesting phenomena such as backscattering immune unidirectional transport.

We have synthesized and characterized the first mid-infrared (Mid-IR) gyroid photonic crystals, including both single and double gyroid crystals with Weyl points present, in the Mid-IR regime. Simulations reveal that gyroids must be composed of high refractive index materials such as a-Si in order for gyroids to possess interesting properties such as band gaps and Weyl points. Two-photon lithography was utilized to write polymer gyroid scaffold with unit cell sizes of 4-6 μm composed of 40x40x5 unit cells, on intrinsic Si substrates. We inverse the structure by atomic layer deposition of Al_2O_3 until the surface of the gyroid is closed. We then perform reactive ion etching of Al_2O_3 with Cl_2 to facilitate polymer removal, yielding a hollow inversed Al_2O_3 structure. The inversed structure was then conformally coated and in-filled with a-Si. Lastly, we remove the Al_2O_3 structure with phosphoric acid. The resulting double gyroids have unit cell sizes of 4.68 μm oriented along [001] direction, with Weyl points at 8 μm and k between $0.3\pi/a$ and $0.5\pi/a$. Characterization of single and double gyroid photonic crystals has been performed by angle resolved spectroscopy with a quantum cascade laser. The photonic crystal bandstructure is constructed from angle resolved reflectance and transmittance spectra, all the way close to the light line. Constructed bandstructures from single gyroids clearly exhibit a photonic bandgap. Characterization from double gyroids reveals defect photonic states emerging inside the bandgap. Measured bandstructures of

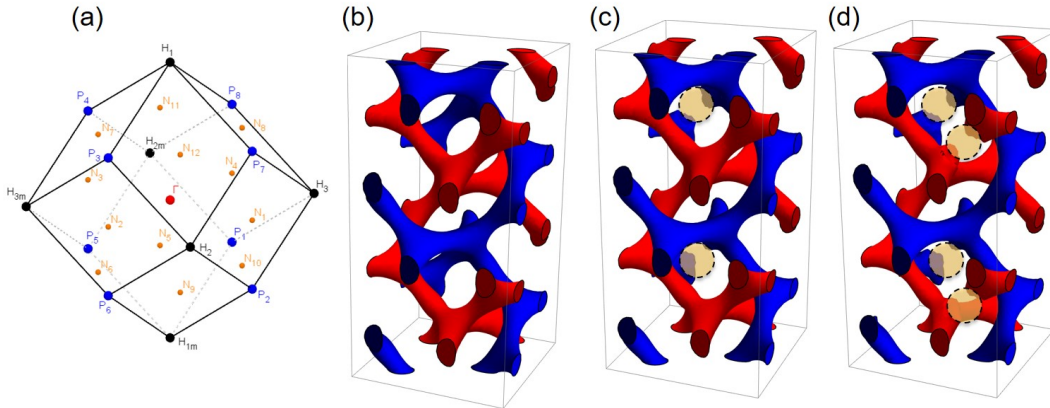


Figure 3.1: (a) BCC Brillouin zone (b) Double gyroids (c) Double gyroids with an airsphere which breaking parity symmetry (d) Double gyroids with two airspheres

single and double gyroids are compared with simulated bandstructures projected based on crystal orientation.

3.1 Introduction

Topological insulators are an emerging class of material that has exceptionally interesting physical phenomenon[2]. Topological edge/surface states, which exist on the edges/surfaces of topological insulators, are unidirectional and backscattering immune. These remarkable transport properties enable exciting applications, such as quantum computers and other semi-conductor and optical communication devices. Topologically protected surface states can be realized in three-dimensional photonic crystals. Double gyroid photonic crystals have been predicted to be a candidate of three-dimensional photonic topological insulators at microwave wavelength.

The group symmetry of single gyroid structures, which are introduced in the last chapter, can be varied by introducing its spatial inversion partner and forming a double gyroid structure, shown in Figure 3.1b. Double gyroid photonic crystals are predicted to have a pair of line nodes emerging inside the bandgap[11]. Breaking of parity inversion symmetry or breaking of time reversal symmetry in the double gyroid photonic crystal give rise to a pair of novel topological states known as Weyl points from the line nodes. Weyl points are the degenerate energy states resulting from band crossings of linear dispersion features in three dimensional momentum space[11]. Unlike Dirac points in two-dimensional systems, Weyl points have been shown to be stable. The concept of Weyl points was first derived by Hermann Weyl

to be a massless solution to the Dirac equation in the context of high energy particles. Until today, Weyl fermions are yet to be experimentally realized in high energy physics. On the other hand, with the advances of condensed matter physics and photonics, Weyl points have been observed in low energy systems in various forms, such as electronic dispersion in crystalline materials and centimeter-scale photonic crystal in the microwave regime[11, 21, 36]. Surface states associated with Weyl points are predicted to be topological with non-trivial Chern number[11]. Our research on double gyroid photonic crystal focuses on achieving the change of wavelength from microwave to mid-infrared for the double gyroid geometry, which entails a whole new level of challenges in synthesis at nanoscale and optical characterization techniques. In this work, we report a synthesis strategy for forming mid-infrared double gyroid photonic crystals with high-refractive index materials, and a mid-infrared characterization technique to map out momentum resolved photonic band structures.

3.2 Frequency domain simulation method of double gyroids

We start out by simulating bandstructures of double gyroid, to determine appropriate unit cell sizes and materials for desired band structures. Simulations are performed with MIT photonic band solver. Double gyroid band structures are shown in Figure 3.2, with unit cell size of $4.7\mu\text{m}$ and refractive index of 3.5. The complete band gap of single gyroid structures are indicated by the yellow rectangle, from $7.5\mu\text{m}$ to $9.5\mu\text{m}$. For double gyroid, we observe quadratic degeneracy points appear inside the bandgap at the Γ point. In Figure 3.3, we compare band structures of three different types of double gyroid structures: double gyroids, double gyroids with parity breaking symmetry, and double gyroids with airspheres with parity symmetry. For double gyroids with parity breaking symmetry, the quadratic points from double gyroids are further hybridized and therefore result in band inversion. The degenerate quadratic points at $8\mu\text{m}$ at the Γ point are now inverted to 7 and $8\mu\text{m}$ respectively. For double gyroids with two airspheres, line nodes form at $7.5\mu\text{m}$, which is a closed loop in the Brillouin zone of generate states.

Alternatively, parity symmetry can be broken by placing a thin cylinder in place of an airsphere. We compare band structures from the two different ways of breaking parity symmetry, shown in Figure 3.4a for the airsphere case and Figure 3.4b for the thin cylinder case. Although the band inversion in Fig 3.4b is compared to the band inversion in Figure 3.4a, by changing radius and length of the cylinder, the degree of band inversion could be tuned. The thinner and longer the cylinder is, the more

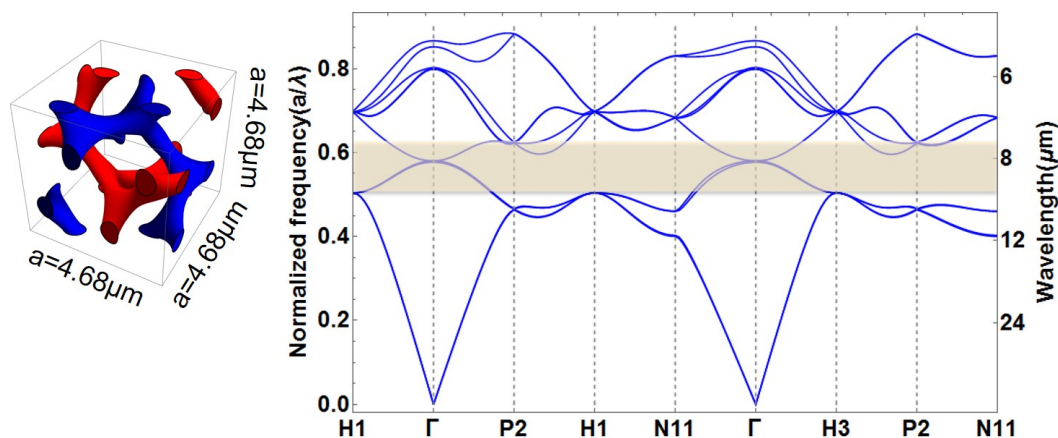


Figure 3.2: Band structures of double gyroids with unit cell size of $4.68\mu\text{m}$

the band inverses.

3.3 Three-dimensional band structure projection onto a two-dimensional plane

For experimental characterization, three-dimensional band structures are projected onto a two-dimensional plane perpendicular to the crystal orientation, illustrated in Figure 3.5. The projection plane is the purple rectangle, spanned by Γ -H2 and Γ -H3, where the projection direction is illustrated by the red arrow. Projected band structures are convoluted along the Γ -H1, while the resolution is kept within the projection plane. To simulate projected band structures, we compute 3D band structures, and superimpose them along the [001] (Γ -H1) direction. Figure 3.6 is the projected simulation of double gyroid band structures along the Γ -H2 and Γ -H3 direction. The quadratic point degeneracy can be observed in both directions. Figure 3.7 is the projected simulation of Weyl points (parity breaking symmetry) band structures along the Γ -H2 and Γ -H3 direction. The pair of Weyl points reside inside the plane spanned by Γ -H3 and Γ -N11. Therefore, after the [001] direction projection, two of the Weyl points could be observed along the Γ -H3 direction, close to the light line (red line). Figure 3.8 is the projected simulation of line nodes (parity symmetry) band structures along the Γ -H2 and Γ -H3 direction, where similarly degenerate line nodes could be observed along the Γ -H3 direction.

3.4 Synthesis of double gyroid photonic crystals

To synthesize the three photonic crystals, we start by define the polymer scaffold using two-photon lithography, shown in Figure 3.9a. The polymer scaffold is then

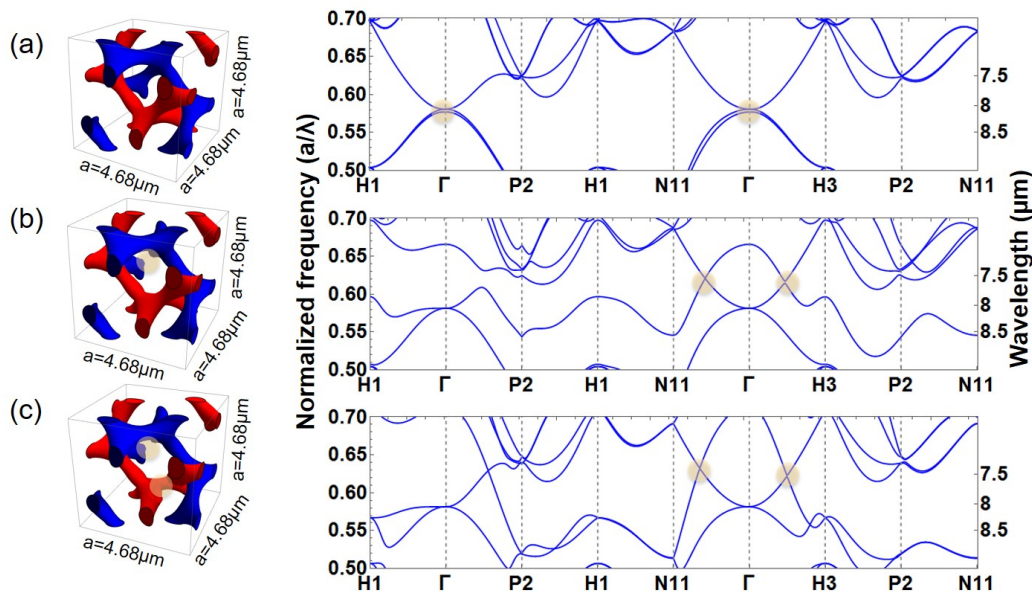


Figure 3.3: Band structures of double gyroids with unit cell size of $4.68 \mu\text{m}$ (a) Double gyroids with quadratic point degeneracy (indicated by yellow circles) (b) Double gyroids with Parity breaking symmetry, which give rise to a pair of Weyl points. The Parity breaking airsphere is indicated by the yellow circle in the unit cell. Weyl points are indicated by the yellow circles along Γ -N11 and Γ -H3. (c) Double gyroids with two air spheres in one unit cell (indicated by yellow circles). Line nodes are indicated by yellow circles Γ -N11 and Γ -H3.

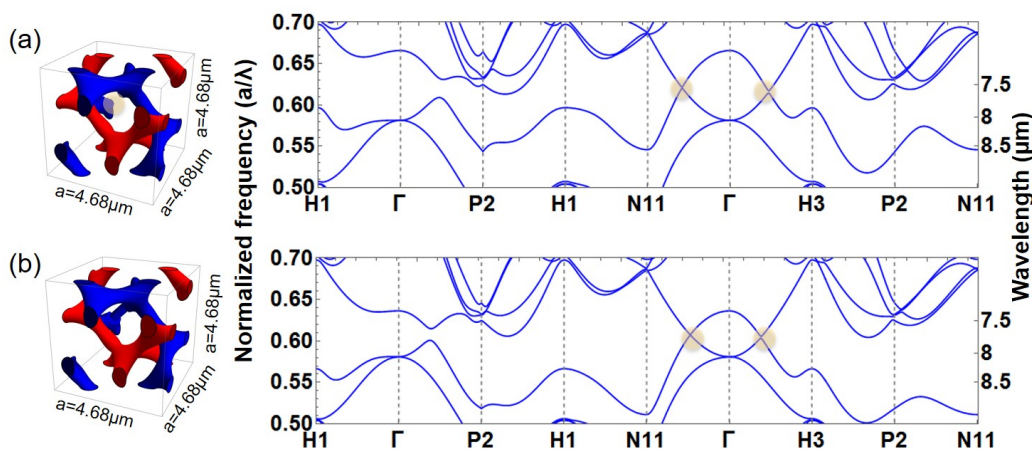


Figure 3.4: Band structures of double gyroids with unit cell size of $4.68 \mu\text{m}$ (a) Double gyroids with parity breaking symmetry by an airsphere, which give rise to a pair of Weyl points. The parity breaking airsphere is indicated by the yellow circle in the unit cell. Weyl points are indicated by the yellow circles along Γ -N11 and Γ -H3. (b) Double gyroids with Parity breaking symmetry by a thin cylinder, which also give rise to a pair of Weyl points along the same symmetry directions. The parity breaking cylinder is placed at the spatial position as the airsphere.

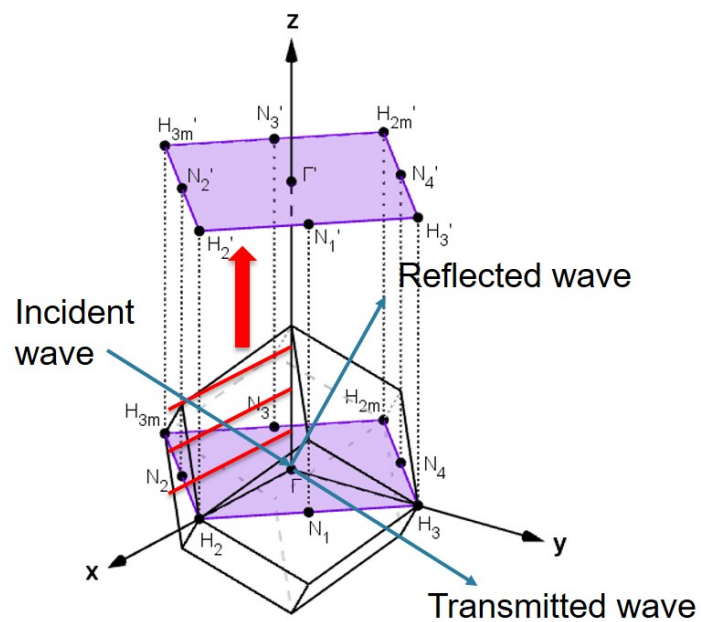


Figure 3.5: Illustration of 3D band structure projection onto a 2D plane, along the Γ -H1 direction.

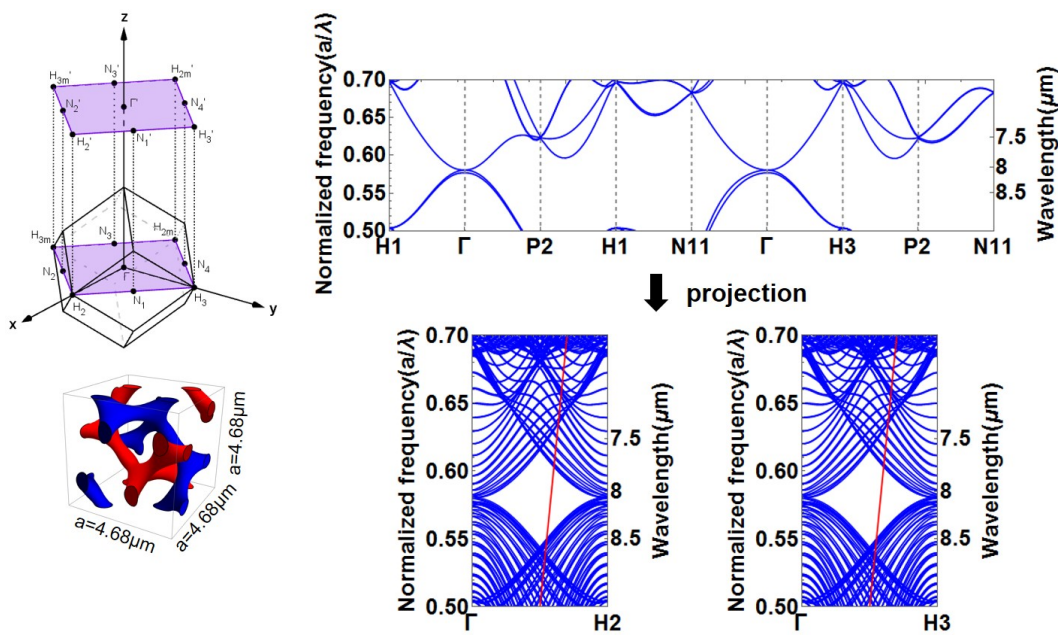


Figure 3.6: Projection of double gyroid band structures along the [001] direction.

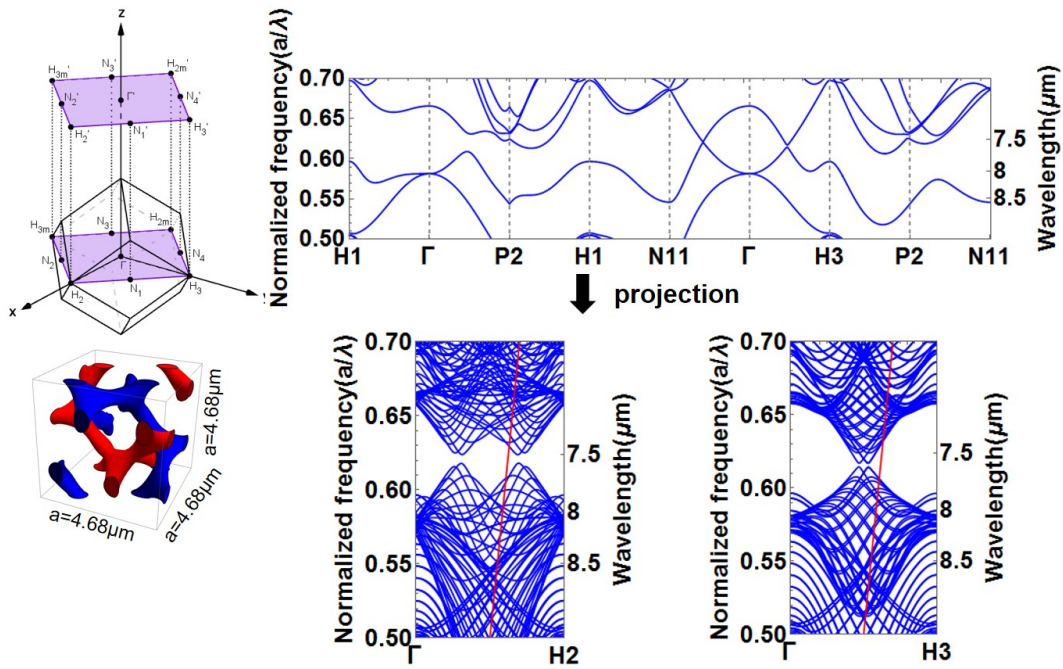


Figure 3.7: Projection of Weyl points band structures along the [001] direction.

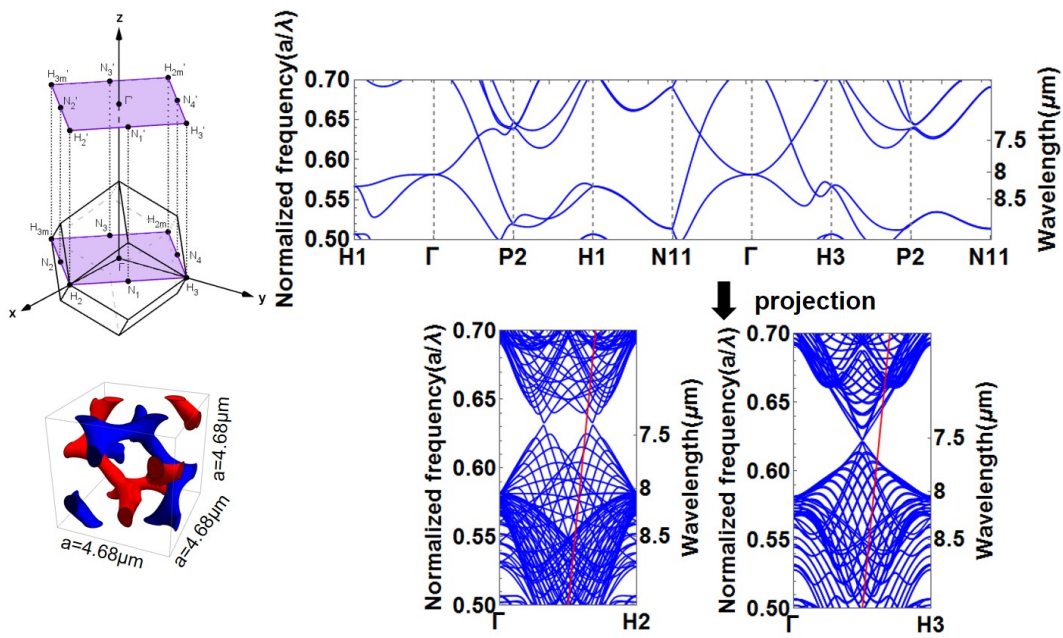


Figure 3.8: Projection of line nodes band structures along the [001] direction.

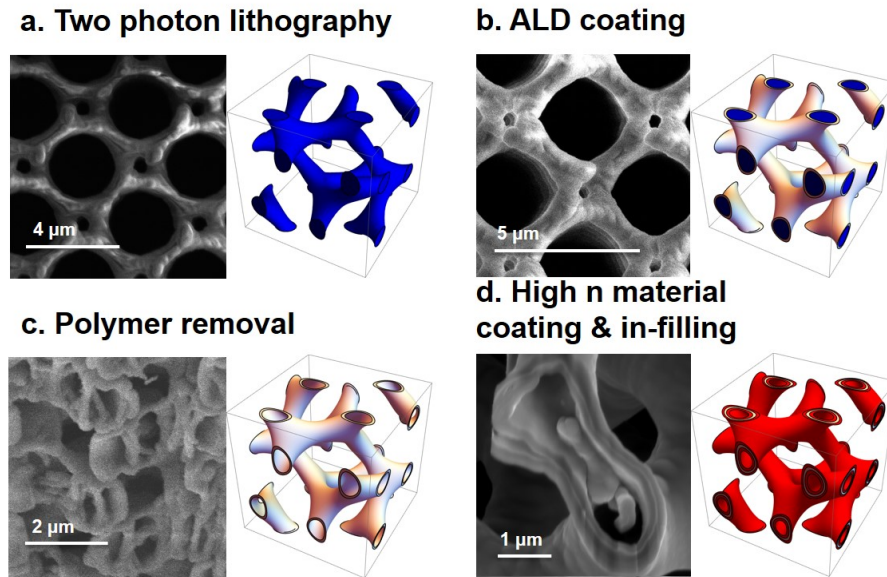


Figure 3.9: Synthesis of three-dimensional photonic crystals with high-refractive index materials.

coated with aluminum oxide or silicon dioxide by atomic layer deposition, shown in Figure 3.9b. We then facilitate polymer removal by removing sides of the photonic crystals with focused ion beam milling. After oxygen plasma cleaning, we obtain a hollow oxide scaffold of the photonic crystal, shown in Figure 3.9c. The hollow oxide scaffold is then conformally coated and in-filled with high refractive index material such as a-Si via static chemical vapor deposition. Then cross sectional image of the three-dimensional photonic crystal in Figure 3.9d consists of a-Si/ Al_2O_3 /a-Si. Note that this method is also applicable for other high refractive index material. For example, a-Ge can be deposited using the same method as a-Si. Other viable material candidate include TMDC material such as MoS_2 and WS_2 . For example, Mo_2O_3 can be conformally deposited by ALD process, and then converted to MoS_2 via sulfication.

3.5 Angle resolved mid-infrared spectroscopy

For initial optical characterization of double gyroids, we utilize FTIR, which is illustrated in Figure 3.10a. Results of reflectance spectra from single gyroid (red), double gyroids (blue) and double gyroids with parity breaking symmetry are shown in Figure 3.10b. While we observe a reflectance peak from single gyroid corresponding to the photonic bandgap, the reflectance peak decreases for double gyroid structures, as a result of emergence of photonic states inside the bandgap. However,

reflectance and transmittance spectra from FTIR give us convoluted momentum space information. In order to observe novel photonic states such as line nodes and Weyl points in double gyroid photonic crystals, I designed and built an optics set up that can perform angle resolved spectroscopy with a quantum cascade laser, shown in Figure 3.11. The set up consisted of a quantum cascade laser as the source, series of ZnSe lenses to expand and refocus the laser beam into a $75\mu\text{m}$ diameter spot and germanium beam splitter to direct 50% of the laser beam to the reference detector and 50% to the sample. Two The sample and the pyroelectric detector are mounted on top of concentric rotation stages to collect transmission and reflection at different incidence angles. Alignment of the laser beam and the photonic crystal sample is first performed by a visible CCD camera with a telescope lens. Then more precise alignment is performed by a magnifying lens and the magnified image is projected onto a MCT camera. The angle of spread for beam focusing onto the sample is 8° . The wavefront of the beam is defined by:

$$E(r, z) = E_0 \frac{\omega_0}{\omega(z)} \exp\left(\frac{-r^2}{\omega(z)^2}\right) \exp\left(-i\left(kz + k\frac{r^2}{2R(z)} - \Phi(z)\right)\right) \quad (3.1)$$

where z is the axis of wave propagation, and $R(z)$ is the radius of curvature of the beam defined by:

$$R(z) = z\left(1 + \left(\frac{z_R}{z}\right)^2\right) \quad (3.2)$$

At the focal point, $z=0$ $kz=0$, and $R(z)$ approaches infinity, effectively we get a plane wave wavefront.

The photonic crystal bandstructure is constructed from angle resolved reflectance and transmittance spectra, all the way close to the light line. The set up is capable to perform both normal incidence characterization, shown in Figure 3.12 and off normal incidence characterization, shown in Figure 3.13. To start off, we characterize a double side polished silicon substrate, shown in Figure 3.14a and b. We observe clear Fabry-Perot resonance in both reflectance and transmittance characterization. The reflectance characterization is also in agreement both in wavelength and momentum compared to reflectance simulation shown in Figure 3.14c. Characterization from double gyroids, oriented along [001] direction, reveals defect photonic states emerging inside the bandgap. Measured bandstructures of double gyroids shown in Figure 3.15b, are compared with simulated bandstructures projected based on crystal orientation shown in Figure 3.15a. The double gyroid photonic crystal we characterize here has a unit cell compression in the z direction by 70%. In this case, the quadratic degeneracy point moved from the Γ point towards H3, which is

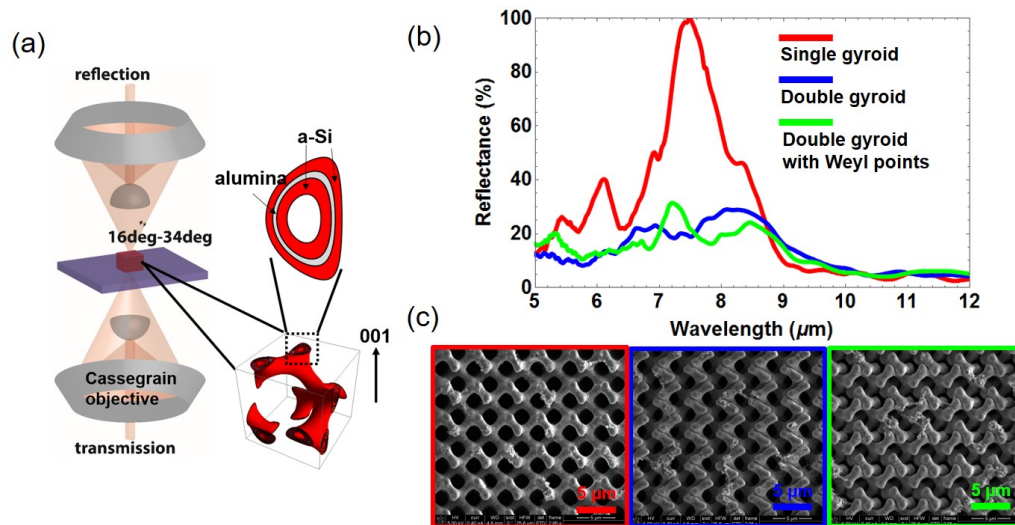


Figure 3.10: FTIR characterization of double gyroids: (a) Illustration of FTIR set up (b) Reflectance spectrum from single gyroid (red), double gyroids (blue) and double gyroids with parity breaking symmetry (green) (c) SEM images of single gyroid (red), double gyroids (blue), and double gyroids with parity breaking symmetry (green)

taken into consideration for the simulation shown in Figure 3.15a. The experimental characterization has good correspondence at the degeneracy point compared to simulations.

Compared to FTIR, the characterization used here has selectively excite photonic states at desired momentum and wavelength, providing more subtle information of the bandstructures essential for characterizing defect states and surface states. To resolve the subtlety of Weyl points, the degenerate energy states resulting from band crossings of linear dispersion features in three-dimensional momentum space, such characterization method is indispensable.

3.6 Conclusions and outlook

In summary, we aims to investigate topological phenomenon in 3D photonic crystals, which is both a new platform to design high efficiency photonic devices and a playground for new physics. We have developed a synthesis method to fabricate high refractive index three-dimensional photonic crystals, not limited to a-Si. To characterize photonic states such as Weyl points in double gyroid photonic crystals, we have constructed angle resolved transmission/reflection set up which enable us to construct photonic bandstructures in the mid-infrared with momentum resolution. Our future goal is to design and experimentally demonstrate topological properties

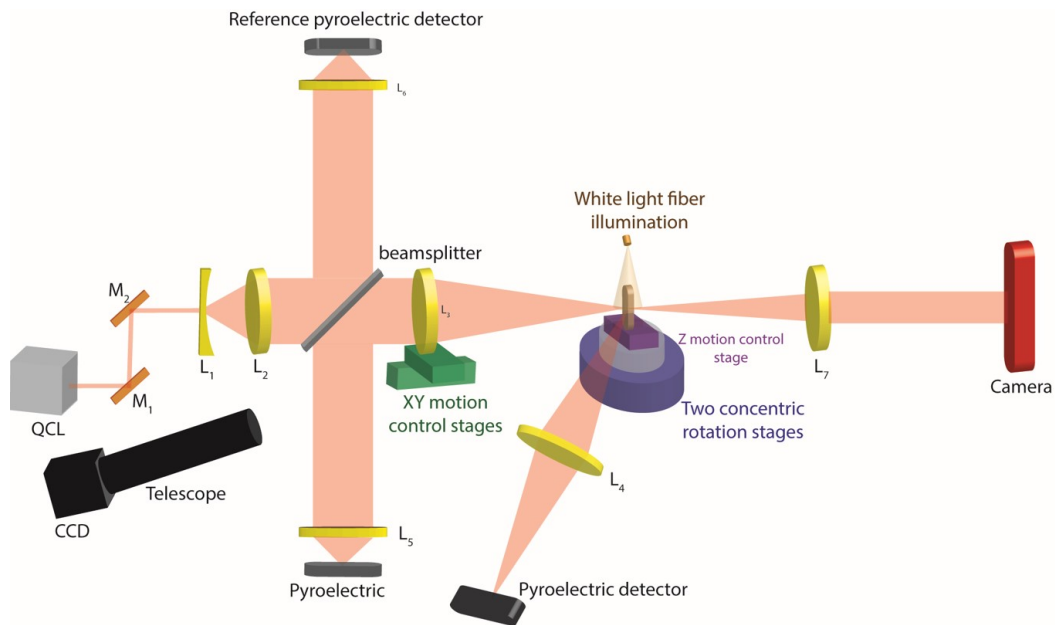


Figure 3.11: Photo of angle resolved characterization set up

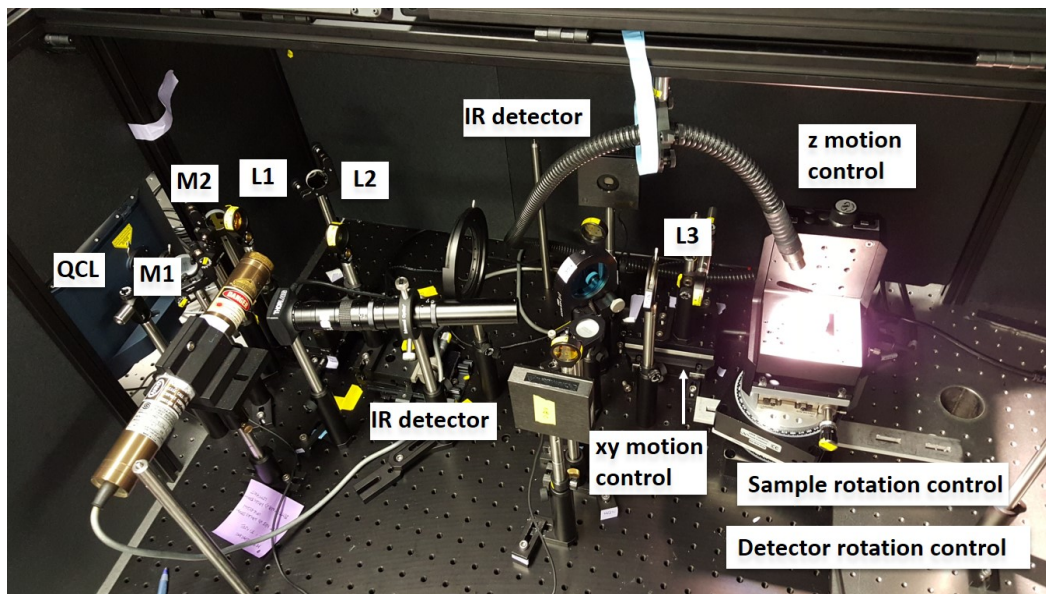


Figure 3.12: Angle resolved characterization set up for normal incidence reflectance measurement

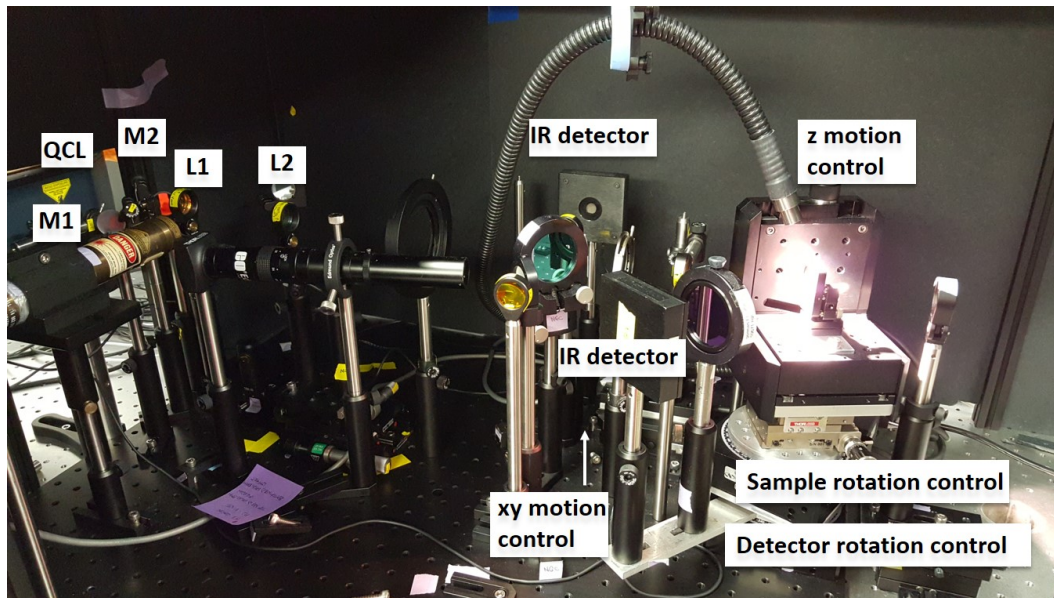


Figure 3.13: Angle resolved characterization set up for off normal incidence measurement

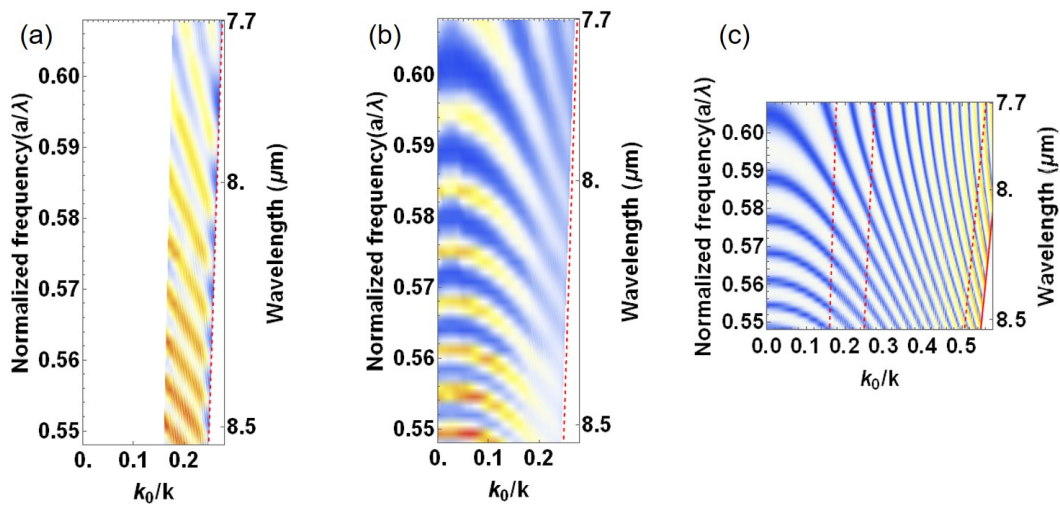


Figure 3.14: Fabry-Perot resonance from silicon substrate (a) reflectance (b) transmittance (c) simulated reflectance

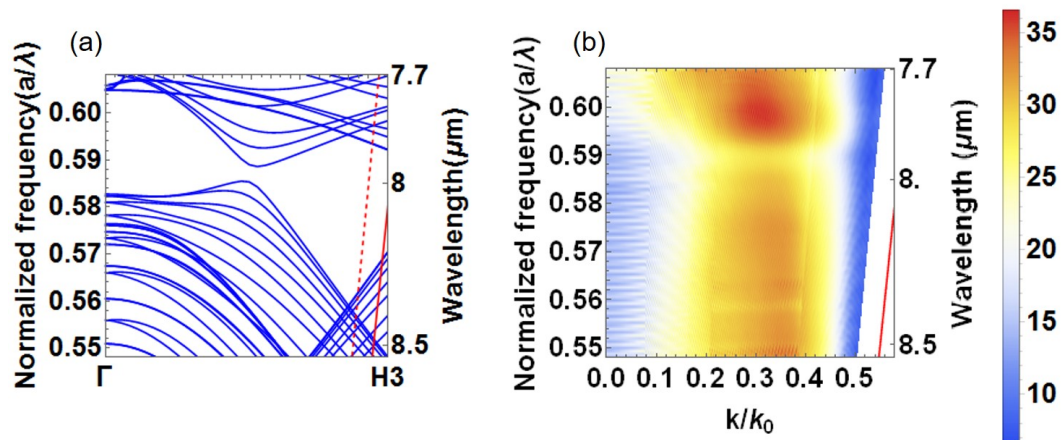


Figure 3.15: Double gyroid photonic band structures (a) simulation (b) experimental characterization

of double gyroid photonic crystals.

*Chapter 4***DIRAC-LIKE PLASMONS IN SILVER NANOPILLAR
HONEYCOMB LATTICES: DESIGN, FABRICATION AND
CATHODOLUMINESCENCE CHARACTERIZATION**

Surface plasmons in honeycomb lattices of Ag nanoparticles exhibit Dirac-like band structures, similar to the electronic band structure of graphene[37, 38]. Full wave simulations for an infinite honeycomb lattice of silver nano-pillars reveal hybridization of localized plasmonic modes between two neighboring pillars and the consequent formation of bonding and anti-bonding modes that are energetically degenerate at Dirac points with a relative phase of π . Calculations also reveal that distortion of the honeycomb lattice breaks the lattice inversion symmetry and opens a photonic bandgap, whose width is proportional to the extent of distortion. Furthermore, electromagnetic simulations reveal the existence of Dirac-like plasmonic edge states in finite width nanoribbons of the honeycomb nanoparticle lattice. Nanoscale architecture of the honeycomb lattice may provide a new way to control directional plasmon propagation by selective excitation of surface plasmon edge states without backscattering.

Experimentally, we have utilized cathodoluminescence (CL) spectroscopy to study angular emission patterns at various wavelengths and eventually construct band structures of the silver pillars in honeycomb lattices. In a CL measurement, electron beams are incident on the sample to excite plasmonic modes in the out of plane direction, which is normally difficult to excite via optical measurement. The scattered light due to the decay of surface plasmon excitations is collected by a parabolic mirror and mapped to the momentum space, yielding a direct construction of band structures in the Brillouin zone. In our initial CL measurement, we compared angular emission patterns from a single silver pillar, silver pillar dimers and silver pillars in honeycomb lattices fabricated on a 15 nm thick free standing silicon nitride membrane. The angular emission patterns from a single silver pillar exhibits strong dipole radiation, while silver pillars in dimer have directional radiation resulting from dipole interactions. For silver pillars in honeycomb lattices, we have observed strong radiation patterns near the Brillouin zone edge, integrated over an interval of wavelength including the wavelength of the Dirac points.

4.1 Introduction

Surface plasmons are coherent oscillation of electron waves at the interface of metal and dielectric. Beyond having propagating surface plasmon waves which exist at a planar interface or localized surface plasmon waves which exist at a closed interface, there are different ways surface plasmon dispersions could be engineered. For example, a metal insulator metal structure, an insulator insulator metal structure, or an insulator metal insulator structure could modify the dispersion to achieve negative refraction[39]. Similarly, coupling between plasmonic modes could also introduce interesting dispersion relations. For example, in closely spaced gold nano-particle chains both transverse and longitudinal modes were observed that are distinctively different from single particle resonances[40]. We study a metamaterial of graphene-like structure, which exhibits interesting Dirac-like surface plasmon dispersions[37, 38]. Graphene has particularly interesting honeycomb lattice structures, which consist of triangular Bravais lattice A and B, shown in Figure 4.1. Each unit cell consists of two atoms A and B. The fact that electrons can hop between A and B has given rise to interesting physical phenomenon of Graphene such as Dirac bandstructures and nontrivial topological properties. In our work, we investigate nanoparticles in a honeycomb lattice, in the hope that coupling between these particles can also give rise to interesting dispersion relations and novel optical properties.

4.2 Tight binding model

The Hamiltonian of the nano-particles in honeycomb lattices can be written in the following form:

$$H = \sum_{i=A,B} \sum_{r_i} \frac{p_i^2(r_i)}{2N_e m} + \frac{N_e m}{2} \omega_0^2 q_i^2(r_i) + \frac{e N_e}{\epsilon_m a^3} \sum_{r_B} \sum_{j=1}^3 q_B(r_B) q_A(r_B + e_j) \quad (4.1)$$

where $\frac{p_i^2(r_i)}{2N_e m}$ is the kinetic energy term, $\frac{N_e m}{2} \omega_0^2 q_i^2(r_i)$ is the potential energy term for each individual particles and $q_B(r_B) q_A(r_B + e_j)$ is the dipole dipole interaction term for two particles within a unit cell. Solution of the Hamiltonian reveal the dispersion relation shown in Figure 4.2a, which is very similar to electronic bandstructures of Graphene, with Dirac like linear dispersion at K points. Illustrated in Figure 4.2, this type of dispersion relations are results from hybridization of electric dipole modes on lattice sites A and B in the same unit cell. The red dashed horizontal line that

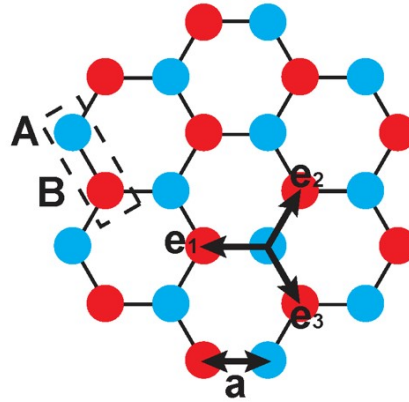


Figure 4.1: Honeycomb lattices with lattice constant a and lattice vectors e_1 , e_2 , and e_3 ; one unit cell of the lattice has two lattice sites: A and B.

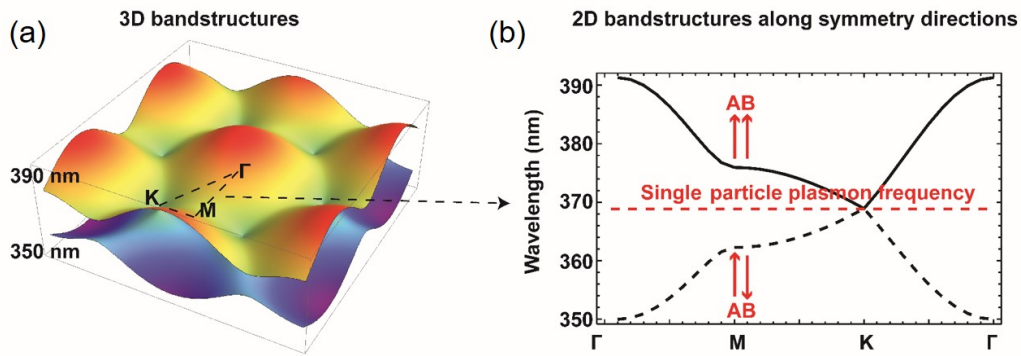


Figure 4.2: Dirac-like surface plasmon bandstructures: (a) three-dimensional bandstructures with six Dirac points, (b) two-dimensional bandstructures along high symmetry directions of the hexagonal lattice

crosses the Dirac point corresponds to the single dipole resonance, and the upper and lower band dispersions correspond to in-phase and out-of-phase modes.

4.3 Full wave finite-different time-domain design of Dirac-like plasmons

We performed numerical full wave simulation with FDTD method to verify the analytical model. We used dipoles as the excitation source and point monitors that collect electric field over time with periodic boundary conditions. Then we perform Fourier transform of the electric field over time to obtain the spectrum that reveal modes. By adding phase to the periodic boundary condition, modes at different wavevectors are calculated. Simulations verify that we have Dirac-like band structures as shown in Figure 4.3a. The symbol $\Delta\lambda$ represent separation of the upper band with the lower band at the M point, which is proportional to the degree of

hybridization.

How to increase hybridization of the modes is one of the key questions we would like to answer here. In figure 4.3b, the black curve is $\Delta\Lambda$ for the analytical model at different nearest neighbor distances. To be able to experimentally resolve the Dirac point, we need to increase the hybridization. In the analytical model, hybridization between nanoparticles is weak since there is very little field overlap in between the particles. Instead, we simulated nanopillars, which effectively increase the mode overlap between A and B particles, therefore coupling strength is increased. In figure 4.3b, We simulate nanopillars of several different ratios and material dielectric constants from different models. Purple dots and orange dots are simulations from nanopillars with aspect ratio=1 and dielectric constants from Palik and Drude model respectively. Red and Blue dots are simulations from nanopillars with aspect ratio=3.75 and dielectric constants from Palik and Drude model respectively. While the hybridization trend agrees with the analytical model, such that when particles get closer, hybridization increases, We observe that as the particles get taller, hybridization increases as well. For taller particles, there is more mode overlap and therefore hybridization strength increases. Other factors, such as loss in materials defects, could decrease the hybridization strength. For example, the red dots which are simulated with Palik dielectric constants considering loss have less hybridization strength compared to blue dots which are simulated with Drude model without loss. Mode profiles shown in Figure 4.4 further verify that formation of the bands are due to the hybridization between particles. There mode profiles are from the upper band and lower band of M point. From these simulations, we can clearly see that in the upper band at longer wavelength, the adjacent particles are in phase to each other. At shorter wavelength, the particle of respectively different lattices have flipped sign to form out of phase mode. At the K point, the modes are from upper and lower bands are superimposed with a relative phase shift of Π . In order to study the edge modes of these structures, we open the gap at the Dirac point by breaking the spatial inversion symmetry. We break the inversion symmetry by shifting the A lattice point (red dots), relative to the B lattice point (blue dots). When we shift the lattices relatively by 10nm, we observe an opening of the gap at the Dirac point without much perturbation of the overall band structure, shown in Figure 4.5b. We have further investigated the correlation between the lattice shift and gap opening, and found a very linear relationship between the two parameters, shown in Figure 4.5a. Under material condition of both the Drude model and Palik data, the gap opening and lattice shift remain linearly correlated. The gap opening is also linearly related

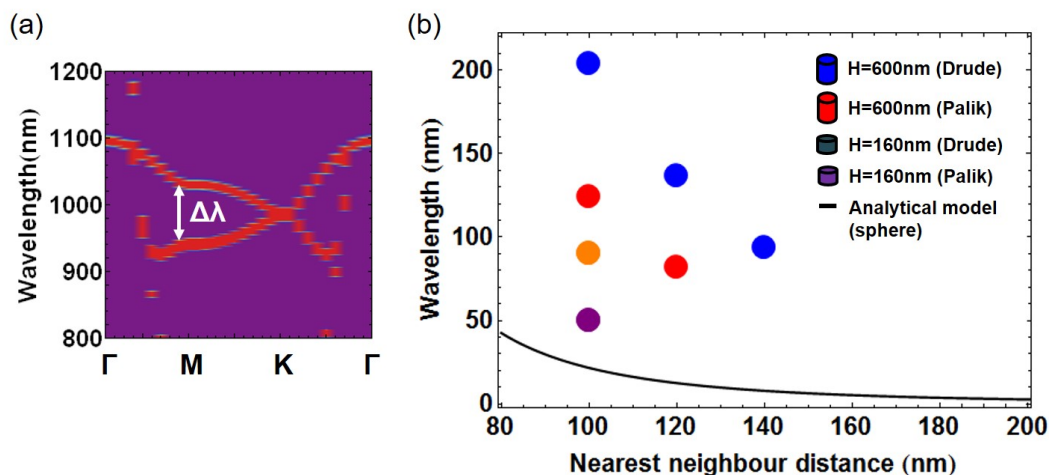


Figure 4.3: (a) Full wave simulations of bandstructures of silver nanopillars in honeycomb lattices ($r=80\text{nm}$, $h=160\text{nm}$ with a Drude model approximation for silver dielectric constants) (b) Degree of hybridization ($\Delta\lambda$) as a function of lattice sites separation and aspect ratio of individual lattice sites

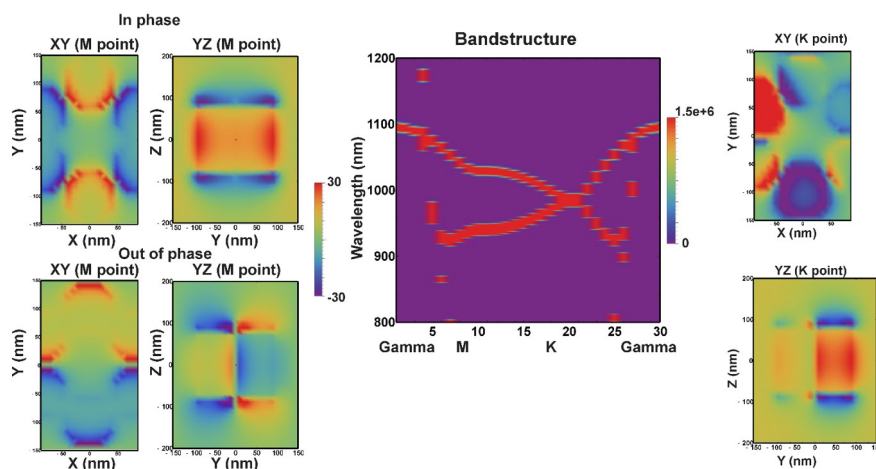


Figure 4.4: Electric field distribution of silver nanopillars at the M point and the K point

to lattice shifts at different heights of the nanopillars.

4.4 Fabrication of silver nanopillar honeycomb lattices

To experimentally study these structures. We use electron beam lithography to fabricate these structures on 12nm thin silicon nitride membranes, which are suitable the substrates for cathodoluminescence spectroscopy. The fabrication procedures are shown in Figure 4.6. We spun two layers of resist: PMMA 495 as the bottom layer and PMMA 950 as the top layer. Then we use electron beam lithography to define

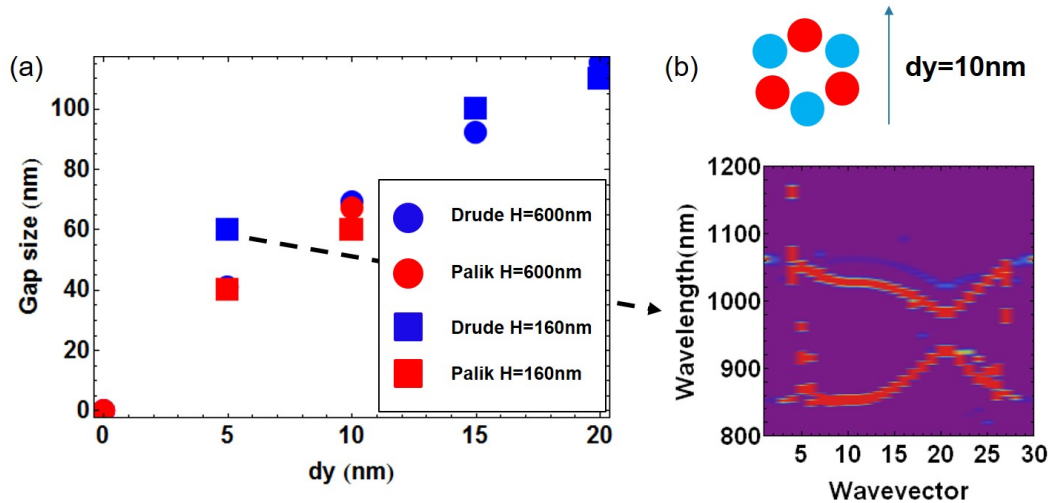


Figure 4.5: Opening a bandgap at the Dirac point (a) Gap size as a function of lattice distortions (b) Band structures of distorted lattice with a band gap at the Dirac point ($r=80\text{nm}$, $h=160\text{nm}$ with a Drude model approximation for silver dielectric constants)

the patterns, followed by development of the exposed areas. Double layer resists enable formation nice edge cut between the two layers. Finally, we utilize electron beam evaporation to deposit 4 nm of Ge as the adhesive layer and 160nm of silver. Resists are lifted off in hot solvents (remover PG). Figure 4.7a is an SEM image of the top view of the fabricated honeycomb lattices, and Figure 4.7b is an SEM image of the side view of the fabricated structure using this technique. The nanopillars are cone-like with some height variation looking from the side, due to limitation of the fabrication method.

4.5 Cathodoluminescence characterization of Dirac-like plasmons

In order to characterize bandstructures of nanopillars as well as edge states, we need a technique that could excite the TM mode at different wave vectors, as well as the ability to excite a single particle on the edge. Angle resolved cathodoluminescence spectroscopy is particularly suited for this type of measurement. For cathodoluminescence, electron beams incident on the sample, form image charge and therefore excite the sample with dipole moment. Dipoles are capable of exciting modes with a wide range of wave vectors. After the excitation, the emitted light from the sample are collected by a parabolic mirror and spectrally analyzed by a spectrometer to differentiated the spectrum. With the electron beam we could also have very good control of spatial excitation position. We have performed initial Cathodolumines-

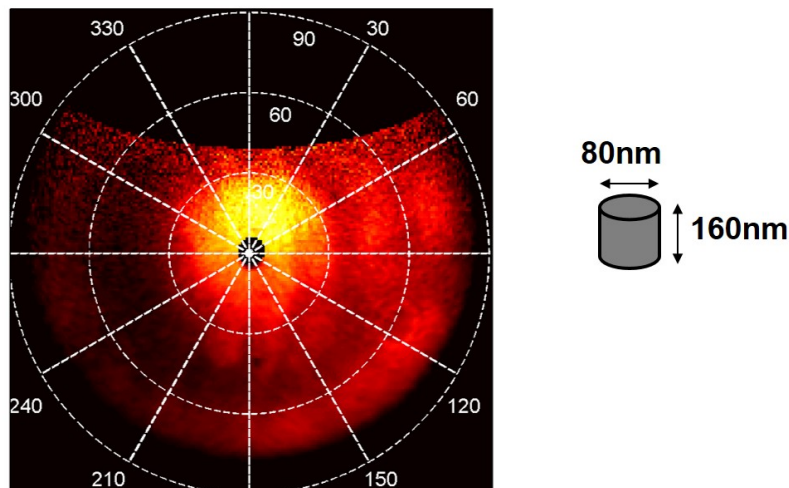


Figure 4.8: Angle resolved cathodoluminescence of a single silver pillar at 650nm

cence spectroscopy on single nanopillar, dimers, and infinite honeycomb lattices. For a single nanopillar, CL confirm very strong dipole emission shown in Figure 4.8. Instead of isotropic emission pattern, we observe bright emission on one side as a result of the tilted nanopillars due to fabrication imperfection. Comparing the dimer emission pattern shown in Figure 4.9 to that of a monomer, we observe a change of emission direction which is not related to the direction of the nanopillar tilt. Also, by switching to an opposite excitation point, the emission pattern is rotated by 180 degrees. The results confirms coupling between the two nanopillars. Looking at the emission pattern of infinite honeycomb lattice shown in Figure 4.10, we see bright emission spots on the edge of the Brillouin zone, which is what we expect from an integrated spectrum at energies close to the Dirac point. At lower wavelength, the spots merges and moves closer to the center of the Brillouin zone, which is also expected. Fabrication imperfections such as tilt and uneven height caused the emission to be anisotropic from the monomer, and the emission from the honeycomb lattices to to not six-fold symmetric. Going forward, fabrication needs to be improved in order to measure cleaner signals from the lattice.

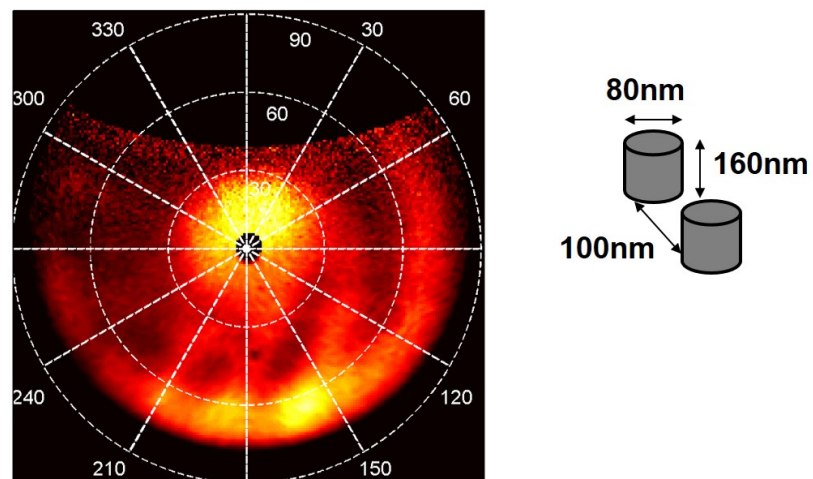


Figure 4.9: Angle resolved cathodoluminescence of a dimer pair of silver pillars at 650nm

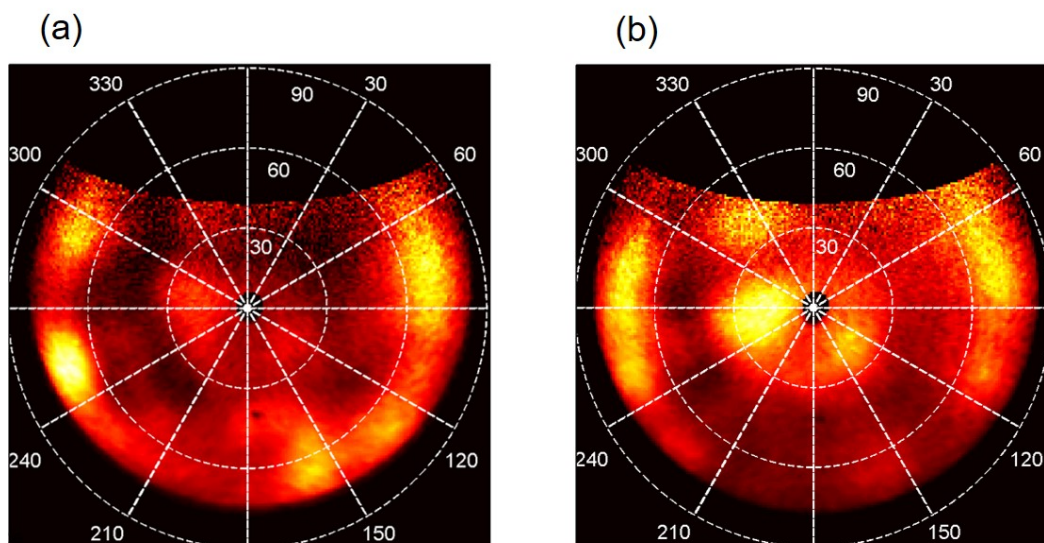


Figure 4.10: Angle resolved cathodoluminescence of silver pillars in honeycomb lattices at (a) 800nm (b) 750nm

MIE RESONATORS: RESONANCES AND COUPLINGS

High index dielectric Mie resonators enable resonant coupling of light into nanoscale volume with low loss. By tuning wavelength of photons and geometries of the resonator, electric and magnetic resonances can be selectively excited. We investigate coupling between dielectric Mie resonators arranged in dimers, hexamers and honeycomb lattices at optical frequencies. Utilizing cathodoluminescence microscopy, we directly visualize redistribution of optical modes resulting from hybridization between resonances from single resonators. Coupling is further supported by evidences from spectral characterization. By studying resonator spectra as a function of inter-resonator distance, we observe coupling strength change as a function of resonator distance. The effect of coupling between dielectric resonators enables more complex devices to achieve novel applications such as optical isolators and sensors.

5.1 Introduction

Coupled oscillators is a simple yet elegant model to describe many phenomenon in nature, such as vibrational motions of chemical bonds in molecules and solids. Energy is transferred through coupling, such as sound waves in atomic resonators and electromagnetic waves in LC resonators. Similarly, optical energy can be transferred through coupling of electromagnetic waves. High index dielectric Mie resonators can resonantly couple to light and confine optical energy with low loss[41, 42, 43, 44]. Through electron beam lithography, geometrical arrangement and distances between the Mie resonators can be precisely controlled. Therefore, Mie resonators provides a perfect platform to systematically study coupling through all degrees of freedom of coupled resonators.

Previously, work has been done to investigate coupling between silicon cylinder and rectangular dimers on SOI wafer [45]. In this work, we investigate resonances of dielectric Mie resonators in dimer pairs, hexamers as well as honeycomb lattices. The Mie resonators are placed on 10nm free standing Si_3N_4 membranes. Compared to Mie resonators on bulk materials, 10nm Si_3N_4 membranes minimize charging effect and interference of cathodoluminescence from the substrate. We report direct observation of coupling between dimers and hexamers as well as honeycomb lat-

tice, by visualizing spatial electric field distribution through cathodoluminescence microscopy[46]. We observe coupling strength varies as a function of distance between the dielectric resonators, as well as geometrical arrangements.

5.2 Sample Fabrication

Mie resonators were fabricated on 10nm thick free standing Si_3N_4 membranes. The fabrication procedures are illustrated in Figure 5.1. We start by lifting off a single crystalline silicon film from an SOI wafer in HF solutions. The SOI wafer was first cleaning by sonication in IPA and acetone solutions, then cleaned with Nanostrip solutions, before being placed in HF solution for overnight liftoff. After the SiO_2 layer were etched away, the silicon film floats on top of the HF solution. We then transfer the silicon film from HF to water with a spoon. The floating silicon film was then placed onto the Si_3N_4 membrane in solution and left dry overnight on a hotplate. After drying, the substrate was cleaned again in nanostrip solution for a second time, followed by electron beam resist (ZEP520) spinning. The electron beam resist, ZEP520, was diluted by anisole solution by a volume ratio of 1:3. Diluted ZEP520 solution forms a thinner film when spinning, therefore has better spatial resolution and mechanical strength. Electron beam lithography was used to lithographically define the pattern, and the pattern was formed by developing away the written part in ZED solution. The remaining electron beam resist form an etch mask, which was treated by electron beam overnight at 2kV. Electron beam curing at 2kV and highest current significantly improves cross linking of the electron beam resist pattern, especially on the edge. Then the pattern was etched into the silicon layer using PBosch reactive ion etching. The remaining etch mask was removed by O_2 plasma cleaning.

5.3 Resonances and coupling of Mie resonators with aspect ratio=1

We start by simulating an isolated single silicon cylinder with radius of 65nm and height of 130nm with full wave time domain method using a TFSSF source and monitors. We observe two distinct resonant features at 596nm and 494nm in the scattering spectrum, shown in Fig 5.2a. To determine the nature of the resonance, we examine electric field distributions, shown in Figure 5.2b, c for the 494nm resonance and Figure 5.2d, e for the 596 nm resonance. The field line in Figure 5.2c, which is the cross section of the cylinder in the xz plane, indicates the resonance at 494nm is an electric dipole resonance. In Figure 5.2e, the electric field lines at 596nm form current loops which indicate a magnetic resonance . To investigate coupling,

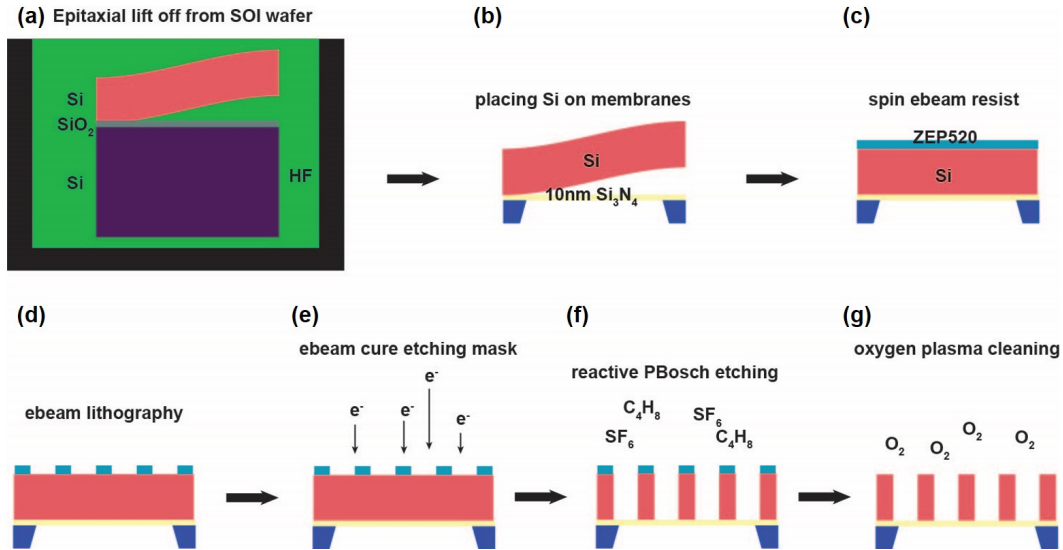


Figure 5.1: Fabrication of Mie resonators on 10nm free-standing Si_3N_4 membranes: (a) Epitaxial lift off of a single crystalline silicon film from an SOI wafer (b) Placement of the silicon film on a 10nm free-standing Si_3N_4 membrane (c) Spin a layer of ZEP520 on the silicon film (d) Electron beam lithography on the ZEP520 film (e) Electron beam curing of the ZEP520 film as an etching mask (f) Reactive ion beam etching of the silicon film (g) Oxygen plasma cleaning to remove ZEP520

we simulate a cylinder dimer pair at a 40nm edge to edge distance using the same method. The simulated spectrum of the dimer pair is shown in Figure 5.3a. We observe shift of both resonances from the single cylinder, the magnetic resonance has redshifted from 596nm to 616nm, and the electric resonance has blue shifted from 494nm to 484nm. The electric field intensity distribution of the dimers at 484nm is shown in Figure 5.3b, c. Comparing Figure 5.3b and Figure 5.2b (top surface of dimers), we observe the field lines from resonators “repel” each other due to coupling. Figure 5.3c supports the observation. The electric field distribution at 616nm along with the field lines are shown in Figure 5.3e and f. We observe one current loop passing through both of the dimers as a clear evidence of coupling versus the single particle case. To further investigate how coupling is affected by distance between the dimers, we simulate dimers with edge to edge distances at 10nm (lightest blue), 15nm (light blue), 20nm (blue), and 40nm (dark blue), shown in Figure 5.3d. The resonance peaks shift further apart as dimer distance decreases, indicate stronger coupling. Experimental evidences of dimer coupling are shown in Figure 5.4. We compare spatial and spectral CL characterization of dimer pairs with a single cylinder resonances. Similar to simulation in Figure 5.3,

we study resonances of dimers pairs with edge to edge distance of 40nm, 20nm, 15nm and 10nm, in Figure 5.4b-e respectively. In the left column, the resonators are excited by electron beam at the center while in the middle column the resonators are excited on the side. Comparing with a single silicon cylinder with a lowest order resonance peak at 571nm indicated by the dashed line in Figure 5.4a, we observe one resonance red shifted at 689nm and another blue shifted to 501nm for the dimer pair with 10nm edge to edge distance in Figure 5.4e. As the distance between dimers decreases, the coupling strength (shift of resonances) weakens which in agreement with simulation results in Figure 5.3. The trend of resonances separation can be visualized in Figure 5.3b-e. For a dimer pair 15nm apart, the resonances are located at 500nm and 643nm (Figure 5.4d). For a dimer pair 20nm apart, the resonances are located at 496nm and 622nm (Figure 5.4c). For a dimer pair 40nm apart, the resonances are located at 571 with a broadened full width half maximum (Figure 5.4b). The selection of electric field distributions on the right column corresponds to the lowest order resonance of each resonator configuration. It is clearly visible that the electric fields from each resonators are “repelled” for all of the dimer configurations. In Figure 5.5a-c, we experimentally compare resonances of a single cylinder, a cylinder dimer with 10nm edge to edge distance and connected dimers respectively. While the resonances of coupled dimers are blue and red shifted due to mode hybridization, new lower order modes emerge at 559nm, 611nm as well as 730nm for the connected dimers. It is evident that while hybridization of modes is still present in the connected dimers, the picture of coupled resonators can no longer be fully applied.

5.4 Resonances and coupling of Mie resonators with aspect ratio=0.65

Another type of resonators we studied are hexagons with $r=100\text{nm}$ and $h=130\text{nm}$. With a lower aspect ratio, electrical and magnetic resonances are less separated. Comparing two types of resonators with difference aspect ratios will give us more insights into how each resonances affect the coupling. The single particle spectrum and electric field distribution are shown in Figure 5.6a-g. The cylinder is excited at the center and on the side, shown in Figure 5.6a and b respectively. Figure 5.6c-g are electric field distribution at each of the resonance peaks in the spectra, at 422nm, 483nm, 568nm (vertical electric dipole resonance), 624nm (magnetic dipole resonance), and 688 nm (electric dipole resonance). Characterization of dimers is shown in Figure 5.7b-h. We observing the vertical electric dipole resonance at 568nm have split into two resonances at 558nm and 581nm, comparing Figure 5.7b

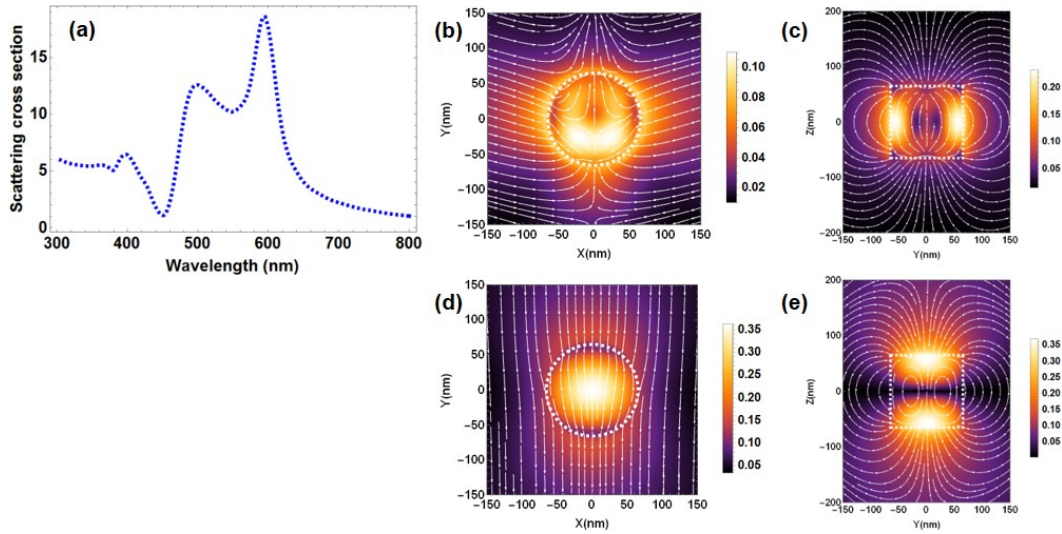


Figure 5.2: Single Mie resonator: (a) Scattering cross section of a single silicon Mie resonator with radius of 65nm and height of 130nm (b) Electric field intensity distribution of the top XY plane at 494nm (c) Electric field intensity distribution of the center XZ plane at 494nm (d) Electric field intensity distribution of the top XY plane at 596nm (e) Electric field intensity distribution of the center XZ plane at 596nm

(dimer edge to edge distance at 35nm) with a single particle spectrum in Figure 5.7 a dimer particle spectrum at a distance of 35nm. This observation is confirmed by electric field distributions in Figure 5.7e at 558nm and Figure 5.7f at 581nm showing binding and anti-binding behavior. We did not observe any coupling for the higher order modes at 423nm and 483nm due to their spatial confinement.

5.5 Asymmetric dimers

The third type of dimers we investigated are asymmetric dimers, composed of one cylinder with $r=65\text{nm}$ and $h=130\text{nm}$ and one hexagon with $r=100\text{nm}$ and $h=130\text{nm}$. Characterization of the asymmetric dimers with edge to edge distance of 40nm and 200nm are shown in Figure 5.8b,e and Figure 5.8c,f respectively. Comparing Figure 5.8b, c with a, which are all spectrum from the hexagon, the vertical dipole resonance split for the 40nm edge to edge distance dimers and broadening of the spectrum for the 200nm edge to edge distance dimers. For spectrum from the cylinder in the asymmetric dimers, we observe red shifts in both Figure 5.8e and f compared to d.

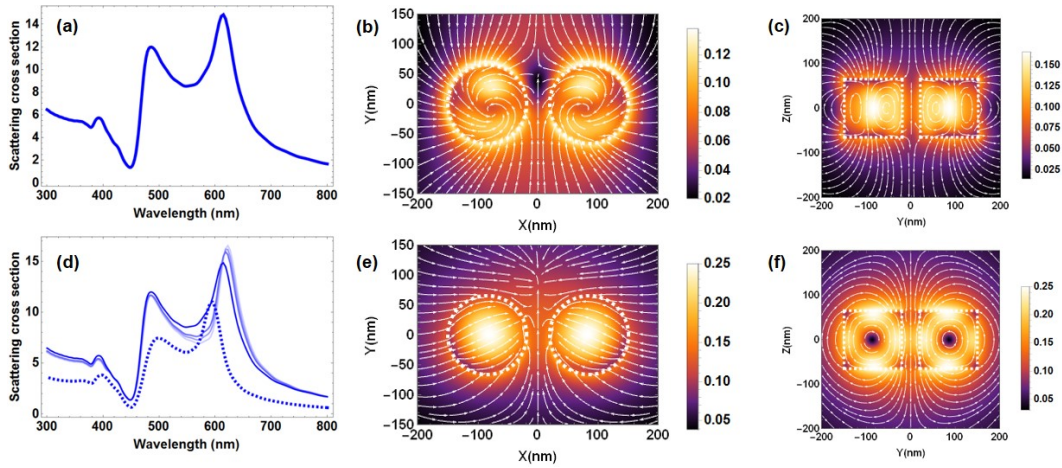


Figure 5.3: Coupled Mie resonators (a) Scattering cross section of dimer silicon Mie resonators with radius of 65nm and height of 130nm and distance of 40nm from edge to edge (b) Electric field intensity distribution of the top XY plane at 484nm (c) Electric field intensity distribution of the center XZ plane at 484nm (d) Scattering cross section of : a single silicon Mie resonator with radius of 65nm and height of 130nm (dashed blue); dimer silicon Mie resonators at distance of 10nm apart (lightest blue); dimer silicon Mie resonators at distance of 15nm apart (second lightest blue); dimer silicon Mie resonators at distance of 20nm apart (third lightest blue); dimer silicon Mie resonators at distance of 40nm apart (fourth lightest blue) (e) Electric field intensity distribution of the top XY plane at 616nm (f) Electric field intensity distribution of the center XZ plane at 616nm

5.6 Coupling of hexamers and honeycomb lattices

The last case we investigated are cylinders and hexagons arranged in hexamers and honeycomb lattices, which have six fold symmetry, shown in Figure 5.9. Figure 5.9e-g are the electric field distributions of hexagons arranged in hexamers. We observe binding modes in Figure 5.9f 664nm where modes are avoided in between the particles, and anti-binding modes at in Figure 5.9g at 750nm, where modes are most intense in between the particles. Figure 5.9a-c are the field distribution of hexagons arranged in honeycomb lattices, with number of periods >10 in both directions. Similarly, we observe anti-binding modes at 664nm and binding modes at 750nm with sharper electric field distributions. More interestingly, in the honeycomb lattice arrangement, at 426nm we observe electric field intensity in the center of the lattice where there is only a 10nm Si₃N₄ membrane, which is not observed for the hexamer arrangement. For cylinders arranged in hexamers and honeycomb lattices shown in Figure 5.9i-p, we did not observe modal distribution off silicon resonators. Due to limitations of fabrication and spatial resolution of characterization, we did not

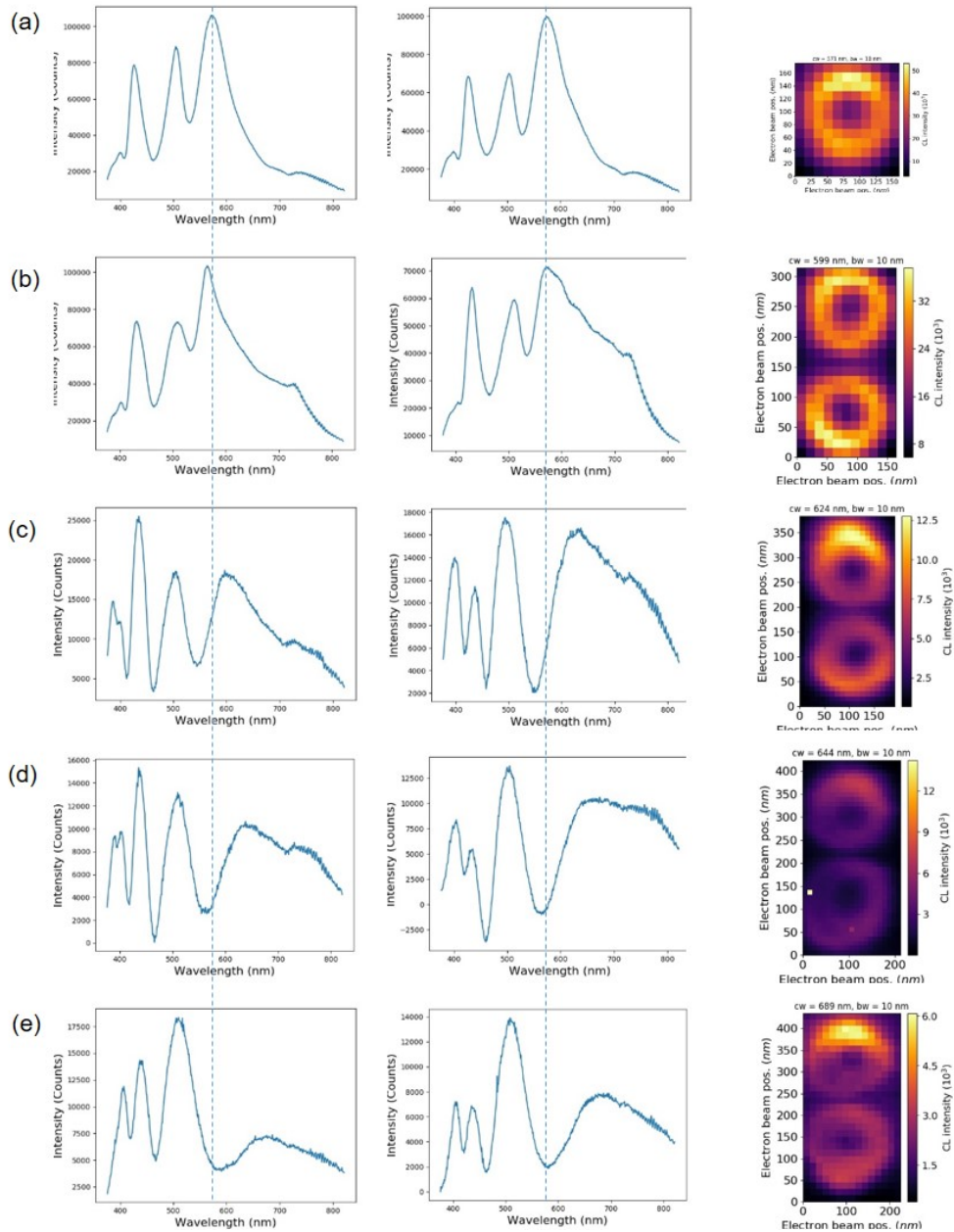


Figure 5.4: Cathodoluminescence characterization of coupled Mie resonators (a) CL spectrum of a single particle of radius 65nm and height 130nm at the center (left), side (middle), CL map at 571nm (right) (b) Dimers of 40nm apart: CL spectrum at the center (left), side (middle), CL map at 599nm (right) (c) Dimers of 20nm apart: CL spectrum at the center (left), side (middle), CL map at 624nm (right) (d) Dimers of 15nm apart: CL spectrum at the center (left), side (middle), CL map at 644nm (right) (e) Dimers of 10nm apart: CL spectrum at the center (left), side (middle), CL map at 689nm

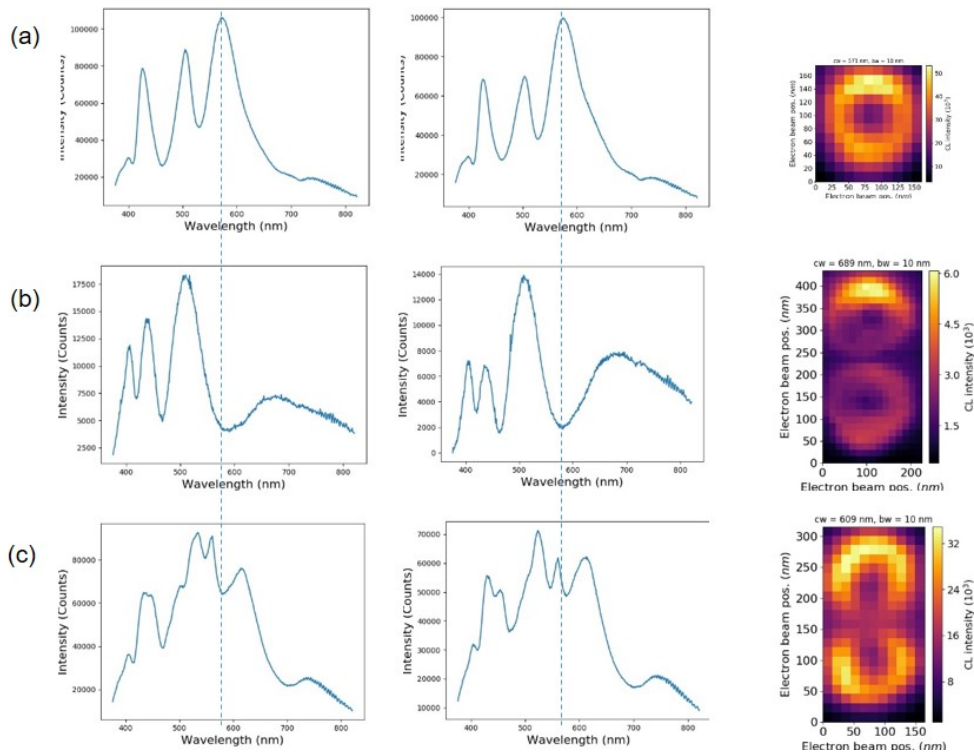


Figure 5.5: Connected Mie resonators: (a) CL spectrum of a single particle of radius 65nm and height 130nm at the center (left), side (middle), CL map at 571nm (right) (b) Dimers of 10nm apart: CL spectrum at the center (left), side (middle), CL map at 689nm (b) Connected dimers: CL spectrum at the center (left), side (middle), CL map at 609nm

observe clear evidence of binding and anti-binding modes.

5.7 Conclusions and outlook

From the results presented here, it is evident that we have observed coupling between individual silicon resonators, from both spectral spatial characterization, in both cylinder and hexagon resonators. For future work utilizing coupling of modes, efforts will be directed toward designing photonic band structures and devices which enable efficient energy transfer with suppressed back scattering.

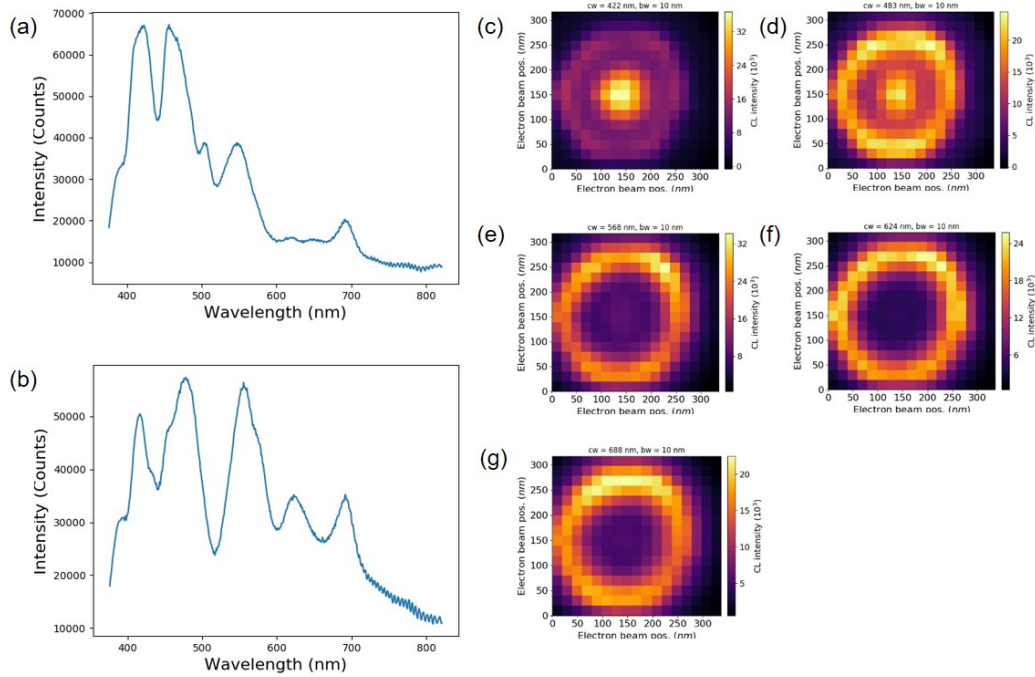


Figure 5.6: Single Mie resonator: (a) CL spectrum of a single particle of radius 100nm and height 130nm at the center (b) CL spectrum of a single particle of radius 100nm and height 130nm at the side (c) CL intensity map at 422nm (d) CL intensity map at 483nm (e) CL intensity map at 568nm (f) CL intensity map at 624nm (g) CL intensity map 688nm

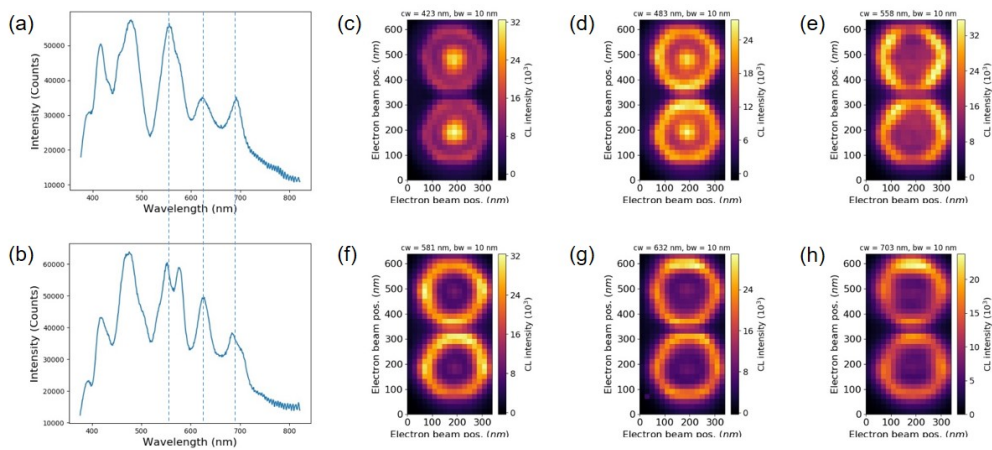


Figure 5.7: Coupled Mie resonators: (a) CL spectrum of a single particle of radius 100nm and height 130nm at the side (b) CL spectrum of dimer particles on the side (c) CL intensity map at 423nm (d) CL intensity map at 483nm (e) CL intensity map at 558nm (f) CL intensity map at 581nm (g) CL intensity map 632nm (g) CL intensity map 703nm

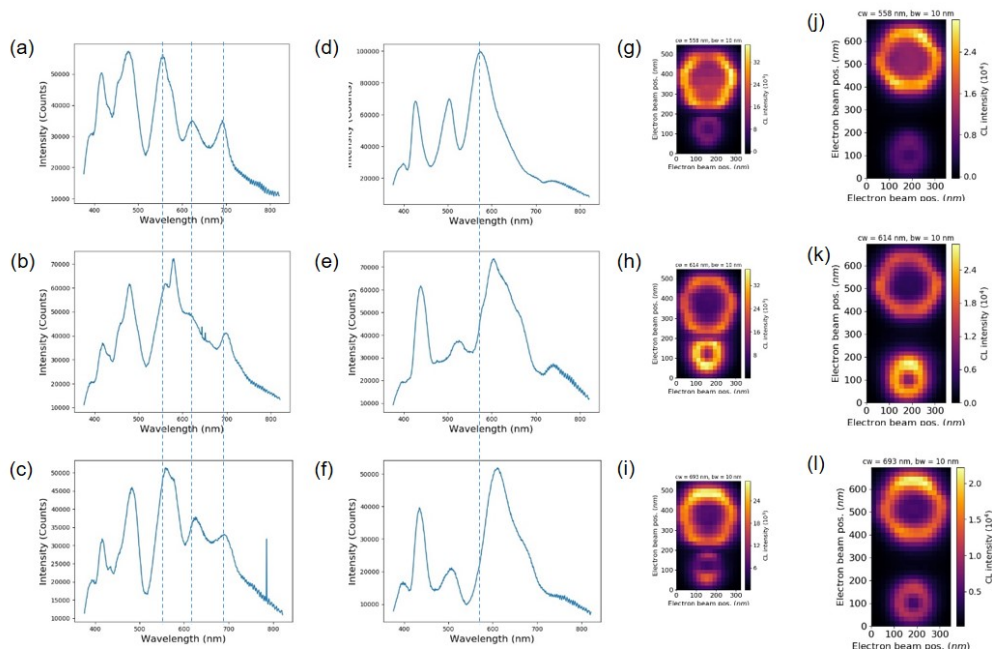


Figure 5.8: Asymmetric dimers: (a) CL spectrum of a single particle of radius 100nm and height 130nm on the side (b) CL spectrum of a asymmetric dimer 40nm apart ($r_1=100\text{nm}$, $r_2=65\text{nm}$), excitation point on the side of the $r_1=100\text{nm}$ particle (c) CL spectrum of a asymmetric dimer 200nm apart ($r_1=100\text{nm}$, $r_2=65\text{nm}$), excitation point on the side of the $r_1=100\text{nm}$ particle (d) CL spectrum of a single particle of radius 65nm and height 130nm on the side (e) CL spectrum of a asymmetric dimer 40nm apart ($r_1=100\text{nm}$, $r_2=65\text{nm}$), excitation point on the side of the $r_1=65\text{nm}$ particle (f) CL spectrum of a asymmetric dimer 200nm apart ($r_1=100\text{nm}$, $r_2=65\text{nm}$), excitation point on the side of the $r_1=65\text{nm}$ particle (g) CL intensity map at 558nm of the 40nm apart dimer (h) CL intensity map at 614nm of the 40nm apart dimer (i) CL intensity map at 694nm of the 40nm apart dimer (j) CL intensity map 558nm of the 200nm apart dimer (k) CL intensity map 694nm of the 200nm apart dimer (l) CL intensity map 693nm of the 200nm apart dimer

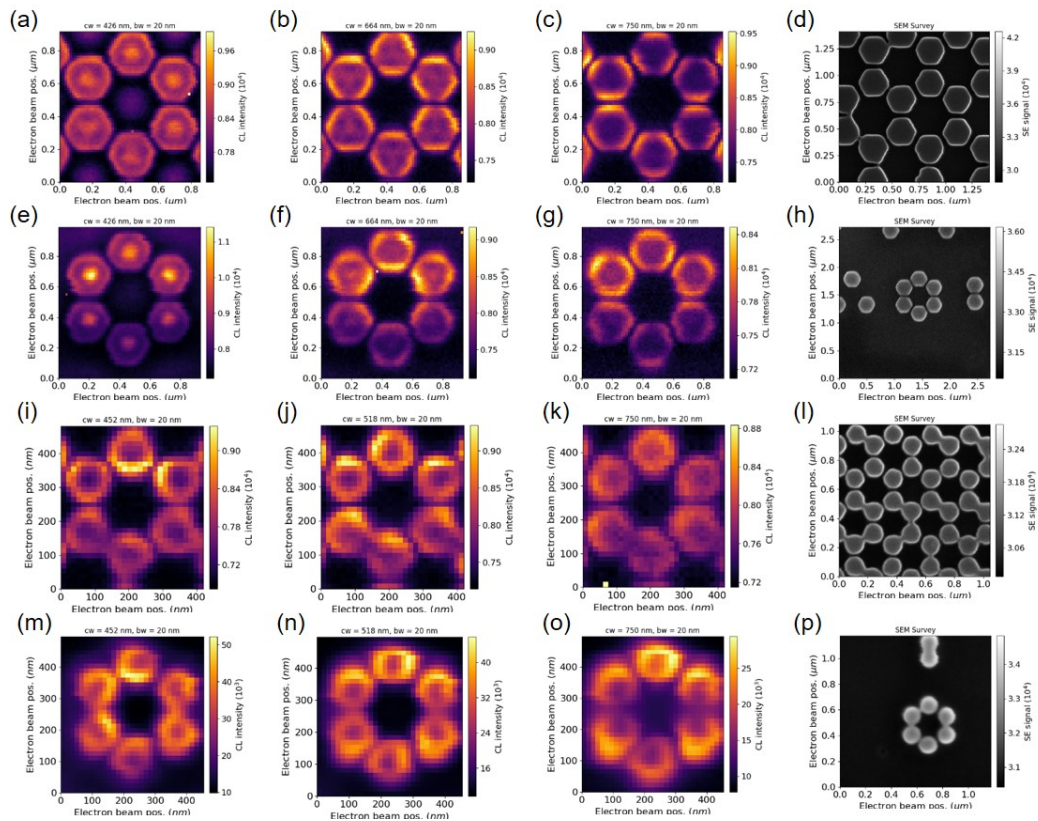


Figure 5.9: Hexamers and honeycomb lattice modes: (a) Lattice I at 426nm, modes in the center (b) Lattice L at 664 nm, anti-bonding mode (c) Lattice L at 750 nm, bonding mode (d) SEM image of lattice I (e) Hexamer I at 426 nm (f) Hexamer I at 664 nm (g) Hexamer I at 750 nm (h) SEM image of hexamer I (i) Lattice s at 452 nm (j) Lattice s at 518 nm (k) Lattice s at 750 nm (l) SEM image of lattice s (m) Hexamer s at 452 nm (n) Hexamer s at 518 nm (o) Hexamer s at 750nm (p) SEM image of hexamer s

MIE RESONATORS IN HONEYCOMB LATTICES: DIRAC-LIKE DISPERSIONS AND TOPOLOGICAL EDGESTATES

Nanoscale architecture of dielectric Mie resonators provide new ways to control directional photon propagation by selective excitation of photonic edge states without backscattering. Dielectric Mie resonators in honeycomb lattices exhibit Dirac-like band structures, similar to the electronic band structure of graphene. Full wave simulations for an infinite honeycomb lattice of dielectric Mie resonators reveal hybridization of localized Mie modes between two neighboring pillars and the consequent formation of bonding and anti-bonding modes that are energetically degenerate at Dirac points. Simulations also reveal that distortion of the honeycomb lattice that reserves the C_6 symmetry opens a photonic bandgap, whose width is proportional to the extent of distortion. Further, electromagnetic simulations reveal the existence of topologically protected edge states in finite width nanoribbons of the distorted lattice at the zigzag and arm-chaired edges. Experimentally, we utilize cathodoluminescence (CL) spectroscopy to study angular emission patterns at optical frequencies and construct band structures with high spectral resolution. Angle resolved characterization yields direct comparison with photonic band structure simulation in the Brillouin zone of a periodic lattice. Angular emission reveals three-fold and six-fold symmetry depending on lattice type, wavelengths, and excitation position. Efforts to construct photonic band structures and investigation of edge states will be discussed.

6.1 Introduction

Topological photonics use unconventional states of light to carry information for communication and computing purposes[5, 4, 47]. Topological phases of light supported by well-designed nanostructures have the unique property to suppress backscattering induced by impurities and bending therefore hold great promise for lossless photon transport for large-scale optical integrated circuits, as well as for quantum computing applications that require insensitivity to environmental noise. However, topological properties of light are widely studied at microwave frequencies due to limitation of fabrication and characterization techniques[6, 48]. Topological photonics realized at near infrared and visible wavelength utilize optical elements

at >micron scale which are not compatible with chip-scale integration[9, 8, 10]. In this work, we report experimental attempts to observe topologically protected edge states in the visible wavelength, on a platform of two dimensional nanometer scale dielectric Mie resonators. Based on theoretical design[12], we fabricated derivatives of honeycomb lattices composed of silicon on top of 10nm thick Si_3N_4 membranes. We utilize cathodoluminescence microscopy which directly image photonic band structures of 2D Mie resonator arrays. Our device, which is composed of silicon and magnetic field-less, is potentially CMOS compatible.

6.2 Dirac-like bandstructures of honeycomb lattice and edge states

A honeycomb lattice consists of two triangular Bravais lattices with lattice constants R_1 . Therefore, one unit cell within a honeycomb lattice consists of two lattice sites, the unit cell marked by the dashed line with diamond shape and lattices site represented as red and blue dots shown in Figure 6.1a. Brillouin zone of a honeycomb lattice is hexagonal, shown by the dashed line in Figure 6.1b, where the high symmetry points are Γ , M and K. The unique geometry of the lattice give rise to the photonic band structures in Figure 6.1c, with a Dirac point at the K point at normalized frequency of 0.24, as a result of nearest neighbor hopping. Alternatively, the honeycomb lattice can be viewed as equivalence of a triangular lattice consists of supercells of hexamers. In this scenario, the super unit cell is illustrated in Figure 6.1a as the dashed hexagon, with lattice constants R_2 . Consequently, the Brillouin zone is folded for the supercell lattice. The reduced Brillouin zone is illustrated in Figure 6.1b as the smaller solid line hexagon, with symmetry points labeled as Γ , M' and K' , where $\Gamma M' = \frac{1}{2} \Gamma K$ and $\Gamma K' = \frac{2}{3} \Gamma M$. In the supercell lattice, Dirac points are folded into the Γ point of the reduced Brillouin zone. By tuning the ratio of R_1 and R_2 of the supercell lattice, a photonic band gap can be opened-close-reopened at the Dirac point from the trivially regime to the topologically regime. Specifically, a trivial gap is opened when $R_1 < \sqrt{3}/3 R_2$, while a topological gap can be opened when $R_1 > \sqrt{3}/3 R_2$. The topologically nature of the gap for $R_1 > \sqrt{3}/3 R_2$ comes from the fact that the upper and lower bands of the Dirac point re-hybridizes from inter-cell lattice site coupling. The photonics bands of the topologically gapped supercell lattice are shown in Figure 6.1d. Within the topological gap, topologically protected edge states exist both along zigzag and arm-chaired edges. As an example, Figure 6.1e is a band structure simulation along the zigzag edge between the topologically gapped lattices and the trivially gapped lattices. Two edge states cross at a normalized frequency of 0.485, each representing a specific

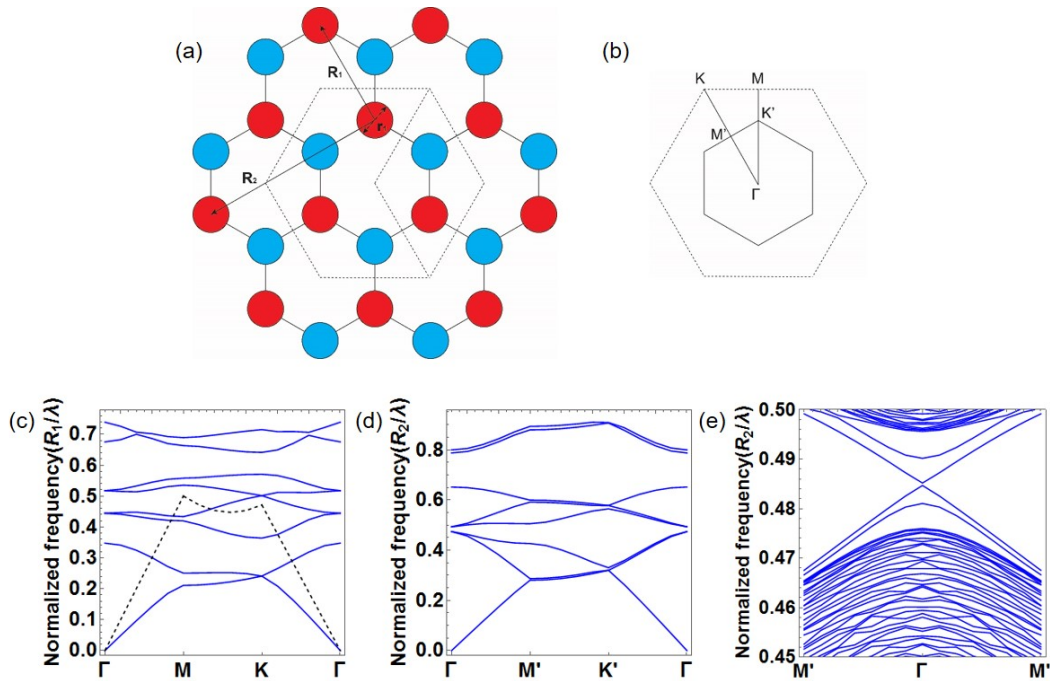


Figure 6.1: (a) Honeycomb lattice with lattice constant R_1 for the smallest unit cell (diamond shaped dashed line), and triangular lattice with lattice constant R_2 with the hexagonal shaped unit cell (dashed cell) (b) First Brillouin zone of the honeycomb lattice (dashed line), reduced Brillouin zone of the supercell triangular lattice (solid line) (c) Band structures of a honeycomb lattice in the first Brillouin zone (d) Band structures of a supercell triangular lattice with a band gap ($R_2=2.9R_1$) (e) Edge states at the Zigzag edge within the bandgap

propagation direction along the zigzag edge. The fact there are no other states to scatter into in the frequency range of 0.48 to 0.49 gives rise to the topological protection.

6.3 Angle-resolved cathodoluminescence characterization of photonic band-structures

Experimentally, we study two types of photonic lattices, lattice consists of Mie resonators with aspect ratio=1 ($r=65\text{nm}$, $h=130\text{nm}$) which we abbreviate as lattice s and lattice consists of Mie resonators with aspect ratio=0.65 ($r=100\text{nm}$, $h=130\text{nm}$) which we abbreviate as lattice l. Cathodoluminescence spectroscopy is used to characterize the photonic band structures. To excite optical modes, the electron beam is incident on the sample, which induces a vertical dipole that preferably excites the TM mode of the photonic lattices. The out-coupled light at different angles is projected by a parabolic mirror onto a CCD camera which is represented

as angle resolved patterns in Figure 6.2 and Figure 6.3. Figure 6.2a-d are the angle resolved patterns from honeycomb lattice I, in comparison to diffraction pattern of free-photon approximations (right panel). The left panel and middle panel of Figure 6.2a-d are angle resolved patterns from excitation position A and B respectively, indicated in Figure 6.2f. A and B are two lattice sites in one unit cell of the honeycomb lattice. We observe that at A, a three-fold symmetric bright band is excited together with a three-symmetric dark band, shown in Figure 6.2a, b, d and e. For excitation point B, the bright and dark bands are reversed, in agreement with the real space lattice symmetry. To be more quantitative, we employ free photon approximation [49, 50, 51, 52, 53, 54] 10, 11, 12, 13, 14, 15 given by

$$\frac{e^{i k R}}{R} \sum_{n=1}^N e^{-i k r_n} \quad (6.1)$$

where R is the radius of the observation sphere and k is the wave vector. Blue lines represent the lower wavelength limit and red lines represent the upper wavelength limit. Boundaries of the angle resolved patterns are well depicted by the free photon approximation. However, the symmetry of bright and dark bands are not explained. In the free photon approximation, it is assumed that each of the lattice sites scatter cylindrical waves and no coupling is present. However, additive rule does not apply for the angle resolved pattern. Namely, the pattern can not be subtractively separated into spherical waves from each scatter. For example in Figure 6.2b, the bright bands does not continue into polar angles $< 20^\circ$, which could not be explained by free photon approximation. From simulations and experiments in chapter 5, we understand that free photon approximation is not an exact depiction of our experimental system. In Figure 6.3, we compare angle resolved patterns of different lattices types. Figure 6.3a,f are angled resolved patterns from honeycomb lattice s and lattice I. Figure 6.3b,g are angle resolved patterns from topologically gapped lattice s and lattice I. Figure 6.3c,h are angle resolved patterns from trivially gapped lattice s and lattice I. Figure 6.3d,i are angle resolved patterns from zigzag edges of lattice s and lattice I. Figure 6.3e,j are angle resolved patterns from arm-chaired edges of lattice s and lattice I. According to the measured orientation of the lattice, the Brillouin zone is indicated in Figure 6.1b as the dashed lines, with K points at polar angle of 41.8° and M points at polar angle of 35.26° . In Figure 6.3b-e, we observe bright spots indicating optical modes at K points and M points. For angle resolved patterns from lattice I, we observe “six-fold stars” with the tip of the stars intersecting K points, shown in Figure 6.3g-j. These angle resolved patterns are integral of the optical modes over a bandwidths of 40nm. Since the photonic

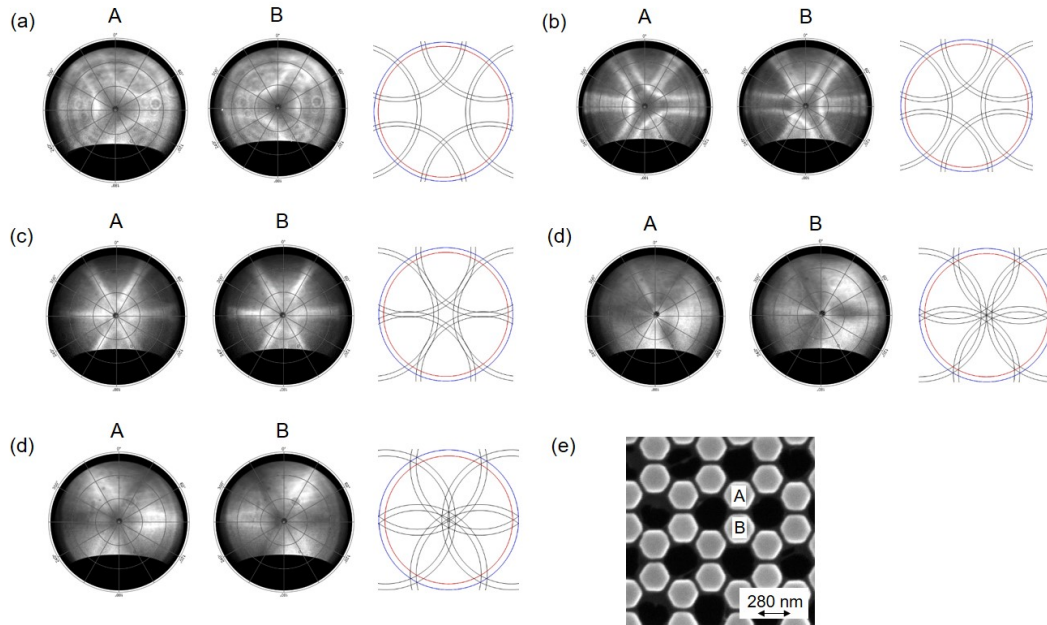


Figure 6.2: Electron beam induced bands asymmetry: (a) 630 – 670 nm (b) 580 – 620 nm (c) 530 – 570 nm (d) 480 – 520 nm (e) 430 -470 nm (d) Lattice orientation and electron beam excitation location

band gap is small (between 20-40nm), in order to resolve edge states, we employ techniques to characterize photonic band structures with better spectral resolution.

6.4 Photonic band structures in the bulk and on the edges

Hyperspectral angle resolved characterization is performed by letting out-coupled light through a narrow slit at a specific symmetry direction. Light is then spectrally resolved with a spectrometer. Fig 6.4 a-e are hyper-spectral angle resolved measurement from topologically gapped lattice s, at 0° , 15° , 30° , 45° , 60° respectively. 0° and 60° corresponds to symmetry direction of Γ -M, and 30° corresponds to symmetry direction of Γ -K. The x-axis of these characterizations are plotted in normalized units of $\frac{k}{k_0}$, while y-axis is wavelength. With the normalized units, $x=0$ corresponds to Γ , $x=0.57735$ corresponds to M and $x=0.66667$ corresponds to K. We observe clear dispersions, for example, from 650nm to 750nm in Figure 6.4e. We performed similar characterization on trivially gapped lattice s, shown in Figure 6.4 f-j. In Figure 6.4i,j, we observe interesting crossing of linear dispersion at 710nm. Characterizations on zigzag and arm-chaired edges are shown in Figure 6.4k-o and p-t respectively. The crossed linear dispersions are also observed in Figure 6.4k, l, m, n, o. Characterizations of honeycomb lattice l are shown in Figure 6.5, over the same set of angles. Characterizations of topologically gapped lattice l, trivially gapped

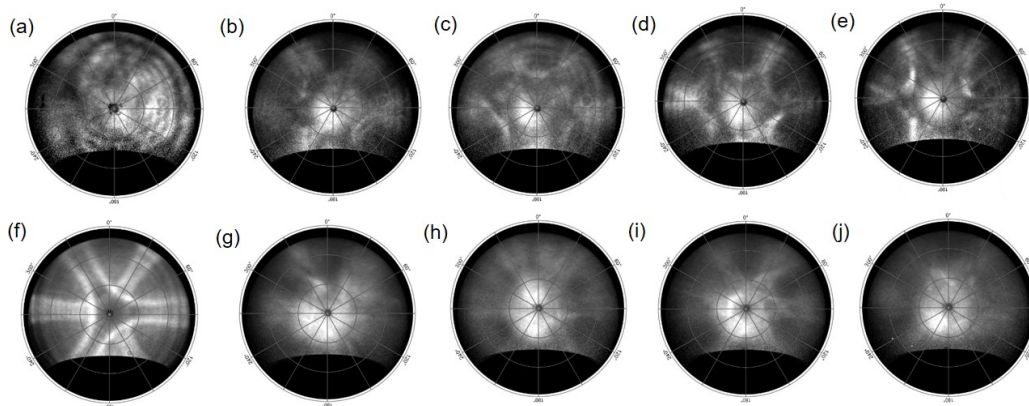


Figure 6.3: Mapping band structures in the Brillouin zone: (a) Honeycomb lattices s 630-670nm; (b) Topologically gapped lattices s 630-670nm; (c) Trivially gapped lattices s 630-670nm; (d) Zigzag edges lattice s 630-670nm; (e) Arm-chaired lattice s 630-670nm; (f) Honeycomb lattices l 580-620nm; (g) Topologically gapped lattices l 580-620nm; (h) Trivially gapped lattices l 580-620nm; (i) Zigzag edges lattices l 580-620nm; (j) Arm-chaired lattices l 580-620nm

lattice l, zigzag edges and arm-chaired edges of lattice l, shown in Figure 6.5a-f, g-l, m-r, and s-x. The set of characterization angles are 0° , 15° , 30° , 37° , 45° , and 60° . Compared with Figure 6.4, we observe additional dispersion features appear in Figure 6.5, for example the triangular-shaped features in Figure 6.5x. Although We observe clear dispersion features, which support existence of lattice mode dispersions, further comparison with band structure simulations is necessary to identify physical meaning of the bands. Ideally, characterization on a photonic crystal lattice with simple dispersion features can be used as a bench mark to verify the validity and consistency of this method.

6.5 Conclusions

In conclusion, we have experimentally investigated dispersion features of honeycomb lattices and gapped honeycomb lattices at visible frequencies. We observe clear three-fold and six-fold symmetric patterns in angle-resolved dispersion features. Hyper-spectral angle resolved characterizations have further confirmed our observation. A complete angle span from hyper-spectral angle resolved measurements enable us to construct 3D photonic band structures. However, to further our understanding of dispersions to distinguish between bulk and edge states, more advanced modelling is necessary. Periodic infinite cylinder mpb simulations and free photon approximations guide us through initial qualitative understanding of the data.

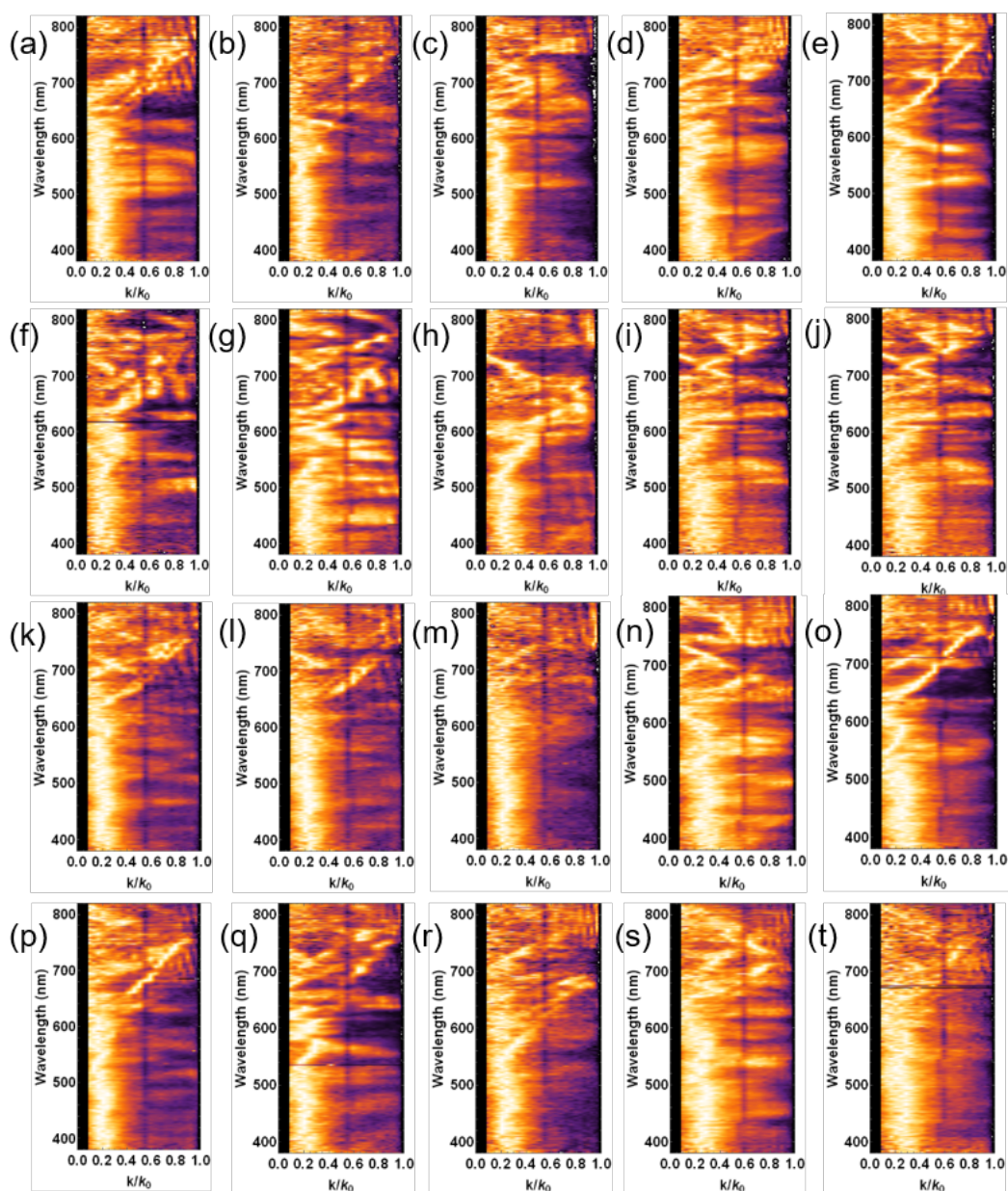


Figure 6.4: Spectral resolved photonic bands lattice s ($r_1=65\text{nm}$, $h=150\text{nm}$, trivial gap: $R_1=246\text{nm}$, $R_2=444\text{nm}$, factor=3.12): (a) 0 degrees topological gap (b) 15 degrees topological gap (c) 30 degrees topological gap (d) 45 degrees topological gap (e) 60 degrees topological gap (f) 0 degrees trivial gap (g) 15 degrees trivial gap (h) 30 degrees trivial gap (i) 45 degrees trivial gap (j) 60 degrees trivial gap (k) 0 degrees Zigzag edge (l) 15 degrees Zigzag edge (m) 30 degrees Zigzag edge (n) 45 degrees Zigzag edge (o) 60 degrees Zigzag edge (p) 0 degrees arm-chaired edge (q) 15 degrees arm-chaired edge (r) 30 degrees arm-chaired edge (s) 45 degrees arm-chaired edge (t) 60 degrees arm-chaired edge

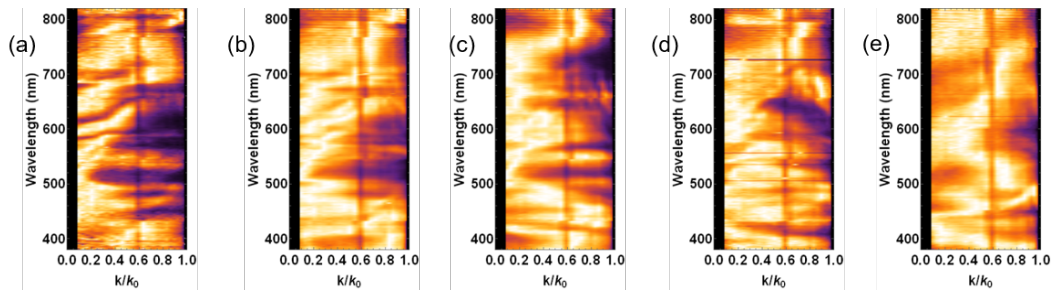


Figure 6.5: Spectral resolved photonic bands honeycomb lattice I: ($r_1=284\text{nm}$, $h=230\text{nm}$, $R_1=526\text{nm}$) (a) 0 degrees honeycomb lattice I (b) 15 degrees honeycomb lattice I (c) 30 degrees honeycomb lattice I (d) 45 degrees honeycomb lattice I (e) 60 degrees honeycomb lattice I

To be more precise, full wave band structure simulations of finite size cylinders are necessary. With better design and modelling, our fabrication and characterization methods are capable of observing topologically protected photon transport at the nanoscale.

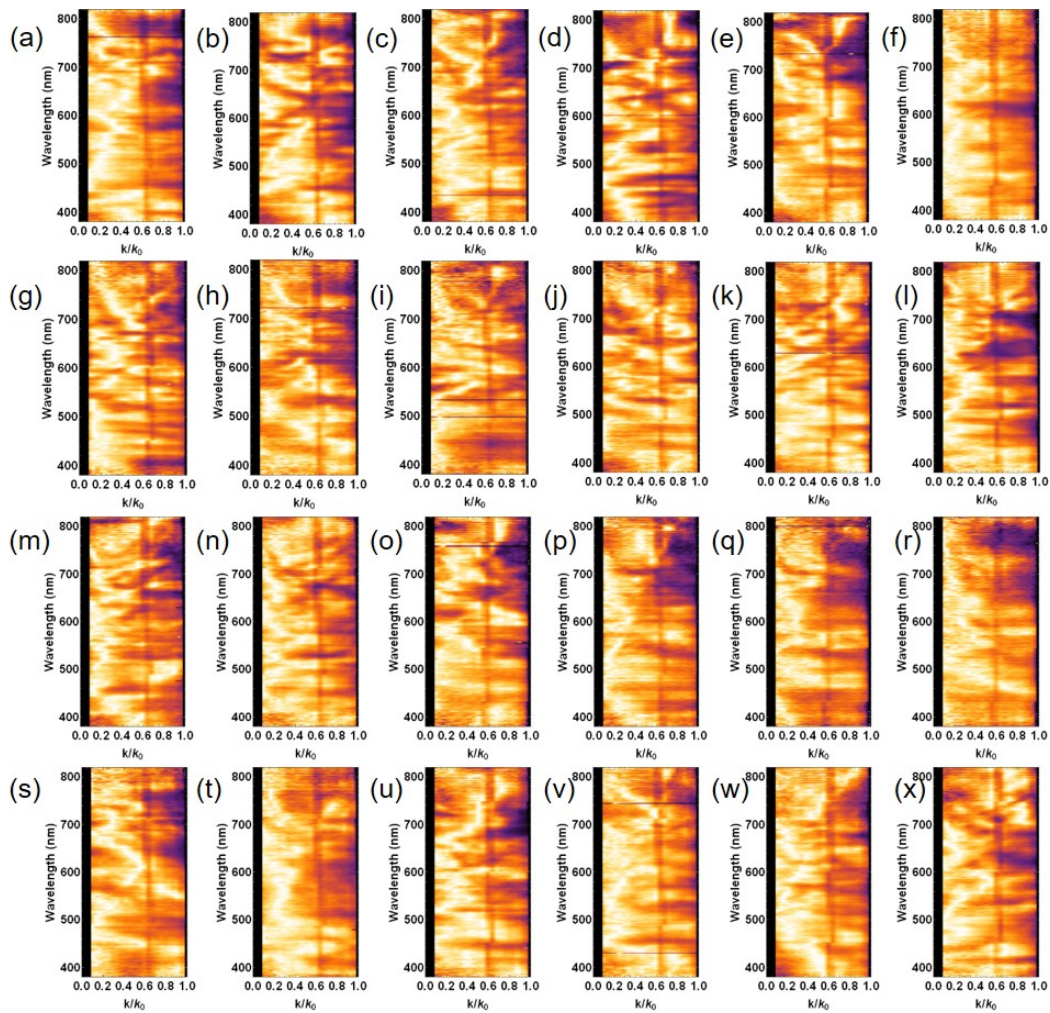


Figure 6.6: Spectral resolved photonic bands honeycomb lattice I: (need information from MP5 on the trivial and topologically gapped lattice) (a) 0 degrees topological gap (b) 15 degrees topological gap (c) 30 degrees topological gap (d) 37 degrees topological gap (e) 45 degrees topological gap (f) 60 degrees topological gap (g) 0 degrees trivial gap (h) 15 degrees trivial gap (i) 30 degrees trivial gap (j) 37 degrees trivial gap (k) 45 degrees trivial gap (l) 60 degrees trivial gap (m) 0 degrees Zigzag edge (n) 15 degrees Zigzag edge (o) 30 degrees Zigzag edge (p) 37 degrees Zigzag edge (q) 45 degrees Zigzag edge (r) 60 degrees Zigzag edge (s) 0 degrees arm-chaired edge (t) 15 degrees arm-chaired edge (u) 30 degrees arm-chaired edge (v) 37 degrees arm-chaired edge (w) 45 degrees arm-chaired edge (x) 60 degrees arm-chaired edge

*Chapter 7***ULTRAVIOLET SURFACE PLASMON-MEDIATED LOW TEMPERATURE HYDRAZINE DECOMPOSITION AND GROWTH OF GAN**

Conventional methods require elevated temperatures in order to dissociate high-energy nitrogen bonds in precursor molecules such as ammonia or hydrazine used for nitride film growth. We report enhanced photodissociation of surface-absorbed hydrazine (N_2H_4) molecules at low temperature by using ultraviolet surface plasmons to concentrate the exciting radiation. Plasmonic nanostructured aluminum substrates were designed to provide resonant near field concentration at $\Lambda = 248$ nm (5 eV), corresponding to the maximum optical cross section for hydrogen abstraction from N_2H_4 . We employed nanoimprint lithography to fabricate 1 mm x 1 mm arrays of the resonant plasmonic structures, and ultraviolet reflectance spectroscopy confirmed resonant extinction at 248 nm. Hydrazine was cryogenically adsorbed to the plasmonic substrate in a low-pressure ambient, and 5 eV surface plasmons were resonantly excited using a pulsed KrF laser. Mass spectrometry was used to characterize the photodissociation products and indicated a 6.2 overall enhancement in photodissociation yield for hydrazine adsorbed on plasmonic substrates compared with control substrates. The ultraviolet surface plasmon enhanced photodissociation demonstrated here may provide a valuable method to generate reactive precursors for deposition of nitride thin film materials at low temperatures.

7.1 Motivation

Gallium nitride (GaN) and indium gallium nitride (InGaN) are tunable wide band gap semiconductor materials with important applications in optoelectronic devices such as LEDs and photovoltaics[55, 56]. Conventional growth methods for these materials include chemical vapor deposition (CVD) and molecular beam epitaxy (MBE), which both require high temperatures (>500 K) to create atomic nitrogen growth species by thermal decomposition of nitride precursor molecules[57]. Alternatively, magnetron sputtering can be used to grow nitride semiconductors at room temperature[58]. However, the sputtering process utilizes high-energy plasma ions to bombard nitride precursors, resulting in a high kinetic energy distribution of atomic nitrogen that limits the crystalline quality of the growing film. By con-

trast, ultraviolet (UV) radiation can resonantly dissociate nitrogen bonds, through a pathway that does not produce species with high kinetic energy or require high temperatures. By generating a kinetic energy distribution of the dissociated nitrogen species similar to that achieved in molecular beam epitaxy or chemical vapor deposition processes, resonant ultraviolet dissociation of nitrogen precursors may enable low temperature film growth with superior crystalline quality. Additionally, because film growth could occur at lower temperatures, such a process may open doors for synthesis of difficult-to-make semiconductor materials such as indium rich InGaN, which is normally hindered due to phase separation into InN and GaN at elevated growth temperatures[59, 60].

We utilize the optical confinement properties of surface plasmons to localize ultraviolet radiation in a surface-adsorbed hydrazine layer and thus generate a high flux of reactive nitrogen species athermally, with the aim of overcoming the limitations of conventional high temperature nitride film growth, a method of nitride precursor generation that has not been demonstrated before. Surface plasmons are coherent oscillations of charge density at the interface of a metal and a dielectric that confine incident radiation within evanescent fields of subwavelength extent in the direction perpendicular to the surface, thereby providing concentration of optical intensity at resonance up to 1000 greater than the free space intensity in some cases[61]. This remarkable property of surface plasmons has been studied extensively for various applications such as surface-enhanced Raman scattering (SERS)[62], surface enhanced photo-chemistry[63, 64, 65, 66, 67, 68, 69], optical tweezing[70], and nanoparticle therapeutics[71]. In our experiment, the enhancement of radiation fields via surface plasmon excitation is employed to maximize resonant ultraviolet decomposition of nitride growth precursor molecules that are cryogenically condensed at high concentration on plasmonically active substrates.

7.2 N-H bond energy of the N_2H_4 molecule

We identify hydrazine (N_2H_4) as a promising nitride growth precursor molecule for low temperature film growth. N_2H_4 molecules have a dissociation threshold at $\Lambda = 376.2$ nm and very large optical absorption cross section at 5 eV ($\Lambda = 248$ nm),[72, 73] which is compatible with an KrF excimer laser excitation at 248 nm. Figure 7.1 shows the potential energy diagram along the N-H bond in a N_2H_4 molecule calculated at the level of GVB-RCI (generalized valence bond - restricted configuration interaction) (restricted double excitation)[74]/cc-pVTZ//B3LYP/6-311++G**. Optical excitation at 5 eV resonantly excites the N-H bond in the singlet electronic

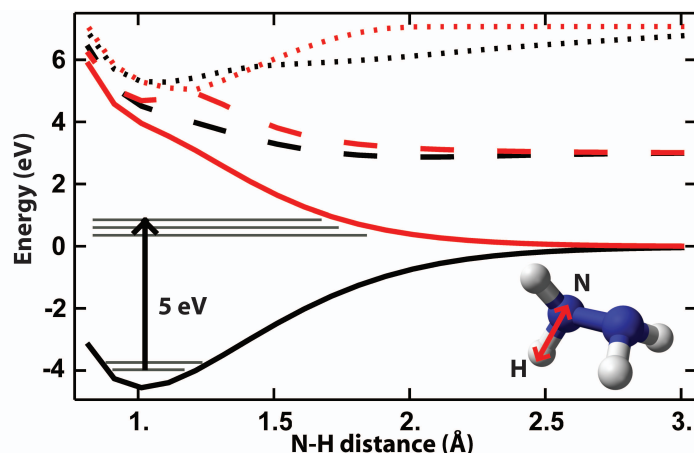


Figure 7.1: N_2H_4 energy curve: Solid black curve (S_0) is the singlet ground state for the N-H bond. Inside the potential well of S_0 , the horizontal lines represent the roto-vibrational states. Optical excitation at 5eV (free space wavelength 248nm) excites the ground state to higher roto-vibrational states and dissociates the N-H bond. The calculated curves depict the triplet first excited state (T_1 , solid red), the singlet first excited state (S_1 , dash black), the triplet second excited state (T_2 , dashed red), the singlet second excited state (S_2 , dotted black), and the triplet third excited state (T_3 , dotted red).

ground state (S_0) which we calculated to have an energy barrier of 4.0 eV after including the zero point energy correction, from a lower roto-vibrational state to a higher roto-vibrational state. The higher roto-vibrational state is sufficiently energetic to overcome the potential well of the S_0 state, resulting in the stretch of the N-H bond and ultimately, bond dissociation, and energizing other degree of freedoms in the molecule with the excess energy from the surface plasmon (1.0 eV in this case). We note that the energy gap between the ground state S_0 and the first excited state T_1 is 8.6 eV, which is too large to be excited by a 5 eV surface plasmon. We utilize surface plasmons to enhance the ultraviolet radiation field that excites the 5 eV dissociation pathway in N_2H_4 . Ultraviolet surface plasmons have been studied in the past to enhance surface photochemical reactions[63], increase sensitivity of SERS[62], and generate photoelectron emission[75]. In the above context, aluminum has been identified as a promising ultraviolet plasmonic material for two reasons: its high bulk plasmon energy in the deep ultraviolet and low optical loss[75, 76, 77] entails that it provides strong ultraviolet field enhancement compared to more conventional plasmonic materials such as gold and silver.

7.3 FDTD simulation of aluminum plasmonic grating

To optimize plasmonic concentration of optical energy at 5 eV and facilitate dissociation of N_2H_4 , we performed full wave electromagnetic simulations of surface plasmon modes in aluminum nanostructures. We identified a periodic aluminum grating structure as a simple and promising geometry, because it enables momentum matching between incident photons and surface plasmon modes on the metal. Shown in Figure 7.2a is the modeled reflectance over energy and wave number $k_g = 2\pi/\text{grating pitch}$, of an aluminum grating where a 4 nm native oxide on the surface (shown in Figure 7.2b) is included in the model. The width of the ridges (W in Figure 7.2b) of the grating increases as the grating pitch increases. Both the photonic dispersion and surface plasmon dispersion are manifested as a valley in reflectance spectrum (blue color in Figure 7.2a), indicated by the dashed lines. At lower wavenumber (larger pitch), the surface plasmon approaches the light line. As the wavenumber increases, the surface plasmon diverges from the light line and approaches an asymptotic limit, indicating localization of the optical field on the surface of the aluminum. In Figure 7.2a, the reflectance valley indicated by the circles arises from the localized surface plasmon mode at the ridges of the grating. Similar to the localized plasmonic mode of a metal nanoparticle, the energy of this localized surface plasmon mode decreases as W increases with the grating pitch. The broader reflectance valley at small wavenumber indicated by the stars corresponds to photonic modes and reveals the diffraction orders of the aluminum grating. We performed a systematic parameter variation changing W, the grating height (H in Figure 7.2b), and pitch of the grating to determine the geometry with minimum reflectance at 248 nm, corresponding to maximum field concentration in the plasmonic mode. We observe the strongest surface plasmon resonance at this wavelength for a grating period of 205 nm, width of 24 nm, and height of 50 nm. The electric field magnitude of the optimal geometry (Figure 7.2b) indicates that the optical energy is clearly confined close to the surface of the metal. By integrating of the electric field magnitude, we observe a near-field enhancement factor of 25x in the optimized design.

7.4 Fabrication of aluminum grating by nanoimprint lithography and UV characterization

A large area aluminum grating structure with the optimized design identified above was fabricated using a nanoimprint lithography process in which electron beam lithography was used to fabricate the nanoimprint stamp[78]. Briefly, electron

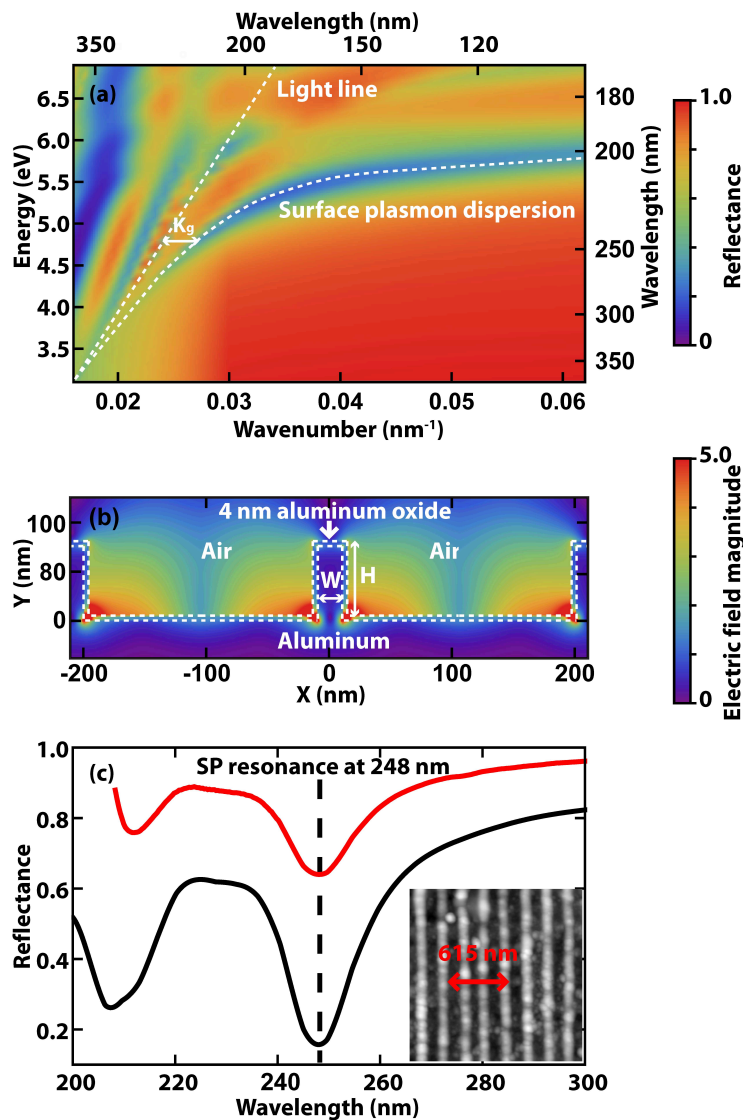


Figure 7.2: (a) Full wave (finite-difference time-domain) simulation of the reflectance versus wavenumber, $k_g = 2\pi/\text{grating pitch}$, and energy of the aluminum grating with 4 nm aluminum oxide on top. The surface plasmon dispersion and the photon dispersion are manifested as the reflectance minimums (dashed white) in the density plot. Localized surface plasmon modes (circles) and photonic modes (stars) are also indicated. (b) The electric field magnitude for two grating periods of the optimized design, with 248 nm incident photons, shows strong field confinement near the surface. The aluminum grating and aluminum oxide layers are marked by white dotted lines. (c) Full wave simulation (FDTD) of the reflectance spectrum at normal incidence is shown (black). The red curve is the experimentally measured reflectance. The dip in reflectance in both the simulated and measured spectra indicates a surface plasmon resonance at 248 nm. Inset: AFM image of the fabricated grating.

beam lithography was used to pattern a silicon wafer coated with negative resist. A grating pattern was etched into the silicon wafer via reactive plasma etching (C_4F_8 and SF_6). The pattern on the silicon wafer was then transferred into a stamp of high modulus polymethyl disiloxane (PDMS). The transferred pattern was stamped into a sol-gel silica film spun onto a sputtered aluminum film via soft contact with the high modulus PDMS stamp. A reactive plasma etch (Cl_2 and HBr) was then performed to transfer patterns from the silica into the aluminum film. An atomic force microscope (AFM) image of the fabricated aluminum grating is shown as the inset of Figure 7.2c. The total area of the patterned structure is 1 mm x 1 mm, and the average period is 205 nm, with an average grating width of 24 nm. We measured the ultraviolet reflectance (Figure 7.2c) of the fabricated aluminum grating using an integrating sphere purged with nitrogen, in order to minimize ultraviolet absorption by atmospheric oxygen. The ultraviolet source of the integrating sphere illuminates the sample at an angle of 8° relative to normal incidence. In experiments that utilize the grating to dissociate N_2H_4 , described below (Figure 7.3), a 248 nm excimer laser excites the grating at normal incidence. However, the surface plasmon resonance of the grating is highly dependent on incident angle, so the measured reflectance spectrum, taken at 8° incidence, has been transformed mathematically to depict the reflectance at normal incidence in order to better compare with experimental conditions. The measured spectrum after this transformation is shown as the red curve in Figure 7.2c. In both the measured and simulated (black) reflectance spectrum, a surface plasmon resonance at 248 nm is clearly visible. The difference in reflectance between the experimentally measured spectrum and the simulated spectrum is attributed to defects in the fabricated aluminum grating.

7.5 Low temperature hydrazine decomposition: experimental set up and characterization

To experimentally characterize the efficiency of the ultraviolet surface plasmon mediated dissociation of N_2H_4 , we utilize mass spectrometry measurements of surface desorbed species, as shown in Figure 7.3. The aluminum plasmonic grating is placed inside a vacuum system at 10^{-6} Torr pressure, mounted on a copper stage that is thermally coupled to a liquid nitrogen bath outside the chamber. When the stage is cooled to 77 K, N_2H_4 vapor is introduced into the vacuum system. The chamber pressure is raised to 10^{-5} Torr by introduction of N_2H_4 , and N_2H_4 molecules are adsorbed on the aluminum grating surface. An unpolarized, pulsed KrF laser operating at 10 Wm^{-2} at 248 nm and 1 Hz pulse rate is directed through

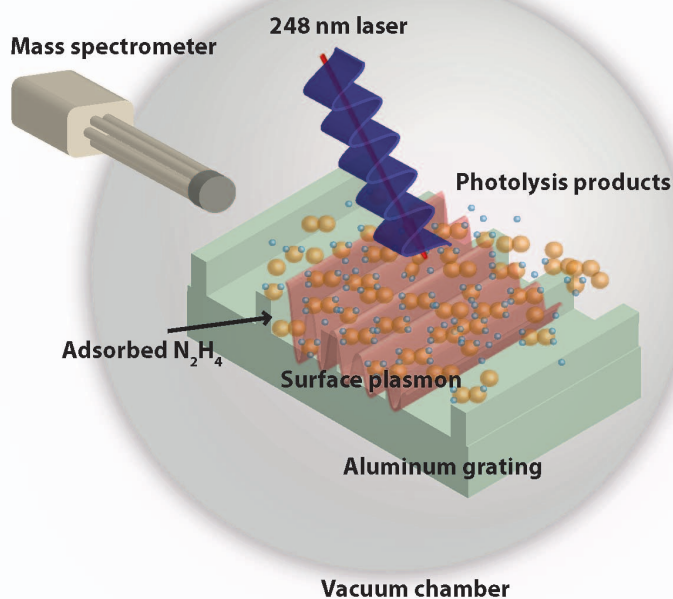


Figure 7.3: Schematic illustration of ultraviolet surface plasmon mediated athermal resonant dissociation of N_2H_4 . A 248 nm laser at normal incidence excites ultraviolet surface plasmons on the surface of a nanostructured Al grating which has been cooled to 77 K inside a low pressure atmosphere of N_2H_4 (105 Torr). The localized optical field resonantly dissociates N_2H_4 molecules adsorbed to the grating surface, and the dissociated species are detected via mass spectrometry.

a viewport into the vacuum chamber at normal incidence on the grating. The plasmonically enhanced optical field resonantly dissociates N_2H_4 molecules into dissociation products such as N_2H_3 . The dissociation products are monitored via mass spectrometry with a filament at an ionization energy of 70 eV. The mass spectrometry data from a typical experiment are shown in Table 7.1. The left column lists the dissociation products of N_2H_4 that are detected by the mass spectrometer. In the middle two columns, we compare the partial pressure and quantum yield of the dissociation products from the aluminum grating substrate and a control substrate consisting of a quartz slide exposed to hydrazine under the same experimental conditions. The signal from each species, Si, in the measured mass spectrum is a convolution of ions generated by resonant ultraviolet dissociation of N_2H_4 , labeled S_{Li} , as well as species that are generated by gas phase N_2H_4 molecules that are dissociated by the mass spectrometer filament directly, labeled S_{Di} . To correct for mass signals that are not due to ultraviolet dissociation of hydrazine, the partial pressure and quantum yield are calculated according to the following procedure.

First, the relative ratio of dissociated species is measured in the dark, defining S_{Di} . The corrected signal, S_{Li} , listed in Table 7.1 is obtained by subtracting the partial pressure of each dissociation product, S_i , from the partial pressure measured in the dark, S_{Di} , normalized for the total amount of N_2H_4 molecules that were ionized and detected

$$S_{Li} = S_i - \frac{S_{Di}}{\sum_i S_{Di}} \sum_i S_i \quad (7.1)$$

We assume that the relative ratio of species generated only by the spectrometer filament, S_{Di} , does not change when the laser is on versus in the dark. Our mathematical procedure ensures that condensed N_2H_4 species on the plasmonic substrate that are released without undergoing ultraviolet dissociation, e.g., from heating or ablation, are not counted in the corrected yield. For each of the dissociated species, the quantum yield, QY_i , is determined from the partial pressure and calculated to be

$$QY_i = \frac{g * S_{Li}}{\text{number of photons}} \quad (7.2)$$

number of photons, where g is a geometric factor relating partial pressure to absolute number of particles based on our chamber configuration. The right column of Table 7.1 shows the enhancement ratio, R_i , of each detected hydrazine decomposition product on the plasmonic substrate as compared with the products from the control substrate. Significantly, the plasmonic substrate enhances the dissociation of every species. The overall enhancement ratio R is calculated by taking the average of all enhancement factors for each dissociation product, where i and j are independent parameters

$$R = \frac{\sum_i R_i \frac{S_{NHi}}{2} + \sum_j R_j S_{N2Hi}}{\sum_i (\frac{S_{NHi}}{2} + S_{N2Hi})} \quad (7.3)$$

The total enhancement factor is 6.2 for all N_2H_4 dissociation products when using the plasmonic aluminum substrate compared with the quartz substrate. In conclusion, we demonstrate a plasmonic nanostructure to concentrate ultraviolet radiation and enhance the generation of reactive nitrogen species athermally via resonant photodissociation by an overall factor of 6.2. Surface plasmon-enhanced athermal dissociation processes, like those demonstrated here, may potentially open alternative pathways for the growth of nitride semiconductor films, by generating reactive nitrogen-containing precursors for film growth at low temperatures.

Dissociated species	Plasmonic substrate		Control substrate		Enhancement ratio, R_i
	Corrected partial pressure (10^{-9} Torr), S_{Li}	Quantum yield (10^{-4}) Q_{Yi}	Corrected partial pressure (10^{-9} Torr)	Quantum yield (10^{-4})	
N	0.3	4	0.008	1	3.6
NH_2	4.5	70	0.1	2	32.6
NH_3	4.1	60	0.2	4	17.6
N_2	3.0	40	1.4	20	2.1
N_2H	4.3	70	0.2	3	20.3
N_2H_3	1.9	30	0.4	6	5.0
Total	18	200	2.4	30	6.2(R)

Table 7.1: The corrected partial pressure and quantum yield of the dissociated N_2H_4 species based on mass spectrometry.

7.6 Experimental set up of ultraviolet plasmon assisted low temperature GaN growth

To enable plasmon resonance-enhanced film growth, we would like to design and develop a bolt-on plasmon resonance-enhanced source for film growth suitable for integration into a vapor deposition chamber for GaN growth, shown in Figure 7.4a. For the plasmon driven nitrogen source, a 248 nm laser excites ultraviolet surface plasmons on the surface of a nanostructured Al grating which has been cooled to 77 K inside a low pressure atmosphere of N_2H_4 (105 Torr). The localized optical field resonantly dissociates N_2H_4 molecules adsorbed to the grating surface, and the dissociated species are detected via mass spectrometry. The low temperature nitrogen source is oriented towards the growth substrate in the main chamber. Atomic gallium source is provided by a gallium gun, also directed at the growth substrate. Layer-by-layer seeding of the growth species is enabled by coordinating modulation of the laser pulse with the shutter of the effusion cell. It is worth noting that this method also enables us to grow AlN, InN as well as $Al_xIn_yGa_zN_{x+y+z}$.//

To start with, We have developed a plasmon resonance-driven film growth process in which the growing film substrate itself (rather than the growth source) is plasmonically active, enabling reactive decomposition of adsorbed species on the growing film surface, shown in Figure 7.4b. In this scheme a migration enhanced epitaxy process for GaN was developed in which first Ga monolayer grows by enhanced migration of Ga on a Ga-terminated surface, followed by adsorption of nitrogen precursors. The decomposition of the nitrogen precursors was enhanced by energy

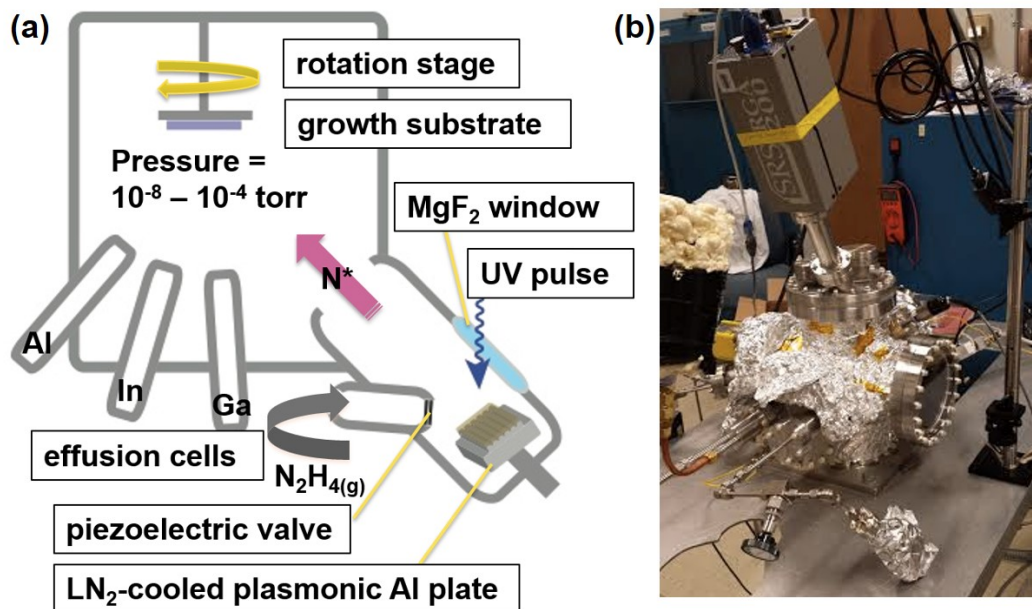


Figure 7.4: GaN growth. (a) A Schematic illustration of a low temperature nitrogen source and epitaxial growth scheme of GaN. (b) View of the actual experimental chamber.

that was coupled into reactive nitrogen species from localized surface plasmons on the thin GaN film growing on an Al coated plastic substrate, while the gallium source is provided by a gallium effusion cell. This is similar to an atomic layer deposition film growth process which utilizes the migration enhanced epitaxy to enhance both precursor decomposition and surface mobility in GaN growth.

7.7 XRD, XPS, EDS, and Raman characterization of GaN film synthesized at low temperature condition

With the growth set up shown in Figure 7.4b, we optimize the growth condition by tuning the relative flux of elemental Ga and plasmonically dissociated hydrazine in our growth chamber for the formation of higher purity GaN films, as well as varying the UV laser repetition rate. The GaN film characterized here is grown at the cryogenic temperature on a gold evaporated silicon wafer, with a laser repetition rate of 1 Hz. The film is prepared by focused ion beam milling and lifted off on to a TEM holder for TEM imaging. A TEM cross sectional image of the film is shown in Figure 7.5a, where the Si/SiO₂/Au/GaN layers are clearly visible. From the TEM image, we determine the thickness of the GaN film to be 30nm. The cross section shown here has indicated that we have a GaN/Ga₂O₃ layer of about 30nm thick. However, EDS analyze of this layer has shown this layer has a Ga to Pt ratio

of 1:1, which indicates that the film has been contaminated during the process of Pt deposition. (The Pt deposition is used to protect the surface from Ion beam damage during the FIB process).

Therefore We have concluded from characterization results of this GaN film that to improve the purity of our sample, we need to grow at a higher laser repetition rate. A higher laser rep rate increases flux of atomic nitrogen produced per second, which speed up the reaction of Ga atoms with nitrogen flux, preventing the compound from oxidation during the growth process.

Figure 7.6a shows XPS characterization at nitrogen 1s binding energy of the GaN film grown on gold substrate at a laser repetition rate of 20 Hz (limit), in comparison with XPS characterization of commercial GaN crystal on silicon wafer (Figure 7.6b). our GaN film and the commercial GaN crystal have a very similar nitrogen binding profile. The fitting has shown that there are three different nitrogen containing chemical bonds forming. The peak at 398.3 eV, which is at the same energy as nitrogen 1s binding energy in standard data base, is attributed to adsorbed nitrogen molecule on the sample surface. The other two peaks shifted to lower binding energy are due to chemical bond formation of atomic nitrogen with other elements. Compared to the GaN sample previously grown at 1 Hz, which only present a small shoulder at lower binding energy, we have seen significant improvement of over 30% in terms of nitride chemical bond formation.

Figure 7.7 shows XPS characterization at gallium 2p_{3/2} binding energy. Comparing our GaN film with a commercial GaN crystal, the peak at 1118.7eV is attributed to GaN/*Ga₂O₃* formation. The peak at 1116.6eV indicates that we still have 8.6% of elemental gallium present in the sample.

In order to be more quantitative about the sample oxidation, we also studied oxygen 1s binding energy. From the number of counts obtained, we can conclude that the oxygen content is definitely higher in our GaN film compared to that of the commercial GaN crystal. The peak at 532.7eV, which is atomic oxygen binding energy, could be attributed to adsorbed oxygen molecules on the surface. Since our sample is nanocrystalline, shown in Figure 7.5b, there is more surface area to adsorb oxygen molecules than the crystalline GaN wafers. The peak at 531.5eV in Figure 7.8a could be attributed to *Ga₂O₃* formation, which exists at the minimum in Figure 7.8b. However, XPS characterization only studies the elemental composition of the surface within 10nm of penetration depth. In order to study the bulk content, we also performed energy dispersive spectroscopy (EDS) characterization on the

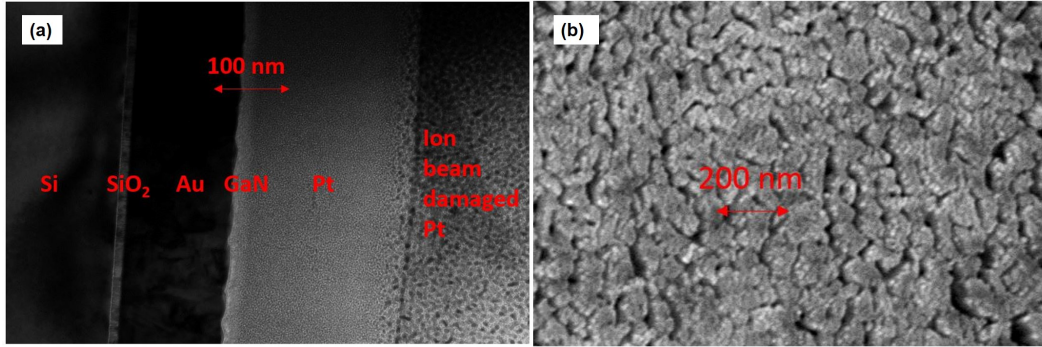


Figure 7.5: GaN film on gold substrate (a) Transmission electron micrograph of the film cross-section. (b) Scanning electron micrograph of the film.

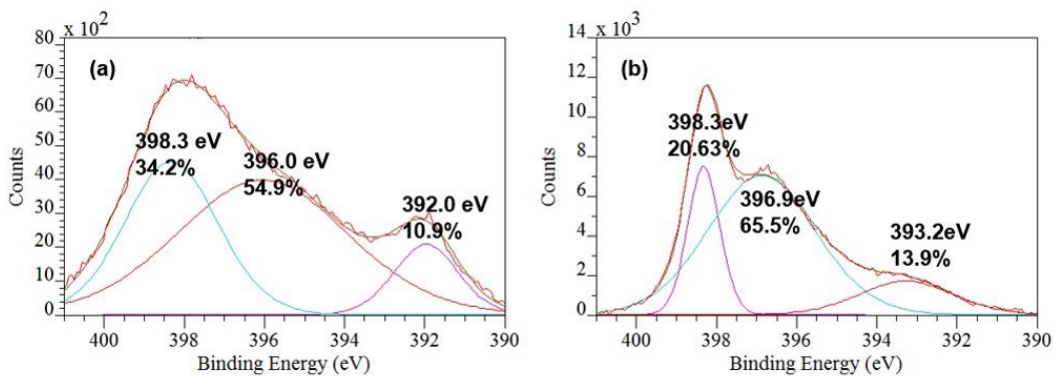


Figure 7.6: X-ray photoelectron spectroscopy of GaN film at nitrogen 1s of (a) GaN film grown on gold substrate. (b) Commercial GaN crystal on silicon wafer.

bulk of the sample. Table 7.2 shows comparison of the relative gallium, nitrogen and oxygen content in our GaN sample compared to commercial GaN wafer. Even though XPS characterization shows close chemical composition profile of our GaN sample and the commercial GaN wafer, EDS characterization indicates that our bulk content has much more oxygen than GaN crystal.

Atomic%	Gallium	Nitrogen	Oxygen
GaN sample	24.6	24.9	50.5
Commercial GaN wafer	30.4	61.8	7.8

Table 7.2: Energy dispersive X-ray spectroscopy.

It further indicates that our bulk content is closer to the surface composition of crystal GaN. The similarity could be attributed to higher than ideal growth chamber pressure. Air leaking through the cold stage has created a chemical reaction con-

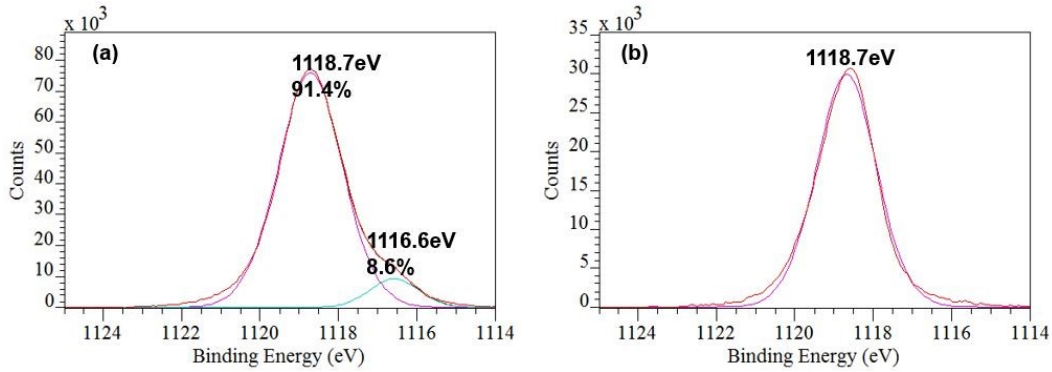


Figure 7.7: X-ray photoelectron spectroscopy of GaN film at gallium 2p_{3/2} of (a) GaN film grown on gold substrate. (b) Commercial GaN crystal on silicon wafer.

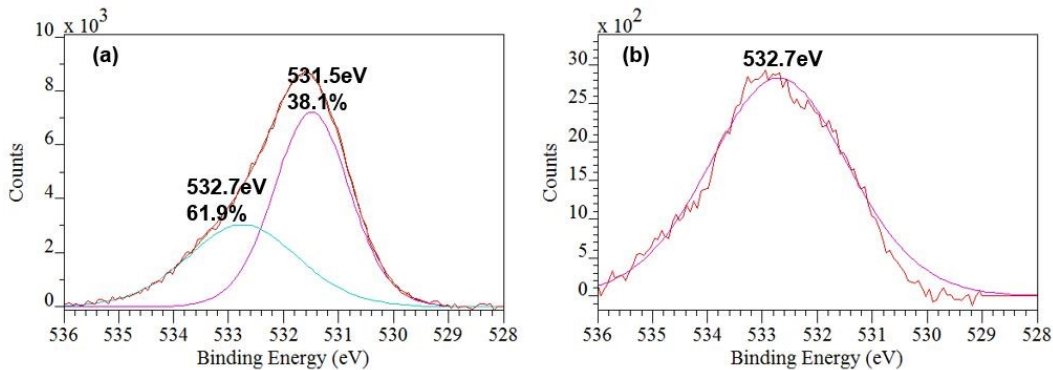


Figure 7.8: X-ray photoelectron spectroscopy of GaN film at oxygen 1s of (a) GaN film grown on gold substrate. (b) Commercial GaN crystal on silicon wafer.

dition close to what the surface of GaN crystal has encountered through exposure to air. Moving forward, our goal is to achieve a growth chamber pressure close to ideal. Therefore decrease the oxygen content in the bulk of our film. We would like to perform surface treatment on our growth substrate such as gold and sapphire, to better initiate GaN growth rather than Ga_2O_3 growth. We also would like to characterize our sample in the TEM without damaging the film content. In this case, growing a thicker film as well as depositing a nonreactive protection layer would help with the TEM sample preparation process.

7.8 Conclusions

In the past two decades, III-nitride semiconductors ($Al_xGa_yIn_{1-x-y}N$) have progressed from research curiosity to creating the materials foundation of visible wavelength optoelectronic and solid-state lighting technology. The 2014 physics Nobel prize was awarded to Isamu Akasaki, Hiroshi Amano, and Shuji Nakamura for de-

veloping GaN devices for blue LEDs. Our approach for III-nitride film growth has two key advantages: low growth temperature and selectivity of molecular species generated via resonant UV photo-activation of precursor dissociation pathways. These advantages improve film quality, growth rates, control of film content, and flexibility of growth substrates.

Works done in this chapter has demonstrated a robust method of generating low temperature nitrogen source via resonant photo-dissociation. Base on this method, we have performed preliminary work to growth GaN at room temperature, which has showed hope for further improvement towards high quality GaN film in future.

BIBLIOGRAPHY

- [1] M. Z. Hasan and C. L. Kane. “Colloquium”. In: *Rev. Mod. Phys.* 82 (4 Nov. 2010), pp. 3045–3067. DOI: [10.1103/RevModPhys.82.3045](https://doi.org/10.1103/RevModPhys.82.3045). URL: <https://link.aps.org/doi/10.1103/RevModPhys.82.3045>.
- [2] Xiao-Liang Qi and Shou-Cheng Zhang. “Topological insulators and superconductors”. In: *Rev. Mod. Phys.* 83 (4 Oct. 2011), pp. 1057–1110. DOI: [10.1103/RevModPhys.83.1057](https://doi.org/10.1103/RevModPhys.83.1057). URL: <https://link.aps.org/doi/10.1103/RevModPhys.83.1057>.
- [3] F. D. M. Haldane and S. Raghu. “Possible Realization of Directional Optical Waveguides in Photonic Crystals with Broken Time-Reversal Symmetry”. In: *Phys. Rev. Lett.* 100 (1 Jan. 2008), p. 013904. DOI: [10.1103/PhysRevLett.100.013904](https://doi.org/10.1103/PhysRevLett.100.013904). URL: <https://link.aps.org/doi/10.1103/PhysRevLett.100.013904>.
- [4] S. Raghu and F. D. M. Haldane. “Analogues of quantum-Hall-effect edge states in photonic crystals”. In: *Physical Review A* 78.3 (2008), p. 033834. URL: <https://link.aps.org/doi/10.1103/PhysRevA.78.033834>.
- [5] Ling Lu, John D. Joannopoulos, and Marin Soljacic. “Topological photonics”. In: *Nat Photon* 8.11 (2014), pp. 821–829. ISSN: 1749-4885. DOI: [10.1038/nphoton.2014.248](https://doi.org/10.1038/nphoton.2014.248). URL: <http://dx.doi.org/10.1038/nphoton.2014.248>.
- [6] Zheng Wang et al. “Observation of unidirectional backscattering-immune topological electromagnetic states”. In: *Nature* 461.7265 (2009), pp. 772–775. ISSN: 0028-0836. DOI: http://www.nature.com/nature/journal/v461/n7265/supinfo/nature08293_S1.html. URL: <http://dx.doi.org/10.1038/nature08293>.
- [7] Zheng Wang et al. “Reflection-Free One-Way Edge Modes in a Gyromagnetic Photonic Crystal”. In: *Phys. Rev. Lett.* 100 (1 Jan. 2008), p. 013905. DOI: [10.1103/PhysRevLett.100.013905](https://doi.org/10.1103/PhysRevLett.100.013905). URL: <https://link.aps.org/doi/10.1103/PhysRevLett.100.013905>.
- [8] Mohammad Hafezi et al. “Robust optical delay lines with topological protection”. In: *Nat Phys* 7.11 (2011), pp. 907–912. ISSN: 1745-2473. DOI: <http://www.nature.com/nphys/journal/v7/n11/abs/nphys2063.html#supplementary-information>. URL: <http://dx.doi.org/10.1038/nphys2063>.
- [9] Hafezi M et al. “Imaging topological edge states in silicon photonics”. In: *Nat Photon* 7.12 (2013), pp. 1001–1005. ISSN: 1749-4885. DOI: [10.1038/nphoton.2013.274](https://doi.org/10.1038/nphoton.2013.274)<http://www.nature.com/nphoton/journal/v7/n12/abs/nphoton.2013.274.html#supplementary-information>. URL: <http://dx.doi.org/10.1038/nphoton.2013.274>.

- [10] Mikael C. Rechtsman et al. “Photonic Floquet topological insulators”. In: *Nature* 496.7444 (2013), pp. 196–200. ISSN: 0028-0836. DOI: [10.1038/nature12066](https://doi.org/10.1038/nature12066)<http://www.nature.com/nature/journal/v496/n7444/abs/nature12066.html#supplementary-information>. URL: <http://dx.doi.org/10.1038/nature12066>.
- [11] Ling Lu et al. “Weyl points and line nodes in gyroid photonic crystals”. In: *Nat Photon* 7.4 (2013), pp. 294–299. ISSN: 1749-4885. DOI: <http://www.nature.com/nphoton/journal/v7/n4/abs/nphoton.2013.42.html#supplementary-information>. URL: <http://dx.doi.org/10.1038/nphoton.2013.42>.
- [12] Long-Hua Wu and Xiao Hu. “Scheme for Achieving a Topological Photonic Crystal by Using Dielectric Material”. In: *Physical Review Letters* 114.22 (2015), p. 223901. URL: <https://link.aps.org/doi/10.1103/PhysRevLett.114.223901>.
- [13] S. Y. Lin et al. “A three-dimensional photonic crystal operating at infrared wavelengths”. In: *Nature* 394.6690 (1998), pp. 251–253. ISSN: 0028-0836. URL: <http://dx.doi.org/10.1038/28343>.
- [14] F. García-Santamaría et al. “A Germanium Inverse Woodpile Structure with a Large Photonic Band Gap”. In: *Advanced Materials* 19.12 (2007), pp. 1567–1570. ISSN: 1521-4095. DOI: [10.1002/adma.200602906](https://doi.org/10.1002/adma.200602906). URL: <http://dx.doi.org/10.1002/adma.200602906>.
- [15] Judith E. G. J. Wijnhoven and Willem L. Vos. “Preparation of Photonic Crystals Made of Air Spheres in Titania”. In: *Science* 281.5378 (1998), pp. 802–804. DOI: [10.1126/science.281.5378.802](https://doi.org/10.1126/science.281.5378.802). URL: <http://science.sciencemag.org/content/sci/281/5378/802.full.pdf>.
- [16] Yurii A. Vlasov et al. “On-chip natural assembly of silicon photonic bandgap crystals”. In: *Nature* 414.6861 (2001), pp. 289–293. ISSN: 0028-0836. URL: <http://dx.doi.org/10.1038/35104529>.
- [17] Susumu Noda et al. “Full Three-Dimensional Photonic Bandgap Crystals at Near-Infrared Wavelengths”. In: *Science* 289.5479 (2000), pp. 604–606. DOI: [10.1126/science.289.5479.604](https://doi.org/10.1126/science.289.5479.604). URL: <http://science.sciencemag.org/content/sci/289/5479/604.full.pdf>.
- [18] Alvaro Blanco et al. “Large-scale synthesis of a silicon photonic crystal with a complete three-dimensional bandgap near 1.5 micrometres”. In: *Nature* 405.6785 (2000), pp. 437–440. ISSN: 0028-0836. URL: <http://dx.doi.org/10.1038/35013024>.
- [19] Markus Deubel et al. “Direct laser writing of three-dimensional photonic-crystal templates for telecommunications”. In: *Nat Mater* 3.7 (2004), pp. 444–447. ISSN: 1476-1122. URL: <http://dx.doi.org/10.1038/nmat1155>.

- [20] J. G. Fleming et al. “All-metallic three-dimensional photonic crystals with a large infrared bandgap”. In: *Nature* 417.6884 (2002), pp. 52–55. ISSN: 0028-0836. URL: <http://dx.doi.org/10.1038/417052a>.
- [21] Ling Lu et al. “Experimental observation of Weyl points”. In: *Science* 349.6248 (2015), pp. 622–624. ISSN: 0036-8075. DOI: 10.1126/science.aaa9273. eprint: <http://science.sciencemag.org/content/349/6248/622.full.pdf>. URL: <http://science.sciencemag.org/content/349/6248/622>.
- [22] Minghao Qi et al. “A three-dimensional optical photonic crystal with designed point defects”. In: *Nature* 429.6991 (2004), pp. 538–542. ISSN: 0028-0836. DOI: http://www.nature.com/nature/journal/v429/n6991/supinfo/nature02575_S1.html. URL: <http://dx.doi.org/10.1038/nature02575>.
- [23] V. Ramanan et al. “Three dimensional silicon-air photonic crystals with controlled defects using interference lithography”. In: *Applied Physics Letters* 92.17 (2008), p. 173304. DOI: [doi:http://dx.doi.org/10.1063/1.2919523](http://dx.doi.org/10.1063/1.2919523). URL: <http://scitation.aip.org/content/aip/journal/apl/92/17/10.1063/1.2919523>.
- [24] Stephanie A. Rinne, Florencio Garcia-Santamaria, and Paul V. Braun. “Embedded cavities and waveguides in three-dimensional silicon photonic crystals”. In: *Nat Photon* 2.1 (2008), pp. 52–56. ISSN: 1749-4885. DOI: http://www.nature.com/nphoton/journal/v2/n1/supinfo/nphoton.2007.252_S1.html. URL: <http://dx.doi.org/10.1038/nphoton.2007.252>.
- [25] James A. Dolan et al. “Optical Properties of Gyroid Structured Materials: From Photonic Crystals to Metamaterials”. In: *Advanced Optical Materials* 3.1 (2015), pp. 12–32. ISSN: 2195-1071. DOI: 10.1002/adom.201400333. URL: <http://dx.doi.org/10.1002/adom.201400333>.
- [26] S. Prayakarao et al. “Gyroidal titanium nitride as nonmetallic metamaterial”. In: *Optical Materials Express* 5.6 (2015), pp. 1316–1322. DOI: 10.1364/OME.5.001316. URL: <http://www.osapublishing.org/ome/abstract.cfm?URI=ome-5-6-1316>.
- [27] Michael Thiel et al. “Three-Dimensional Bi-Chiral Photonic Crystals”. In: *Advanced Materials* 21.46 (2009), pp. 4680–4682. ISSN: 1521-4095. DOI: 10.1002/adma.200901601. URL: <http://dx.doi.org/10.1002/adma.200901601>.
- [28] Mark D. Turner et al. “Miniature chiral beamsplitter based on gyroid photonic crystals”. In: *Nat Photon* 7.10 (2013), pp. 801–805. ISSN: 1749-4885. DOI: 10.1038/nphoton.2013.233. URL: <http://www.nature.com/nphoton/journal/v7/n10/abs/nphoton.2013.233.html#supplementary-information>. URL: <http://dx.doi.org/10.1038/nphoton.2013.233>.

- [29] Silvia Vignolini et al. “A 3D Optical Metamaterial Made by Self-Assembly”. In: *Advanced Materials* 24.10 (2012), OP23–OP27. ISSN: 1521-4095. DOI: 10.1002/adma.201103610. URL: <http://dx.doi.org/10.1002/adma.201103610>.
- [30] Mark D. Turner, Gerd E. Schröder-Turk, and Min Gu. “Fabrication and characterization of three-dimensional biomimetic chiral composites”. In: *Optics Express* 19.10 (2011), pp. 10001–10008. DOI: 10.1364/OE.19.010001. URL: <http://www.opticsexpress.org/abstract.cfm?URI=oe-19-10-10001>.
- [31] Vinodkumar Saranathan et al. “Structure, function, and self-assembly of single network gyroid (I4132) photonic crystals in butterfly wing scales”. In: *Proceedings of the National Academy of Sciences* 107.26 (2010), pp. 11676–11681. DOI: 10.1073/pnas.0909616107. URL: <http://www.pnas.org/content/107/26/11676.abstract>.
- [32] V. Babin, P. Garstecki, and R. Hołyst. “Photonic properties of multicontinuous cubic phases”. In: *Physical Review B* 66.23 (2002), p. 235120. URL: <http://link.aps.org/doi/10.1103/PhysRevB.66.235120>.
- [33] Benjamin P. Cumming et al. “Adaptive optics enhanced direct laser writing of high refractive index gyroid photonic crystals in chalcogenide glass”. In: *Optics Express* 22.1 (2014), pp. 689–698. DOI: 10.1364/OE.22.000689. URL: <http://www.opticsexpress.org/abstract.cfm?URI=oe-22-1-689>.
- [34] G. M Gratson et al. “Direct-Write Assembly of Three-Dimensional Photonic Crystals: Conversion of Polymer Scaffolds to Silicon Hollow-Woodpile Structures”. In: *Advanced Materials* 18.4 (2006), pp. 461–465. ISSN: 1521-4095. DOI: 10.1002/adma.200501447. URL: <http://dx.doi.org/10.1002/adma.200501447>.
- [35] J. H Moon et al. “Triply Periodic Bicontinuous Structures as Templates for Photonic Crystals: A Pinch-off Problem”. In: *Advanced Materials* 19.11 (2007), pp. 1510–1514. ISSN: 1521-4095. DOI: 10.1002/adma.200700147. URL: <http://dx.doi.org/10.1002/adma.200700147>.
- [36] Tena Dubček et al. “Weyl Points in Three-Dimensional Optical Lattices: Synthetic Magnetic Monopoles in Momentum Space”. In: *Physical Review Letters* 114.22 (2015), p. 225301. URL: <https://link.aps.org/doi/10.1103/PhysRevLett.114.225301>.
- [37] Guillaume Weick et al. “Dirac-like Plasmons in Honeycomb Lattices of Metallic Nanoparticles”. In: *Phys. Rev. Lett.* 110 (10 Mar. 2013), p. 106801. DOI: 10.1103/PhysRevLett.110.106801. URL: <https://link.aps.org/doi/10.1103/PhysRevLett.110.106801>.

- [38] Dezhuan Han et al. “Dirac Spectra and Edge States in Honeycomb Plasmonic Lattices”. In: *Phys. Rev. Lett.* 102 (12 Mar. 2009), p. 123904. DOI: 10.1103/PhysRevLett.102.123904. URL: <https://link.aps.org/doi/10.1103/PhysRevLett.102.123904>.
- [39] Jennifer A. Dionne et al. “Are negative index materials achievable with surface plasmon waveguides? A case study of three plasmonic geometries”. In: *Opt. Express* 16.23 (Nov. 2008), pp. 19001–19017. DOI: 10.1364/OE.16.019001. URL: <http://www.opticsexpress.org/abstract.cfm?URI=oe-16-23-19001>.
- [40] Stefan A. Maier, Pieter G. Kik, and Harry A. Atwater. “Observation of coupled plasmon-polariton modes in Au nanoparticle chain waveguides of different lengths: Estimation of waveguide loss”. In: *Applied Physics Letters* 81.9 (2002), pp. 1714–1716. DOI: 10.1063/1.1503870. eprint: <http://dx.doi.org/10.1063/1.1503870>. URL: <http://dx.doi.org/10.1063/1.1503870>.
- [41] Arseniy I. Kuznetsov et al. “Optically resonant dielectric nanostructures”. In: *Science* 354.6314 (2016). DOI: 10.1126/science.aag2472.
- [42] Toon Coenen, Jorik van de Groep, and Albert Polman. “Resonant Modes of Single Silicon Nanocavities Excited by Electron Irradiation”. In: *ACS Nano* 7.2 (2013), pp. 1689–1698. ISSN: 1936-0851. DOI: 10.1021/nn3056862. URL: <http://dx.doi.org/10.1021/nn3056862>.
- [43] J. van de Groep and A. Polman. “Designing dielectric resonators on substrates: Combining magnetic and electric resonances”. In: *Optics Express* 21.22 (2013), pp. 26285–26302. DOI: 10.1364/OE.21.026285. URL: <http://www.opticsexpress.org/abstract.cfm?URI=oe-21-22-26285>.
- [44] Nikita A. Butakov and Jon A. Schuller. “Designing Multipolar Resonances in Dielectric Metamaterials”. In: *Scientific Reports* 6 (2016), p. 38487. DOI: 10.1038/srep38487. URL: <https://www.nature.com/articles/srep38487#supplementary-information>. URL: <http://dx.doi.org/10.1038/srep38487>.
- [45] Jorik van de Groep et al. “Direct imaging of hybridized eigenmodes in coupled silicon nanoparticles”. In: *Optica* 3.1 (2016), pp. 93–99. DOI: 10.1364/OPTICA.3.000093. URL: <http://www.osapublishing.org/optica/abstract.cfm?URI=optica-3-1-93>.
- [46] R. Sapienza et al. “Deep-subwavelength imaging of the modal dispersion of light”. In: *Nat Mater* 11.9 (2012), pp. 781–787. ISSN: 1476-1122. DOI: <http://www.nature.com/nmat/journal/v11/n9/abs/nmat3402.html#supplementary-information>. URL: <http://dx.doi.org/10.1038/nmat3402>.

- [47] Alexander B. Khanikaev et al. “Photonic topological insulators”. In: *Nat Mater* 12.3 (2013), pp. 233–239. ISSN: 1476-1122. DOI: <http://www.nature.com/nmat/journal/v12/n3/abs/nmat3520.html#supplementary-information>. URL: <http://dx.doi.org/10.1038/nmat3520>.
- [48] Tzuhsuan Ma et al. “Guiding Electromagnetic Waves around Sharp Corners: Topologically Protected Photonic Transport in Metawaveguides”. In: *Physical Review Letters* 114.12 (2015), p. 127401. URL: <https://link.aps.org/doi/10.1103/PhysRevLett.114.127401>.
- [49] Lutz Langguth et al. “Plasmonic Band Structure Controls Single-Molecule Fluorescence”. In: *ACS Nano* 7.10 (2013), pp. 8840–8848. ISSN: 1936-0851. DOI: 10.1021/nn4033008. URL: <http://dx.doi.org/10.1021/nn4033008>.
- [50] A. Femius Koenderink and Willem L. Vos. “Light Exiting from Real Photonic Band Gap Crystals is Diffuse and Strongly Directional”. In: *Physical Review Letters* 91.21 (2003), p. 213902. URL: <https://link.aps.org/doi/10.1103/PhysRevLett.91.213902>.
- [51] L. Langguth et al. “Plasmonic phase-gradient metasurface for spontaneous emission control”. In: *Physical Review B* 92.20 (2015), p. 205401. URL: <https://link.aps.org/doi/10.1103/PhysRevB.92.205401>.
- [52] Per Lunnemann and A. Femius Koenderink. “Dispersion of guided modes in two-dimensional split ring lattices”. In: *Physical Review B* 90.24 (2014), p. 245416. URL: <https://link.aps.org/doi/10.1103/PhysRevB.90.245416>.
- [53] A. Hinke Schokker and A. Femius Koenderink. “Lasing at the band edges of plasmonic lattices”. In: *Physical Review B* 90.15 (2014), p. 155452. URL: <https://link.aps.org/doi/10.1103/PhysRevB.90.155452>.
- [54] Abbas Mohtashami, Clara I. Osorio, and A. Femius Koenderink. “Angle-Resolved Polarimetry of Antenna-Mediated Fluorescence”. In: *Physical Review Applied* 4.5 (2015), p. 054014. URL: <https://link.aps.org/doi/10.1103/PhysRevApplied.4.054014>.
- [55] Yen-Kuang Kuo et al. “Advantages of InGaN light-emitting diodes with GaN-InGaN-GaN barriers”. In: *Applied Physics Letters* 99.9 (2011), p. 91107. DOI: 10.1063/1.3633268. URL: <http://dx.doi.org/10.1063/1.3633268>.
- [56] Omkar Jani et al. “Design and characterization of GaN/InGaN solar cells”. In: *Applied Physics Letters* 91.13 (2007), p. 132117. DOI: 10.1063/1.2793180. URL: <http://dx.doi.org/10.1063/1.2793180>.
- [57] S Strite and H Morkoc. “GaN, AlN, and InN: A review”. In: *Journal of Vacuum Science & Technology B: Microelectronics and Nanometer Structures Processing, Measurement, and Phenomena* 10.4 (1992), pp. 1237–1266. DOI: 10.1116/1.585897. URL: <http://avs.scitation.org/doi/abs/10.1116/1.585897>.

- [58] Takayuki Miyazaki et al. “Properties of GaN films deposited on Si(111) by radio-frequency-magnetron sputtering”. In: *Journal of Applied Physics* 89.12 (2001), pp. 8316–8320. DOI: 10.1063/1.1368393. URL: <http://dx.doi.org/10.1063/1.1368393>.
- [59] F K Yam and Z Hassan. “InGaN: An overview of the growth kinetics, physical properties and emission mechanisms”. In: *Superlattices and Microstructures* 43.1 (2008), pp. 1–23. ISSN: 0749-6036. DOI: <http://dx.doi.org/10.1016/j.spmi.2007.05.001>. URL: <http://www.sciencedirect.com/science/article/pii/S0749603607001450>.
- [60] Mark A Hoffbauer et al. “In-rich InGaN thin films: Progress on growth, compositional uniformity, and doping for device applications”. In: *Journal of Vacuum Science & Technology B, Nanotechnology and Microelectronics: Materials, Processing, Measurement, and Phenomena* 31.3 (2013), p. 03C114. DOI: 10.1116/1.4794788. URL: <http://dx.doi.org/10.1116/1.4794788>.
- [61] Anika Kinkhabwala et al. “Large single-molecule fluorescence enhancements produced by a bowtie nanoantenna”. In: *Nat Photon* 3.11 (Nov. 2009), pp. 654–657. ISSN: 1749-4885. URL: <http://dx.doi.org/10.1038/nphoton.2009.187>http://www.nature.com/nphoton/journal/v3/n11/supinfo/nphoton.2009.187_S1.html.
- [62] Louis Brus. “Noble Metal Nanocrystals: Plasmon Electron Transfer Photochemistry and Single-Molecule Raman Spectroscopy”. In: *Accounts of Chemical Research* 41.12 (2008), pp. 1742–1749. DOI: 10.1021/ar800121r. URL: <http://dx.doi.org/10.1021/ar800121r>.
- [63] C J Chen and R M Osgood. “Direct Observation of the Local-Field-Enhanced Surface Photochemical Reactions”. In: *Physical Review Letters* 50.21 (May 1983), pp. 1705–1708. URL: <http://link.aps.org/doi/10.1103/PhysRevLett.50.1705>.
- [64] Robert T Kidd, David Lennon, and Stephen R Meech. “Surface plasmon enhanced substrate mediated photochemistry on roughened silver”. In: *The Journal of Chemical Physics* 113.18 (2000), pp. 8276–8282. DOI: 10.1063/1.1316106. URL: <http://dx.doi.org/10.1063/1.1316106>.
- [65] Suljo Linic, Phillip Christopher, and David B Ingram. “Plasmonic-metal nanostructures for efficient conversion of solar to chemical energy”. In: *Nat Mater* 10.12 (Dec. 2011), pp. 911–921. ISSN: 1476-1122. URL: <http://dx.doi.org/10.1038/nmat3151>.
- [66] Seth Michael Morton and Lasse Jensen. “A discrete interaction model/quantum mechanical method to describe the interaction of metal nanoparticles and molecular absorption”. In: *The Journal of Chemical Physics* 135.13 (2011), p. 134103. DOI: 10.1063/1.3643381. URL: <http://dx.doi.org/10.1063/1.3643381>.

- [67] Hideki Nabika et al. "Toward Plasmon-Induced Photoexcitation of Molecules". In: *The Journal of Physical Chemistry Letters* 1.16 (2010), pp. 2470–2487. DOI: 10.1021/jz100914r. URL: <http://dx.doi.org/10.1021/jz100914r>.
- [68] Abraham Nitzan and L E Brus. "Theoretical model for enhanced photochemistry on rough surfaces". In: *The Journal of Chemical Physics* 75.5 (1981), pp. 2205–2214. DOI: 10.1063/1.442333. URL: <http://dx.doi.org/10.1063/1.442333>.
- [69] Ragip A Pala et al. "A Nonvolatile Plasmonic Switch Employing Photochromic Molecules". In: *Nano Letters* 8.5 (2008), pp. 1506–1510. DOI: 10.1021/nl0808839. URL: <http://dx.doi.org/10.1021/nl0808839>.
- [70] Mathieu L Juan, Maurizio Righini, and Romain Quidant. "Plasmon nano-optical tweezers". In: *Nat Photon* 5.6 (June 2011), pp. 349–356. ISSN: 1749-4885. URL: <http://dx.doi.org/10.1038/nphoton.2011.56>.
- [71] Rizia Bardhan et al. "Theranostic Nanoshells: From Probe Design to Imaging and Treatment of Cancer". In: *Accounts of Chemical Research* 44.10 (2011), pp. 936–946. DOI: 10.1021/ar200023x. URL: <http://dx.doi.org/10.1021/ar200023x>.
- [72] Ghanshyam L Vaghjiani. "Ultraviolet absorption cross sections for N₂H₄ vapor between 191–291 nm and H(2S) quantum yield in 248 nm photodissociation at 296 K". In: *The Journal of Chemical Physics* 98.3 (1993), pp. 2123–2131. DOI: 10.1063/1.464190. URL: <http://dx.doi.org/10.1063/1.464190>.
- [73] Eric L Woodbridge, Michael N R Ashfold, and Stephen R Leone. "Photodissociation of ammonia at 193.3 nm: Rovibrational state distribution of the NH₂(A₂A₁) fragment". In: *The Journal of Chemical Physics* 94.6 (1991), pp. 4195–4204. DOI: 10.1063/1.460653. URL: <http://dx.doi.org/10.1063/1.460653>.
- [74] Wei-Guang Liu and William A Goddard. "First-Principles Study of the Role of Interconversion Between NO₂, N₂O₄, cis-ONO-NO₂, and trans-ONO-NO₂ in Chemical Processes". In: *Journal of the American Chemical Society* 134.31 (2012), pp. 12970–12978. DOI: 10.1021/ja300545e. URL: <http://dx.doi.org/10.1021/ja300545e>.
- [75] Yusuke Watanabe, Wataru Inami, and Yoshimasa Kawata. "Deep-ultraviolet light excites surface plasmon for the enhancement of photoelectron emission". In: *Journal of Applied Physics* 109.2 (2011), p. 23112. DOI: 10.1063/1.3537823. URL: <http://dx.doi.org/10.1063/1.3537823>.
- [76] Mark W Knight et al. "Aluminum Plasmonic Nanoantennas". In: *Nano Letters* 12.11 (2012), pp. 6000–6004. DOI: 10.1021/nl303517v. URL: <http://dx.doi.org/10.1021/nl303517v>.

- [77] Jinlian Hu et al. “Deep-Ultraviolet-Blue-Light Surface Plasmon Resonance of Al and Alcore/Al₂O₃shell in Spherical and Cylindrical Nanostructures”. In: *The Journal of Physical Chemistry C* 116.29 (2012), pp. 15584–15590. DOI: 10.1021/jp305844g. URL: <http://dx.doi.org/10.1021/jp305844g>.
- [78] M.A. Verschuuren. “Substrate Conformal Imprint Lithography for Nanophotonics”. PhD thesis. Utrecht University, 2010.

*Appendix A***CHAPTER 2 METHODS AND SUPPLEMENTARY INFORMATION****A.1 Full Wave Band Structure Simulation**

Simulations were performed using Lumerical FDTD Solutions v8.15.716. In simulations, bands are excited by randomly placing dipoles inside the simulation region that is defined by Bloch boundary conditions in x, y, and z directions. Randomly placed field monitors record electric and magnetic fields over time. Fourier transformation of the overall electric field versus time reveal spectrum of the bands. By tuning phase of the Bloch boundary conditions, we were able to calculate bands at wave vectors along all high symmetry directions in the Brillouin zone of a bcc lattice. Palik(25) n, k data for a-Si are used in the simulation (shown in Supporting Information, Figure 1S).

A.2 Sample Fabrication

Polymer gyroid structures were written in negative photoresist IP-Dip using the Photonic Professional GT system (Nanoscribe GmbH). The 40 nm thick aluminum oxide coatings on the polymer gyroids were conformally deposited via atomic layer deposition at 150 °C in a Cambridge Nanotech S200 ALD System with H_2O and trimethylaluminum (TMA) precursors. We used focused ion beam milling with the FEI Nova 200 Nanolab at 30 kV and 30 nA Ga beam condition to remove the crystal sides to facilitate polymer removal. We etched out the polymers with oxygen plasma using the March PX-500 plasma etcher, yielding a hollow inorganic aluminum oxide crystal. Then the structure is conformally coated and in-filled with 100 nm/150 nm of a-Si at 350 °C using static chemical vapor deposition, with refilled silane as the precursor at an average deposition speed of 10 nm/hour. Refractive index of both deposited a-Si and Al_2O_3 are measured and shown in Supporting Information, Figure 1S.

A.3 FTIR Characterization

The mid-infrared light is incident on the sample at incidence angles from 16° to 34° after being focused with a Cassegrain objective. The sample sits on an intrinsic double side-polished silicon substrate with the (001) crystal surface of the

gyroid structure in parallel with the substrate surface. Reflection and transmission spectra are collected from the same range of angles with two identical Cassegrain objectives on each side of the sample, respectively. Each incidence angle could excite a corresponding wave vector in a specific symmetry direction in the band structure. For three-dimensional crystal structures, the orientation of the crystal could determine projection of the band structure onto a specific symmetry plane.

A.4 Full Wave Simulation on deformed Crystals

Simulations were performed using Lumerical FDTD Solutions v8.15.716. To take into account the effects of polymer shrinkage during the structure developing process, we performed full wave simulation approximating the trapezoidal morphology shown in SEM images in Figures 2 and 4. The simulated structure is infinitely periodic in the x and y directions and has a finite length of three unit cells in the z direction, with the a-Si/ Al_2O_3 /a-Si material composition. The simulation region has periodic boundary condition in the x and y directions and perfectly matched layer (PML) absorbing boundary condition in the z direction. Plane wave source is incident on the structure in the (001) direction as indicated in Figure 3a. Frequency domain field monitors are placed above and below the structure to collect reflection and transmission spectra. We repeated the simulation for a series of unit cell sizes ranging from 4.2 to 4.7 μm with an increment of 0.1 μm . The arithmetic average of these six reflectance spectra, shown as the black dashed line in Figure 3c, is used to approximate the trapezoidal effect on the reflectance spectrum.

A.5 Optical constants of deposited materials

Psi (Ψ) and delta (Δ) data were measured using IR-VASE Mark II infrared variable angle spectroscopic ellipsometer, from a-Si/ Al_2O_3 films deposited on an intrinsic silicon substrate. Optical constants n and k were then obtained from psi (Ψ) and delta (Δ) using a three layer fitting model.

A.6 Fill fraction and discontinuity

Fill fractions are calculated in correspondence to $u(x,y,z)$ for a solid single gyroid structure. Our fabricated structure consists of a-Si (100nm) / Al_2O_3 (40nm) /a-Si (100nm) is a hollow single gyroid structure with fill fraction of 0.104. The a-Si (100nm) / Al_2O_3 (40nm) /a-Si (100nm) layers have $u(x,y,z)$ values of 1.1, 1.2, and 1.25 respectively. The inner hollow part corresponds to a connected air gyroid with $u(x,y,z)=1.35$, shown in Fig. S2b. For the hollow single gyroid consists of

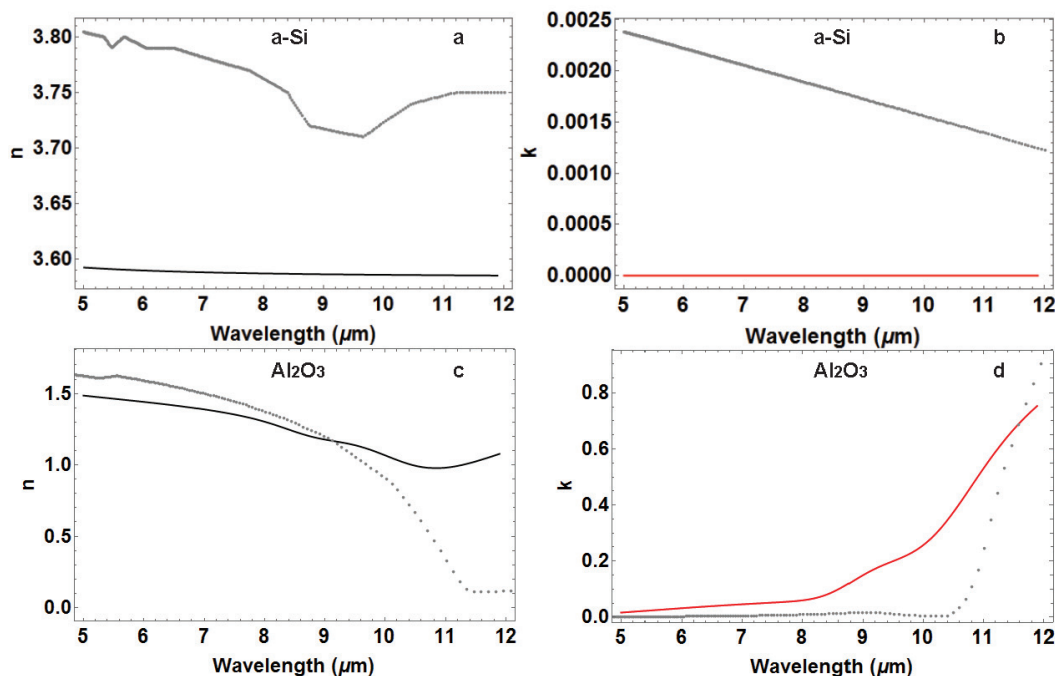


Figure A.1: Optical constants at Mid-infrared wavelength. (a) measured real part of refractive index of a-Si (black solid line) and Palik's real part of refractive index of a-Si (blue dotted line) (b) measured imaginary part of refractive index of a-Si (red solid line) Palik's imaginary part of refractive index of a-Si (blue dotted line) (c) measured real part of refractive index of Al_2O_3 (black solid line) and Palik's real part of refractive index of Al_2O_3 (blue dotted line) (d) measured imaginary part of refractive index of Al_2O_3 and Palik's real part of refractive index of (blue dotted line) Al_2O_3

$u(x,y,z)$	1.0	1.05	1.1	1.2	1.3	1.35	1.37	1.4	1.45
Fill fraction	0.155	0.141	0.127	0.077	0.060	0.023	0.021	0.018	0.004

Table A.1: $u(x,y,z)$ versus fill fraction for a solid single gyroid.

a-Si (150nm) / Al_2O_3 (40nm) / a-Si (150nm), the fill fraction is 0.12. The a-Si (150nm) / Al_2O_3 (40nm) / a-Si (150nm) layers have $u(x,y,z)$ values of 1.05, 1.2 and 1.25 respectively, and an inner air gyroid with $u(x,y,z)=1.37$. For $u(x,y,z)<1.41$, a solid gyroid structure is a connected network. The surface becomes disconnected at $u(x,y,z)=1.41$, as shown in Fig. S2b.

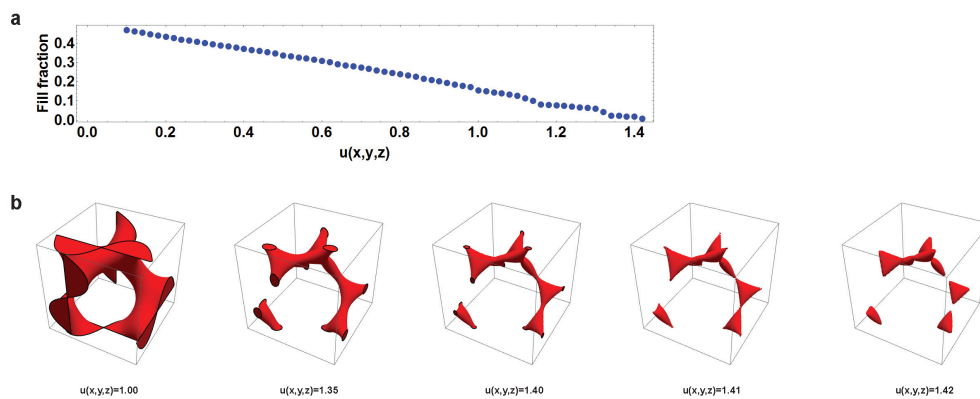


Figure A.2: Single gyroid with different $u(x,y,z)$. (a) $u(x,y,z)$ versus fill fraction for a solid single gyroid (b) single gyroid with $u(x,y,z)=1.00, 1.35, 1.40, 1.41,$ and 1.42 respectively